TEL AVIV UNIVERSITY
RAYMOND AND BEVERLY SACKLER
FACULTY OF EXACT SCIENCES
SCHOOL OF PHYSICS & ASTRONOMY

אוניברסיטת תל-אביב
הפקולטה למדעים מדוייקים
ע"ש ריימונד ובברלי סאקלר
בית הספר לפיסיקה ואסטרונומיה

Search for Physics beyond the Standard Model with the ATLAS detector and the development of radiation detectors

Dissertation submitted for the degree "Doctor of Philosophy"

By

Yiftah Silver

יפתח סילבר

Submitted to the senate of Tel Aviv University

May 26, 2014

Supervisor

Prof. Erez Etzion

This research was carried out under the supervision of professor Erez Etzion.

Abstract

We are investigating a radiation detector based on plasma display panel technology, the principal component of plasma television displays. This Plasma Panel Sensor (PPS) technology is a variant of micro-pattern gas radiation detectors. Based on the properties of existing plasma display panels, we expect eventually to be able to build a sealed array of plasma discharge gas cells to detect ionizing radiation with fast rise time of less than 10ns and high spatial resolution using a pixel pitch of less than 100 micrometer. In this thesis I shall describe our program of testing plasma display panels as detectors, including simulations, design and the first laboratory and beam studies that demonstrate the detection of cosmic ray muons, beta rays and medium energy protons.

The ATLAS detector is used to search for high-mass resonances, in particular heavy neutral gauge bosons (Z') and excited states of Kaluza-Klein γ/Z bosons decaying to an electron-positron pair or a muon-antimuon pair. Results are presented based on the analysis of pp collisions at a center-of-mass energy of 7 TeV and 8 TeV at the LHC. These results corresponds to an integrated luminosity of 4.9 (e^+e^-) / 5 ($\mu^+\mu^-$) fb^{-1} and 5.9 (e^+e^-) / 6 ($\mu^+\mu^-$) fb^{-1} collected by the ATLAS experiment in 2011 and 2012 respectively. In both the 2011 and 2012 analyses no deviation from the Standard Model (SM) were found. In the 2011 analysis the Kaluza-Klein γ/Z bosons were excluded at 95% confidence level (CL) for masses below 4.03 TeV in the electronic channel and below 4.71 TeV when the muon channel is included. A Z' with SM couplings is excluded at 95% CL for masses below 2.08 TeV in the electron channel and 2.22 TeV when the muon channel is included. In the 2012 analysis the exclusion of the Z' with SM coupling was extended, so that with 95% CL the model is excluded for masses below 2.39 TeV in the electron channel and 2.49 TeV when the muon channel is included. The results were also interpreted in a Grand Unification model based on the E_6 gauge group.

0.1 Preface

The work presented in this thesis is comprised of two separate parts. The first part of the thesis describes the development of Plasma Panel Sensor [1–4] (PPS) radiation detector. The second part of the thesis describes the search for Physics beyond the Standard Model with the ATLAS [5] detector at the LHC.

Detector R&D The development process of plasma panel radiation detector involved laboratory work, both in the Tel-Aviv University laboratory and in the University of Michigan laboratory (in which I worked for six month). I joined the PPS collaboration in its early days, as a consequence, I made contribution in every aspect of the development. The process began with the design and construction of the gas system. Through the design and manufacture of the very front end connectors and electronics. Simulation work, mainly for the electronic characteristics of the detector and also for the electric field. I also constructed the data acquisition system in the Tel Aviv Laboratory and wrote its analysis code.

In this thesis I shall present a compilation of selected simulations, measurements and experimental results which show the development and progress we have made in transforming a display panel into a working particle detector. The experimental results described here were measured in the laboratory as well as in two separate beam experiments (a proton beam and a muon beam).

Heavy neutral gauge boson search within the ATLAS experiment has been conducted. This part of the thesis includes the results from two analyses of pp collisions decaying into l^+l^- pairs at a center-of-mass energy of 7 TeV (collected during 2011) and 8 TeV (collected during 2012) at the Large Hadron Collider (LHC) at CERN. In this thesis I will focus on the analysis of the electron channel (which was under my responsibility) but for completeness I will present the results from the muon channel, as well as, the combined results (where applicable).

Kaluza-Klein γ/Z bosons model proposed in [6] assumes a single extra spatial dimension of size of order TeV^{-1}, compactified onto an S^1/Z_2 orbifold. It predicts Kaluza-Klein (KK) infinite tower of excitations of the gauge bosons, which can decay to dilepton final

states in the neutral case. Analysis that searches for the existence of the boson predicted by this model was performed on the data collected by the ATLAS experiment during 2011. As a perliminary step to the analysis I have implemented this model in a common simulation tool used in High Energy Physics (HEP), the PYTHIA8 event generator [7] and validated its results against the theoretical calculations [8].

A search for Z' signal was performed with both the data collected in 2011 and the data collected in 2012. While the analysis strategy is essentially the same for both, the increase of center-of-mass energy (from 7 TeV to 8 TeV), improvements to the electron reconstruction and identification and the slightly higher luminosity result with a broader range of exclusion for the Z' model in the 2012 analysis, in spite of the increase in pileup events. In addition to conducting the electron channel search, I was in charge for the production and validation of the Drell-Yan MC samples (the main background to this search), made the efficiency studies and the production and validation of the signal templates (MC).

0.2 Acknowledgments

Out of the many people who deserve my gratitude, there are few who stand out without whom this work could not be completed in the manner it did. First of all, I would like to thank my supervisor prof. Erez Etzion, who always kept his door open for questions and discussions, after which I always felt motivated and encouraged. The optimistic way and the deep insight on problems (not only in Physics) have taught me more than any textbook can, for which I will always be grateful.

Special thanks are also given to

- The Tel-Aviv University High Energy Physics group staff, prof. Halina Abramowicz, prof. Avner Soffer, prof. Gideon Alexander and Dr. Gideon Bella for being there to answer every question with the greatest patience possible. In particular, Dr. Yan Benhammou and Meny Ben-Moshe for always pushing my limits and extending my capabilities and most importantly for making the laboratory a second home.
- The University of Michigan Plasma Panel Sensor group leader Dr. Daniel S. Levin for teaching me so much, answering every question with patience and to great detail, and for making our stay in Ann Arbor both meaningful, educational and enjoyable. The entire PPS collaboration, Dr. Claudio Ferretti (UM), Dr. Peter Friedman (Integrated Sensors), Dr. Robert Varner (ORNL), Prof. J. Wehrley Chapman (UM), prof. Bing Zhou, Curtis Weaverdyck (UM) and Robert Ball (UM).
- The ATLAS Z'-analysis-team and especially the conveners of the 2011 analysis round, Dr. Simon Viel (TRIUMF), Dr. Sarah Heim (MSU), prof. Fabienne Ledroit (IN2P3), Dr. Wojciech T. Fedorko (MSU), Dr. Oliver Stelzer-Chilton (TRIUMF), Dr. Henri Bachacou (Saclay) and the conveners of the 2012 analysis round including also Dr. Rozmin Daya (Brandeis U). Special thanks are given to Dr. Noam Tal Hod from Tel Aviv University, who went through the stressful experimental work on the inclusion of the KK model along with me while concentrating on the $\mu^+\mu^-$ channel, without which the analysis could not have been made nor published eventually.
- The students with whom I shared an office in the past five years, for the fruitful discussions and the moral support. Especially, Dr. Noam Tal-Hod, Yonathan Munwes, Dr. Nir Guttman, Nimrod Taiblum, Avi Gershon, Adi Ashkenazi, Daphna Peimer, Rotem Gorodeisky and Itamar Levy.

- The management, the senior academic staff, the secretariat and staff of the School of Physics and Astronomy in Tel Aviv University, for all the professional and cheerful help over the nine happy years I have spent in the university.

Finally, my deepest gratitude is given to my entire family without whom I could not accomplish anything, especially my mother Yeudit, for being the role model that she is. I would also like to thank my wife's parents Tova and Zeev Lev-Ran for their endless support making our life much easier and happier. Most importantly, my wife Almog and my son Dory, you are the reason I wear my smile every morning when I wake up.

Contents

Part I

Detectors R&D

Chapter 1

Development of plasma panel radiation detectors

1.1 Plasma Panels Sensors introduction

We are investigating a new radiation detector technology based on plasma display panels used in plasma televisions and many other high power display devices. The design and production of Plasma Display Panels (PDPs) is supported by an extensive and experienced industrial base with four decades of development. The application of PDPs as particle detectors, which we are calling the Plasma Panel Sensor (PPS), is a novel variant of the micropattern radiation detector [2] [9] [3] [4], that can exploit this industrial and technology base. A PDP comprises millions of cells per square meter, each of which can initiate and sustain a plasma discharge on signal, much like a fluorescent tube.

The plasma created by the discharge emits UV photons that are translated into the visible light emitted from the PDP by a phosphor material covering the inside of each cell. The discharge dimensions are around 100 micrometers typically at pressures of 200 to 500 Torr, with an applied voltage between the electrodes of a few hundred volts. A PDP in the simplest matrix configuration consists of two glass plates with electrodes deposited on the surface. These are sealed with the electrodes aligned perpendicularly and facing each other. The gap separating the two plates is filled with a gas mixture of mostly Xe, Ar or Ne. When a voltage pulse is applied between two electrodes, a single pixel at the intersection of two perpendicular electrodes experiences a voltage above the breakdown voltage. This leads to formation of an avalanche discharge in the gas and to the formation of a weakly

ionized (only a small fraction of the atoms are ionized) plasma which emits visible and UV light [10].

We utilize the structure of a PDP, but reverse the order of processes. We arrange for ionization by radiation entering a PPS cell to cause a plasma discharge that is detected electrically. By controlling the gas, voltage and cell geometry, we intend to produce a particle detector with high spatial resolution and granularity, fast response and good timing resolution.

Our main motivation to explore the plasma display technology is to utilize the well established manufacturing processes of display panels to build scalable and cheap devices that are hermetically sealed , not requiring external gas systems.

We are currently exploring the behavior of slightly modified commercial monochromatic PDPs. These panels are designed to operate as display panels and are not optimized to detect ionizing radiation. Our main focus by studying the behavior of these panels under radiation, is to characterize the modifications needed in order to transform the display panels into effective detectors. The display panels we are testing vary from each other in the electrode material, pixel density and size, and separation of the electrodes (gas gap). We are able to fill the detectors to different gas pressures with different mixtures, either commercially sourced or produced in our gas mixing system.

All the tested panels are commercial display panels, operated with DC bias voltages. These panels are monochromatic, so there is no phosphor coating inside the panel cells. There is no dielectric barrier caging the pixels, these panels are simply a matrix of anodes and cathodes with few hundred micrometers gap filled with gas in between. These modified commercial PDPs produce signals when exposed to a radioactive source, a proton beam, a muon beam or cosmic rays. All the measurements described in this paper are made with two sets of display panels differing from each other in the geometrical dimensions. The specifications of the different panels are summarized in table 1.1.

An example of our test PDPs is shown in Fig. 1.1.

We are exploring the behavior of these PDPs under various kinds of radiation at two test benches, one at the University of Michigan, the other at the University of Tel-Aviv. Each test bench includes a gas mixing and delivery system, mechanical support, a triggering system and data acquisition systems.

Table 1.1: *Specifications of the panels used in our tests. The panel reference names are derived from our internal identification scheme and carries no global meaning. Packing fraction is calculated as the ratio between the active pixel area and the total area, electrode length includes only the electrode part inside the gas volume (without the electronic connection part)*

Name	VPA	VPi	MPi
High Voltage (HV) electrodes material	Ni	Ni	Ni
Read-Out (RO) electrodes material	Ni	SnO2	Ni
HV electrodes width	1.397 mm	1.397 mm	0.442 mm
RO electrodes width	1.27 mm	1.27 mm	0.714 mm
HV electrodes pitch	2.54 mm	2.54 mm	1.016 mm
RO electrodes pitch	2.54 mm	2.54 mm	1.016 mm
HV electrodes length	81.3 mm	81.3 mm	65 mm
RO electrodes length	325.4 mm	325.4 mm	131 mm
Active pixel area	1.502 mm^2	1.502 mm^2	0.224 mm^2
Packing fraction	23.5 %	23.5%	22%
Gas gap	0.483 mm	0.483 mm	0.294 mm
Glass thickness	2.23 mm	2.23 mm	2.23 mm

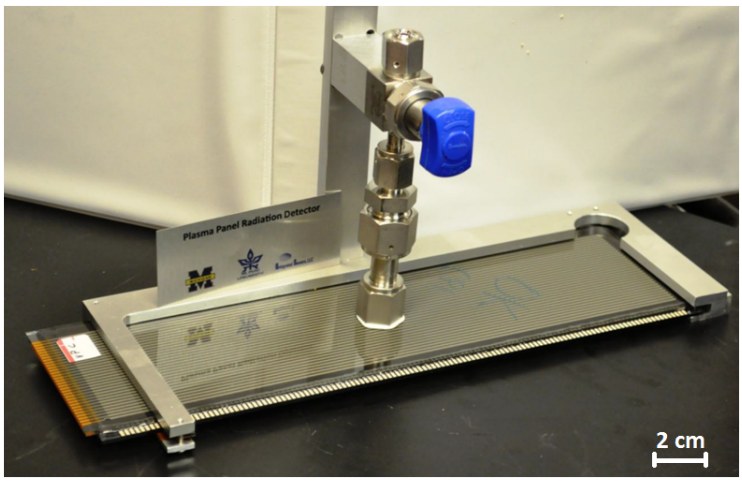

Figure 1.1: A picture of a commercial PDP in our test lab (VPA).

1.2 Motivation and operational principles

1.2.1 Gaseous detectors - what is known

Gaseous detectors rely and use the ionization effects of radiation upon gas filled sensors. Ionization can potentially occur in all gasses and in most condition, given a particle with

sufficient energy to ionize the gas atom or molecules. With the application of electric field the resulting electrons and ions will cause a measurable current flow (via the formation of an avalanche, a streamer or the complete "breakdown" of the gas). In the next few paragraphs we shall describe the relevant physical processes, the main procedures used today in modern gaseous detectors and the key considerations taken in the development of the PPS.

Relevant physical processes

When a particle traverse through the gas fill of a detector it ionizes the gas atom and molecules producing a trail of electron-ion pairs near the particle track. The number of ion pairs resulting in the primary ionization depend heavily both on the gas content and on the particle type and energy. Table 1.2 shows selected gasses properties related to the ionization by minimal ionizing particles. Aside the ionization process and parameters, several other physical processes determine the behavior of the gas and the detector operation.

Table 1.2: *Properties of noble and molecular gases at normal temperature and pressure (NTP: 20. C, one atm) [11]. EX, EI : first excitation, ionization energy; WI : average energy per ion pair; NP , NT : primary and total number of electron-ion pairs per cm, for unit charge minimum ionizing particles.*

Gas	Density	E_x	E_I	W_I	N_P	N_T
	mg cm^{-3}	eV	eV	eV	cm^{-1}	cm^{-1}
He	0.179	19.8	24.6	41.3	3.5	8
Ar	1.66	11.6	15.7	26	25	97
Xe	5.495	8.4	12.1	22	41	312
CO_2	1.84	7.0	13.8	34	35	100
CF_4	3.78	10.0	16.0	54	63	120

At low values of the electric field the ions and electrons will simply migrate or, drift at practically constant velocity (due to elastic collisions with the gas atom and molecules) to their respective collecting electrode. Ionization chambers rely on this process without any manipulations on the electrons and ions inside the gas volume of the detector. A very sophisticated amplification electronics is needed even when the number of primary ion pairs is relatively large. Provided a sufficiently high electric field, the electrons produced in the ionization process will start a gas multiplication process. Between collisions with the neutral gas atoms and molecules the electrons gain kinetic energy. The average kinetic

energy between collisions rise with the electric field. Above a threshold value for the electric field (usually in the order of 10^6 V/m) the kinetic energy of the electrons is larger than that needed in order to ionize a neutral atom or a molecules in the gas. Electrons liberated in this secondary ionization are too accelerated by the electric field, these electrons also collide with the gas atoms and molecules and in turn further ionize with each collision. The gas multiplication takes the form of a growing cascade, known as the Townsend avalanche. The incremental increase in electrons per unit length in the gas is governed by the Townsend equation (1.1), α is the first Townsend coefficient, it's value is zero for electric field (E) below the discussed critical value.

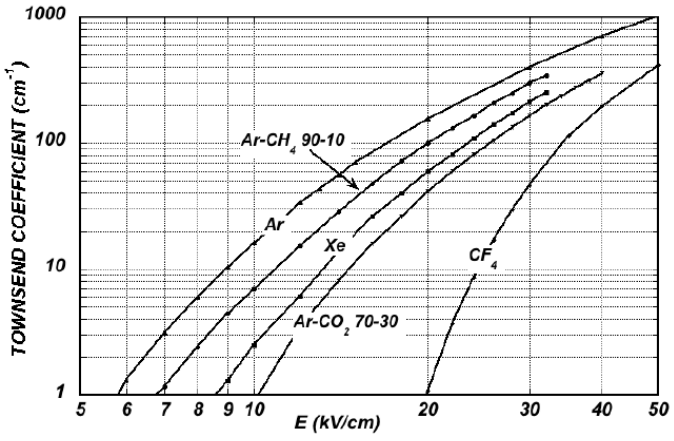

Figure 1.2: The first Townsend coefficient as a function of the electric field in several gasses at NTP [12]

$$\frac{dn}{n} = \alpha(E)dx \tag{1.1}$$

The total gain in electron number (A) after a distance x in the gas is therefor given by (1.2).

$$A(x) = \frac{n(x)}{n_0} = \exp \int_0^x \alpha(E)dx \tag{1.2}$$

Here n_0 represent the number of primary electrons at the starting position of the avalanche, and $n(x)$ are the number of electrons after a distance x in the avalanche. The total number of electrons collected on the electrode will then be (after total amplification A) An_0. In the avalanche many atoms are excited. When they return to their ground state UV photons are emitted. These UV photons create more electrons in the gas volume through photo electric effect with gas atoms or when they hit the metallic electrodes. The

second Townsend coefficient γ gives the probability for a photoelectron to be created by the UV photons, resulting with $An_0\gamma$ photoelectrons, which in turn get amplified to $A^2n_0\gamma$ etc. When taking UV photons into account, equation (1.3) shows the total number of electrons. Here A_γ denotes the total gas amplification including photons.

$$A_\gamma n_0 = n_0 A \sum_{i>0} (A\gamma)^i \xrightarrow[i\to\infty]{} \frac{n_0 A}{1 - A\gamma} \tag{1.3}$$

1.2.2 Gas properties

In addition to the processes described before a few other gas dependent processes determine the evolution of the avalanche. The processes described below are a direct result of the many collisions that occur in the gas. Under normal conditions and for most gasses the different species in the gas (neutral atoms and molecules, positive and negative ions and free electrons) are in constant thermal motion with typical mean free path of 10-1000 nm. All of these processes are highly dependent on the electrons and ions kinetic energy.

Charge transfer In the collisions, electrons will be transferred between neutral atoms and positive ions. As a result the specie with the lowest ionization energy will end as positive ions.

Electron attachment Some electro-negative gasses (e.g. Oxygen or CO_2) have high probability to form a negative ion after the attachment to a free electron in the gas. These negative ions behave practically like the positive ions produced in the ionization only with the opposite charge (thus traveling to the opposite electrode).

Recombination Collisions between a positive ion and a free electron can result in the capture of the electron and normalization of the space charge. alternatively, the collision can occur between a positive and negative ions in which transfer of the extra electron from the negative to the positive ion will neutralize both ions. In both cases, the charge represented by the original ion pair is lost and will not contribute to the signal.

In some cases, the second Townsend coefficient becomes significant and the creation of phtoelectrons result in uncontrolled gain in the gas. In order to control this behavior a quenching agent is added to the gas i.e. gas with polyatomic molecules that have many non-radiative vibrational and rotational states over a wide range of energy. The added

gas can easily absorb the UV photons. The molecules de-excite and release the absorbed energy into the gas through thermal collisions and dissociation.

Modes of operation

The modes of operation for gas filled detectors as a function of the applied voltage (electric field) are plotted in 1.3. At very low voltage the primary electron ion pairs simply recombine without any collected charge.

As the voltage is raised, recombination is suppressed, the electric field is not yet high enough to produce any multiplication. In this mode of ion saturation, all the electrons and ions produced in the primary ionization are collected, this is the operation mode for ionization chambers.

After further increasing the voltage, the first Townsend coefficient becomes non-zero and multiplication begins. Over some range of voltages the multiplication is linear with the applied voltage and the collected charge (and the size of the induced signal) is proportional to the number of primary ion pairs. This is the true proportional mode.

At a yet higher voltage value, some non linearities begin mostly due to the slow dissipation of the positive ions. The electrons in every avalanche are quickly collected in the detector electrode leaving behind a cloud of positive ions which alter and distort the electric field in it's vicinity. Since the multiplication factor depend on the value of the electric field, pulse sizes will still increase with the number of primary ion pairs but not linearly. this is the region of limited proportionality

With increasing value of the electric field the positive ion cloud becomes large enough so that the electric field near the cloud is sufficient to produce further multiplication. In addition, with increasing local electric field the second Townsend coefficient becomes non negligible and emitted photons will produce new ion electron pairs which in turn will start an avalanche. The process will self terminate when the electric field is reduced in the entire active volume of gas due to the positive ion charge. In this Geiger-Müller mode of operation, all proportionality is then lost and pulses will be of uniform amplitude.

Any further increase of the applied voltage will result in complete breakdown of the gas and constant discharge between the electrodes.

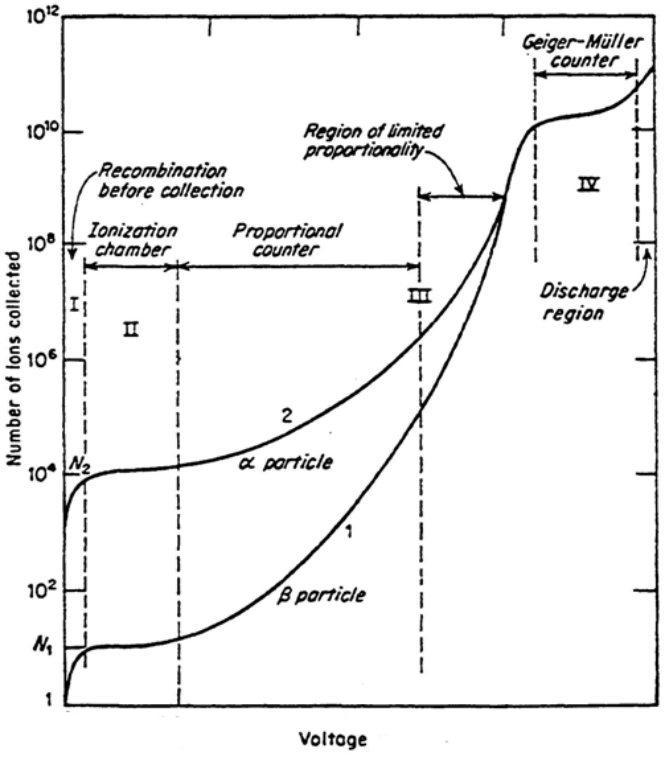

Figure 1.3: The different operational modes as a function of applied voltage in a typical gaseous detector

1.2.3 Signal formation and pulse shape

A simple model for one pixel in the PPS detector is that of a parallel plate capacitor filled with gas. The equivalent circuit model of this simple view is given in 1.4, where R_q is the quench resistor (typically 100 MΩ), C is the pixel total effective capacitance (which is measured to be 1-10pF) and R_t is the termination resistor on which the signal voltage is measured (usually 100 Ω). The effective capacitance is two orders of magnitude larger than the calculated capacitance for one pixel because all the pixels along the same electrode are not isolated. The voltage on the termination resistor V_{signal} is

$$V_{signal} = IR_t = \frac{dq}{dt}R_t \approx \frac{\Delta q}{\Delta t}R_t \tag{1.4}$$

We use equation 1.4 with typical values in order to make an order-of-magnitude assessment of the physical processes. The typical amplitude of the signal are tens of volts (it varies with the panel's dimensions) and it grows to this magnitude within $\gtrsim 1$ nsec.

$$100V \approx \frac{\Delta q}{1nsec} 100\Omega \tag{1.5}$$

Equation 1.5 gives us a gross lower bound estimate on the charge contributing to the discharge Δq which is $\approx 10^{10}$ electrons. This value is at least two orders of magnitude higher than the Raether limit [13,14]. Above this limit, space charge effects prevent further ionization within the avalanche. Then a positive streamer will be formed and will develop toward the cathode. When the streamer reaches the cathode a conductive plasma filament is conceived across the entire gas gap and a complete discharge occur. The development of the described positive streamer can be much faster than the time it takes the positive ions to propagate through the gas gap. Typical development time ranges between tens and hundreds of nsec and is very much gas, geometry and condition dependent.

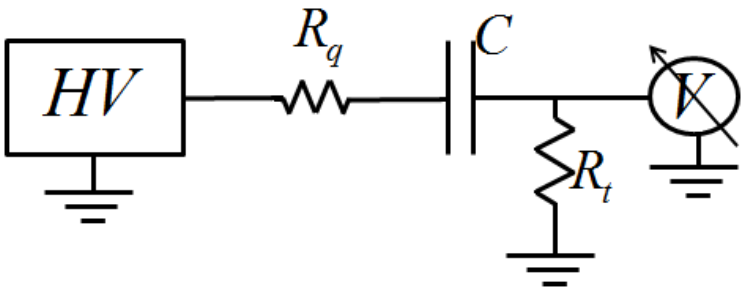

Figure 1.4: A schematic view of one pixel's signal extraction circuit

The evolution of the signal described by this, simplified capacitive discharge model, is only valid after the streamer has fully evolved into a conductive filament between the pixel electrodes. Currently, we do not have a complete description of the evolution time from avalanche to streamer which accurately predicts the gas dependent behavior. Regardless, the observed pulse characteristics are well described by the complete SPICE [15] model which simulates the single pixel embedded among neighboring pixels, connected via direct and stray capacitances and inductances.

Pixel dead time

During the discharge a conducting filament is created between the pixel's electrodes and electric current starts to flow between the electrodes. This current results in voltage dropping on the quench resistor, reducing the electric field between the pixel's electrodes. When the electric field is reduced the pixel cannot sustain the discharge and it is terminated and the gas neutralizes. The time it takes for the electric field to regain the sufficient strength (inside one pixel) to enable a new discharge depends solely on the RC constant, where R is the quench resistance and C is the effective pixel capacitance. For typical values of 100 MΩ

and 10 pF we get an RC time constant of 10^{-3} seconds which roughly translates into the pixel dead time as three times the RC time constant. Since the pixels are not separately quenched, the estimated dead time applies to the entire HV line and not to the individual pixels. The pixel dead time should be carefully chosen, by selecting an appropriate quench resistor. If the dead time is not sufficiently long, the positive ion cloud is not neutralized and the discharge can recur without an external trigger, giving rise to more than one pulse per incident particle. For dead time longer than necessary, the signal rate is saturated and the panel loses efficiency at high irradiation rates.

1.3 Simulations

1.3.1 Electronic properties - simulations

Because of the complexity of the PPS system that depends on energy loss, gas discharge and signal pickoff from sense lines, we have attempted to estimate the electronic properties of the panels using simulations, mostly COMSOL [16] for electric field simulation and SPICE [15] for electronic impulse response.

COMSOL

The electric field and potential as well as the electronic properties of the different components (e.g. capacitances and inductances of the pixels) were simulated with COMSOL. As an example, Fig. 1.5 shows that the electric field is confined to the pixel area with a very small fringe. This implies that the only active area in the panel is the area of the pixels as defined by the intersection of the electrodes.

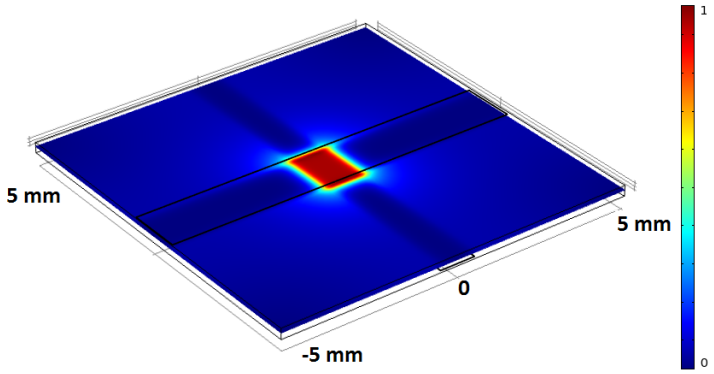

Figure 1.5: *COMSOL* simulation of the electric field strength (normalized to one) inside one pixel in the commercial PDP.

The size of signals induced in one pixel is directly related to the effective capacitance of that pixel. The calculation of capacitance resulting only from the intersection of two orthogonal electrodes yields capacitance of $\approx 5 \cdot 10^{-14}$ F. Signal sizes induced in one pixel demand a much higher effective pixel capacitance. In order to find a better estimation of the effective capacitance we have performed several more simulations.

First, we calculated the capacitance of two orthogonal electrodes only the size of the pixel electrodes (i.e. 1.25 mm in width and 0.45 mm apart). Then we simultaneously increased the length of both electrodes, keeping the pixel at the intersection of the electrodes

in the center of both electrodes. Figure 1.6 shows the calculated capacitance for one pixel for different electrode lengths. With this simulation we find an asymptotic value of 0.12 pF for two orthogonal electrodes in the specified geometry.

Second, we simulated a full array of 31×31 electrodes with a gap of 0.45 mm. The electrode in the center position on one side was set to 1 volt while the orthogonal center electrode was set as ground. The potential on all the other electrodes were allowed to float. Charge conservation was applied separately to each electrode so that the net charge of each electrode is zero, beside the HV and ground electrodes. The model did not include any dielectric material and as such can be regarded as a lower bound for the effective capacitance. The simulated effective capacitance result is 1.65 pF, comparable with the experimental results.

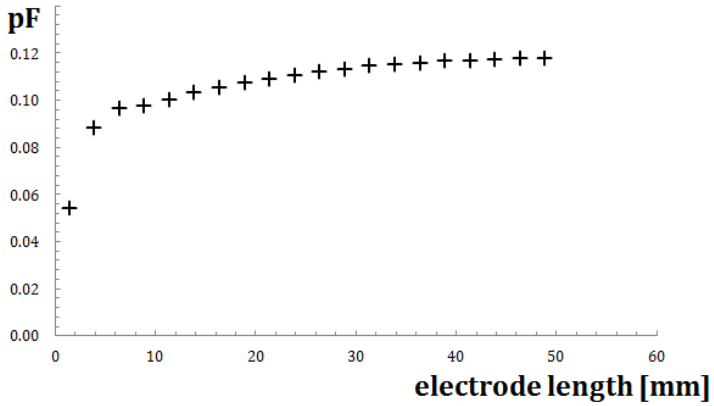

Figure 1.6: Capacitance of two orthogonal electrodes with vertical distance of 0.45 mm apart at varying length

The simulation of the entire array of electrodes allowed us to calculate the strength of the electric field in between the electrodes. Figure 1.7 shows the field strength resulting in between the electrodes along the HV electrode (set to 1 volt). We find that the electric field maximum strength is in the activated pixel's area, outside the pixel the field is sharply dropping to about third of it's value resulting with an inactive area, than for the adjacent pixels, the electric field regain about half it's original strength.

SPICE

We used the program SPICE to simulate the electrical characteristics of the signal induced in the panel electrodes during discharge. Fig. 1.8 shows the schematic of one cell in the panel. This circuit includes the capacitance of the cell, the self-inductance and resistivity

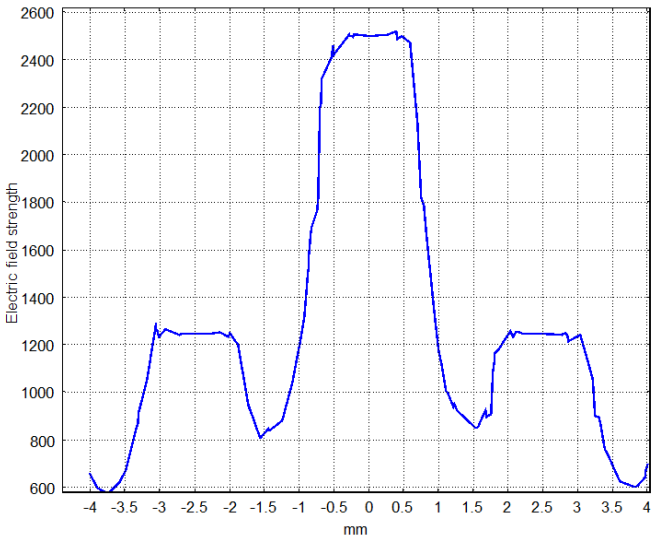

Figure 1.7: *COMSOL* simulation of the electric field strength (arbitrary scale) in between the electrodes along the HV electrode in the commercial PDP.

of the lines, and the nearest neighbor parasitic coupling capacitances. The parameters in the *SPICE* models were determined with our *COMSOL* electrostatic model. The full *SPICE* model connects all the neighboring cells to form a large array of pixels.

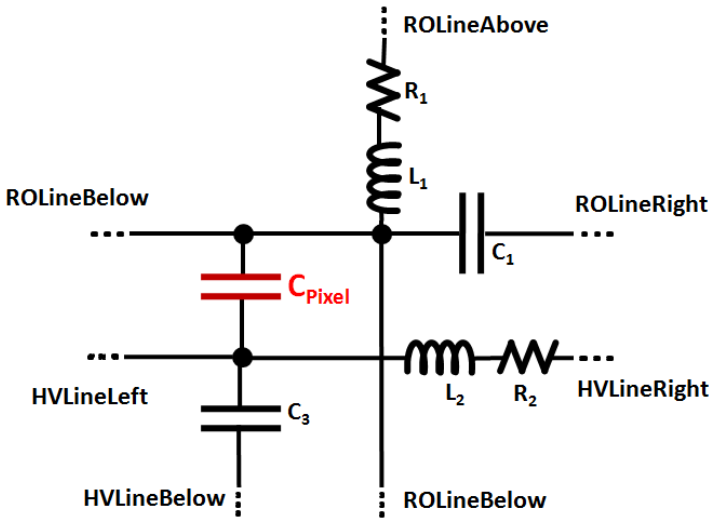

Figure 1.8: *SPICE* model of one cell in the commercial PDP, the parameters C, L and R are capacitances, inductances and resistances of a single cell coupled to it's neighbors. Dashed lines represent the cell's connections to other parts in the panel.

Fig. 1.9 shows the signal induced in an electrode by one pixel discharging and the signal induced in the neighboring electrodes. The induced signal results from the capacitive coupling between all the pixels in the panel and is not due to any discharge spreading.

Since the signal induced by the neighboring pixels is positive in comparison to the negative signal induced by the discharging cell, the determination of the location of the discharging pixel should be straight forward.

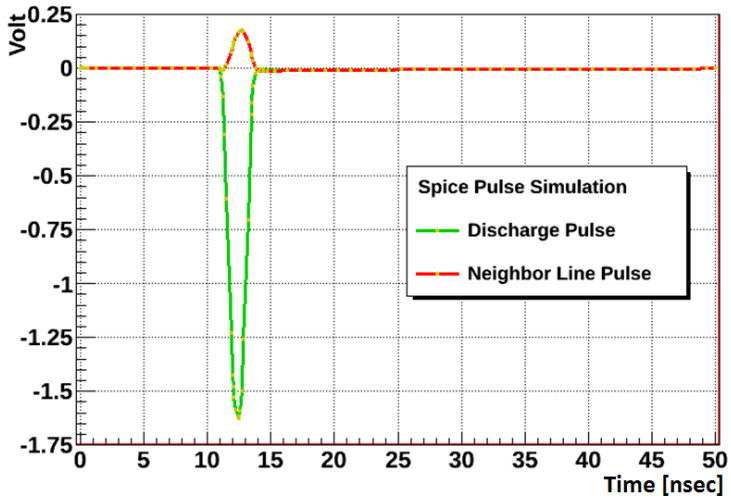

Figure 1.9: SPICE simulation results for the output pulse from a discharging cell and the signal induced in the neighboring electrodes.

1.3.2 Simulations of radiation energy loss and multiple scattering

We have used GEANT4 [17] simulations to evaluate the contribution to the position resolution by the scattering source emitted electrons. The incoming electrons are beta particles emitted out of the ^{106}Ru source and traveling through the 20 mm long air gap of the 1.25 mm wide graphite collimator and then through the 2.25 mm thick glass substrates of the PPS. The full simulation treats the effects of the source medium and window, as well as the finite size of the source material. The limited sample in Fig. 1.10 shows the effect of the air and glass energy loss and dispersion. Most of the scattering and absorption of betas occur in the PPS front glass substrate with very few betas exiting the back glass substrate.

The initial 1.25 mm collimated beam of beta particles has a scattering full width at half maximum of about 2.6 mm at the discharge gas volume, with long non-Gaussian tails, as shown in Fig. 1.11. In other words, the "collimated" beta beam inside the PPS illuminates approximately two adjacent sense electrodes on each side of the targeted electrode under the graphite slit.

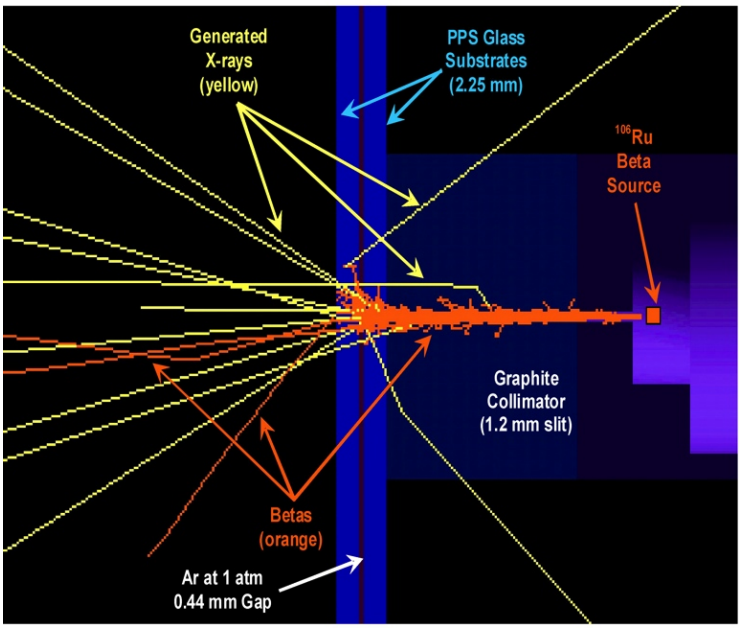

Figure 1.10: GEANT4 beta scattering simulation with ^{106}Ru source.

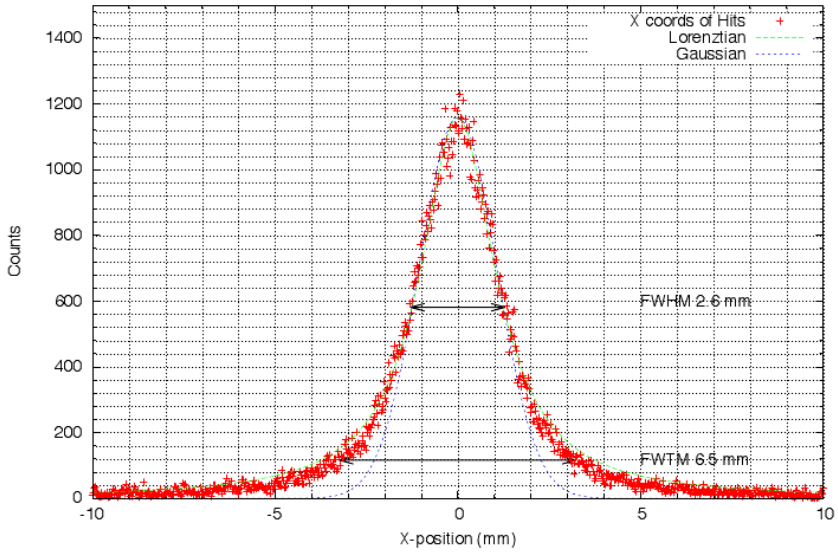

Figure 1.11: GEANT4 simulation showing the expected distribution of betas from the slit collimated ^{106}Ru source inside the PPS cell gas volume. The width of the distribution is comparable to the measured one.

1.4 Methodology and facilities

As mentioned, our collaborative effort includes two working laboratories, each of which operates a test bench for the detector prototypes. Each test bench has a dedicated Data Acquisition (DAQ) system, a triggering system, gas delivering system etc.

1.4.1 Radiation sources

In order to examine the panel's behavior we use a verity of radiation sources. In addition to the work done in our laboratories using radioactive sources and cosmic radiation, we also conducted experiments in other facilities i.e. muon beam at CERN and proton beam at an Ion Beam Applications (IBA) [18] cancer treatment facility [19]. We shall briefly present and discuss each of the used sources.

Radioactive sources

Measurements with radioactive sources presented in this paper were made with ^{90}Sr and ^{106}Ru β sources. Both laboratories uses similar sources with roughly the same activity and physical geometry. ^{90}Sr undergoes β^- decay with decay energy of 0.546 MeV distributed to an electron, an anti-neutrino, yielding ^{90}Y, which in turn undergoes β^- decay with half-life of 64 hours and decay energy of 2.28 MeV. Both ^{90}Sr and ^{90}Y are almost perfectly pure beta sources. The energy spectrum makes it highly unlikely for an electron emitted from this source to penetrate both a trigger detector and enter the panel active area, that requires it to penetrate the 3 mm glass layer. Electrons emitted from ^{106}Ru source have an energy spectrum reaching 3.54 MeV [20], which allows them to both trigger and induce discharges in the panel. In practice, such a small fraction of the spectrum is at this energy that it is practically impossible to activate a trigger detector and enter the active volume of the PPS. As a result, in all experiments performed with the radioactive sources, no external trigger used and we collect all the data from the panel with no real distinction to the origin of the signal.

Cosmic radiation

Muons are the most numerous charged particles at sea level [11](between the different kinds of cosmic radiation). Most muons are produced high in the atmosphere (typically 15 km) and lose about 2 GeV to ionization before reaching the ground. Their energy and angular distribution reflect a convolution of the production spectrum, energy loss in the atmosphere, and decay. As a good approximation the rate of cosmic muons at sea level is $I \propto 1$ cm^{-2}min^{-1} for horizontal detectors [11]. The overall angular distribution of muons at the ground is proportional to $\cos^2\theta$ (where θ is the angle from the vertical axis), which is characteristic of muons with $E_\mu \sim 3$ GeV. By measuring the effect of cosmic background

radiation i.e. cosmic muons on the PPS we can examine the panel's response to Minimally Ionizing Particles (MIP). With muons (both cosmic and from a beam) we can also use an external trigger for better discrimination and timing.

Proton beam

In order to determine if the PPS technology can detect protons in the low energy range (70-250 MeV) we used the cancer therapy proton beam in the Central DuPage Hospital (CDH) Proton Center, ProCure center located in suburban Chicago. This center uses an Iba cyclotron in order to accelerate protons to energies ranging from 70 to 250 MeV, then generates a controlled beam that is directed by magnetic fields through a nozzle to the targeted tumor.

The estimated beam current is about 1 nA with beam energy of 226.09 MeV, Gaussian distributed with 0.5 cm width, which corresponds to proton rate larger than 1 GHz on the entire spread of the beam (13.3 cm). The actual rate of protons from a 1 mm hole in the center of the beam was measured to be about 2 MHz.

Inside the patient room a computer controlled, robotic table with an XYZ translation system (six degrees of freedom) offering to change the table's position in all directions (with respect to the beam line) with a 0.1mm accuracy. Pictures of a patient room before and after the instrumentation of the PPS prototypes are shown in figures 1.12 and 1.13. In addition to the table movement a set of perpendicular lasers are being used in the room showing the position of the beam's center path (the crossing of the lasers).

Muon beam

The Super Proton Synchrotron (SPS) particle accelerator is located in CERN's north experimental area straddling the border of France and Switzerland near Geneva, Switzerland (see figure 1.14) . The test beam facilities uses SPS's 450 GeV proton beam and convert it (with a set of fixed targets and collimators) to electrons, hadrons or muons. The energy of the resulting particle beam ranges from 10 to 400 GeV, with a typical value of $10^3 - 10^4$ particles per spill, reaching a maximum intensity of 2×10^8 particles per spill. Spill structure ranges from 4.8 second spill every 14 seconds to 9.6 second spill every 48 seconds. We used H8 beam line populated with 180 GeV muons.

Figure 1.12: One of the patient rooms prior to the setup of the PPS test bench, on the right side of the picture the snout of the proton delivery system is visible and the robotic table is in the center

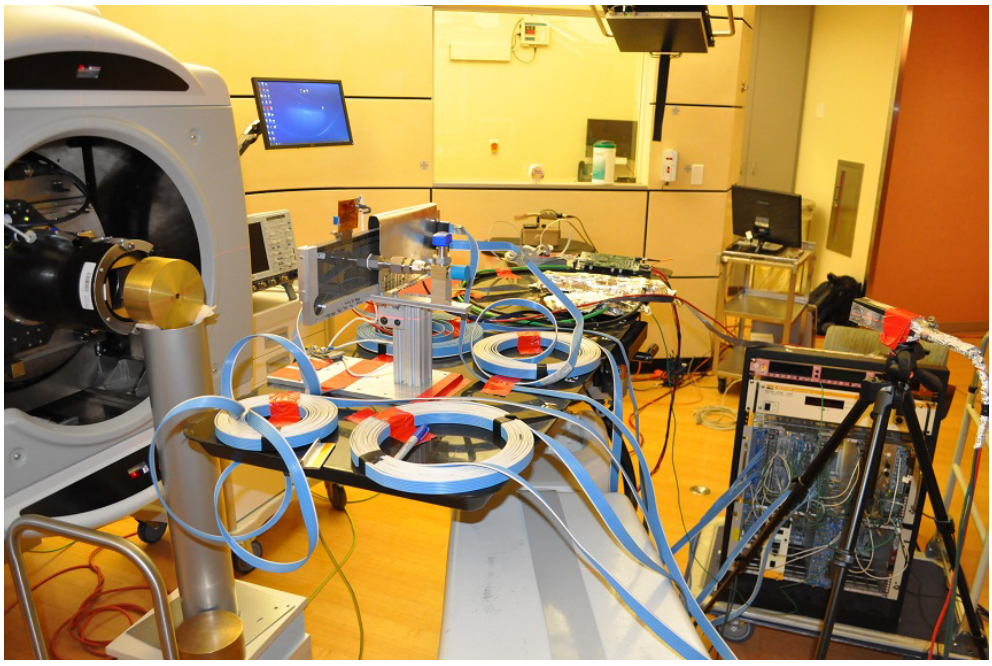

Figure 1.13: In the center, the PPS is mounted on the robotic table perpendicular to the beam line, in the left the beam is collimated with the round brass collimator (with 1cm circular hole), the blue cables are connecting the panel to the discriminators in the bottom right

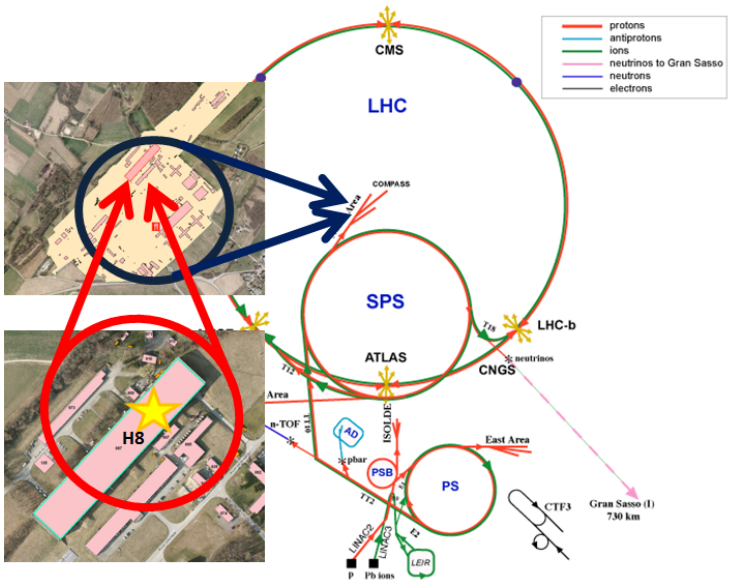

Figure 1.14: A scheme of CERN different accelerators and experiments (not to scale) and a picture of the test beam area at CERN north site.

Figure 1.15: Picture of the setup used in H8 muon test beam, visible in the picture are two scintillation pads and Photo Multiplier Tubes (PMTs) and the tested PPS prototype.

1.4.2 Signal extraction and acquisition

The prototypes described in this thesis were in fact display panels which we modified by adding a gas valve in order to change the gas content and pressure). The process of extracting the signal induced in the panel started with the assembly of Printed Circuit Board (PCB) connectors to be connected to the existing pads of the panels. Attenuation of the output signal is required, since the observed induced signal amplitude for some gases and applied voltages can reach few hundred volts.

Waveform digitizers - DRS4

In order to examine and measure the characteristics of the pulses induced in the panel, we used an oscilloscope. Since most oscilloscopes don't allow for an offline analysis of the data acquired, we used evaluation boards for the DRS4 chip [21]. The DRS4 chip, which has been designed at the Paul Scherrer Institute, Switzerland is a Switched Capacitor Array (SCA). Each evaluation board is basically equivalent to a four channel, 5 GSPS digital oscilloscopes operable on a personal computer. All the data acquired with the DRS4 are saved in binary or XML format directly on the computer. We have developed a set of dedicated computer programs in order to handle and analyze the collected data.

MiniDAQ - MicroDAQ

In order to instrument more readout lines and thus have a larger active area in the panel, a much more elaborate DAQ system was needed. We modified the ATLAS Monitored Drift Tubes (MDT) readout system MiniDAQ [22] (originally designed and built at the University of Michigan) to fit our needs. The MDT detectors are a part of the muon spectrometer in the ATLAS experiment in the LHC. As a second stage this modified DAQ system was further developed and minimized so transportation and setup are easily achieved. Data acquired with the MicroDAQ system allows for Time to Digital Converter (TDC) and Analog to Digital Converter (ADC) counts for every channel (without any real limitation on the number of channels).

Other DAQ used

As an intermediate step (between the scope's screen and MicroDAQ) we also used a variety of readout equipment. For counting experiments and various position scans, we used either

a NIM scalar [23] or a VME v560 16 channel scalar [24], for both a dedicated data analysis software was written. The signals induced in the panel were discriminated and then inserted into the counters. For analysis of the induced signals formation time and the crosstalk between channels we used a VME v1290 16 channel TDC [25]. Measurements with the TDC were carried out using the NIM signal from each channels after it was discriminated and not directly the signal itself.

Triggering

As previously discussed, it is not practical to trigger on electrons from ^{106}Ru and ^{90}Sr. So, for all the measurements using such sources all the attempts to use external trigger were futile, the rate of events was not significantly higher than that of the cosmic background. For all measurements using radioisotopes described in the next chapter, triggering of the DAQ was performed using the logical OR between all the readout channels in the following way: Each of the active channels in the panel were connected to a NIM discriminator where the exact discriminating threshold varied with gas content and pressure. The logic signal (NIM signal after discrimination) is then carried into a logic unit, the logical OR from all the signals is then used as the trigger. We used this technique of self triggering also in the proton beam measurements. This was due to technical difficulties in achieving good alignment between the proton beam, the panel's active area, and two layers of scintillation pads and Photo Multiplier Tubes (PMT). Were it was possible , we used external trigger composed of a set of small to medium (few cm^2) scintillation pads and a dedicated hodoscope which includes two, thin scintillation pads, this was designed especially for beta emission from a ^{90}Sr source but as was discussed, was not efficient for triggering the events induced by the radioisotopes.

1.5 Measurements and results

This section shows a compilation of results demonstrating the main features of the PPS prototype detector. More specifically:

- Response to radioactive sources.
- Signal characterization and the dependance on the applied voltage.
- The simultaneous response to two radioactive sources.
- Quench resistor dependance.
- Timing resolution measurements using cosmic ray muons and muon beam.
- Source position reconstruction and spatial resolution estimation using radioactive sources and proton beam.
- Discharge spreading and cross talk.
- Efficiency estimation.

As we continue to explore the parameter phase space for this technology, the list of measurements described in this section is not a full one. Nevertheless, it is enough to show the potential of this technology as particle detector.

1.5.1 Response to radioactive sources

The panel responds to the radiation emitted from ^{90}Sr and ^{106}Ru sources, with all of the tested gasses and in pressures ranging from as low as 200 Torr to slightly below room pressure. (The tested PDP's are designed to work in low vacuum and will break under positive pressure). Figure 1.16 shows a signal induced in the panel by ^{90}Sr on a panel filled with Xe at 600 Torr operated at 1120 volts.

1.5.2 Signal characterization

The signals from all the tested gasses are characterized by large amplitudes of several volts and fast rise times on the order of 1-3 ns. The large signals obviate (for the tested panels)

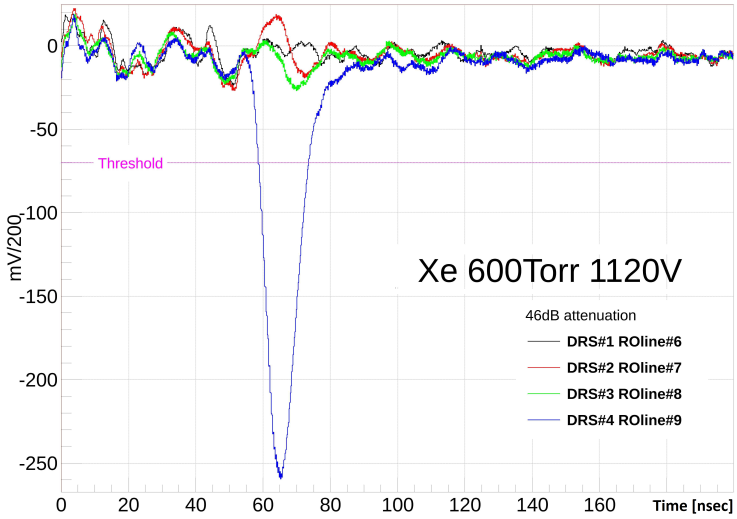

Figure 1.16: A representative signal induced in the panel (attenuated 200 times). Channel 4 (blue) shows the (negative) discharge pulse while the other channels (adjacent lines) show much smaller positive signals induced due to the capacitive coupling of the pixels in the panel.

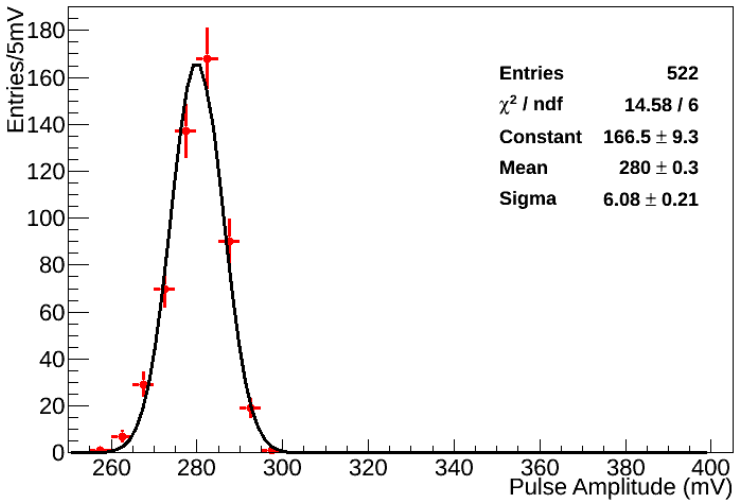

Figure 1.17: Distribution of the (attenuated) signal amplitudes for VPA (2.5 mm pitch) panel filled with 99%Ar 1%CO_2 operated at 860V. The Gaussian fit shows that the dispersion around the mean is only 2% of the most likely amplitudes.

amplification electronics, and sometimes necessitate attenuation. For each gas the shapes of the induced signals are uniform, as seen in one case from figure 1.17.

Two experiments were conducted to gauge the electrical modeling of the pixel used in the simulations. In the first, the dependence of the signal amplitude on the applied voltage was measured; this is expected to be linear from the schematic circuit in figure 1.4. The waveform for a single pixel pulse for a few runs at different HV was recorded. The

signal amplitude (as in Fig. 1.17) was then fitted with a Gaussian function. Figure 1.18 represents the mean of these fits dependence on the applied HV, confirming the expected linear relationship.

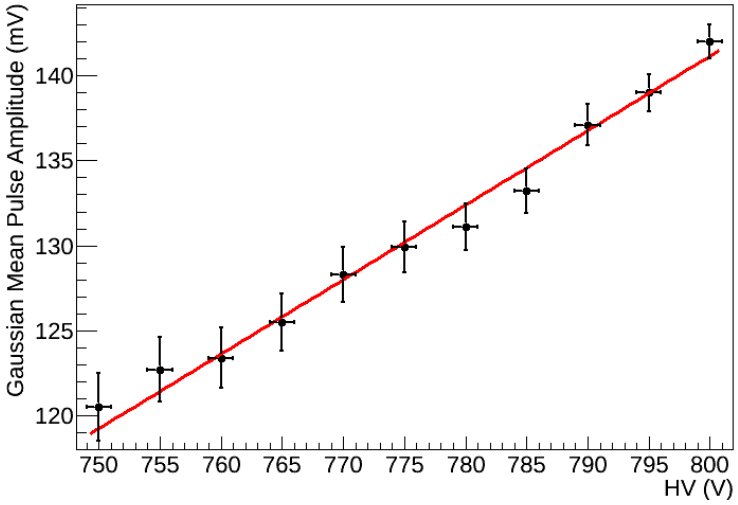

Figure 1.18: Gaussian mean of the (attenuated) signal amplitude vs HV, acquired with MP1 (1 mm pitch) panel filled with 90%Ar 10%CO_2. The fit to the data-points is shown only to show the linear relationship between pulse amplitude and HV.

In a second experiment the signal amplitude dependence on the number of readout lines connected is measured. This measurement is used to validate the SPICE simulation, which is limited to a 5×5 matrix around a central pixel. The exponential fit to the data in figure 1.19 shows that after five lines the amplitude of the signal reaches the asymptotic stable value. From this result we conclude that the matrix size of the SPICE electrical simulations is adequate to describe the effect of all pixels in these panels.

The modified commercial PDPs are fabricated with tolerances appropriate to their intended use as display units, not necessarily as stringent as required for detectors. It is therefore interesting to determine the *baseline* spatial response uniformity. Figure 1.20 shows the distribution of cosmic ray muon PPS hits per readout line (summed over the 30 HV lines instrumented). For this panel (with the indicated experimental gas and HV parameters) the difference between the average and a single channel is $\pm 20\%$.

Voltage scan

The response to radioactive source and background measurements were made repeatedly using different applied voltage. As a detector it is desired that the panel will respond to

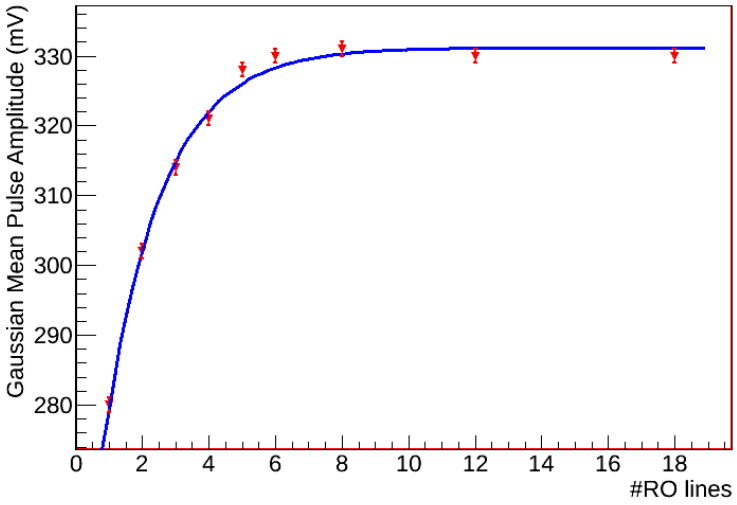

Figure 1.19: Gaussian mean of the signal amplitude vs. number of connected readout lines. VPA panel filled with 10% CF_4 in Ar at 600 Torr.

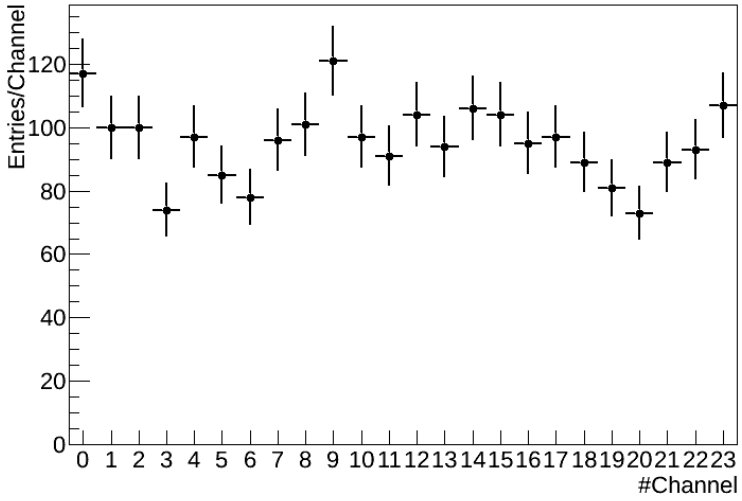

Figure 1.20: Hit map of cosmic rays acquired with VPA (2.55 mm pitch) panel filled with 1% CF_4 in Ar at 730 Torr and operated at 1040V.

the radioactive source (high rate of signal pulses) and minimal hit rate ($\mathcal{O}$(cosmic muon rate)) when no radioactive source is present. Figure 1.21 shows an example of a voltage scan taken with gas content of 1% CO_2 in Ar at 600 torr. For this measurement one HV quenched with one GΩ channel and four readout channels were instrumented. For every applied voltage two measurements were taken, one with the ^{106}Ru source placed above the panel's active area and the second measurement without the source.

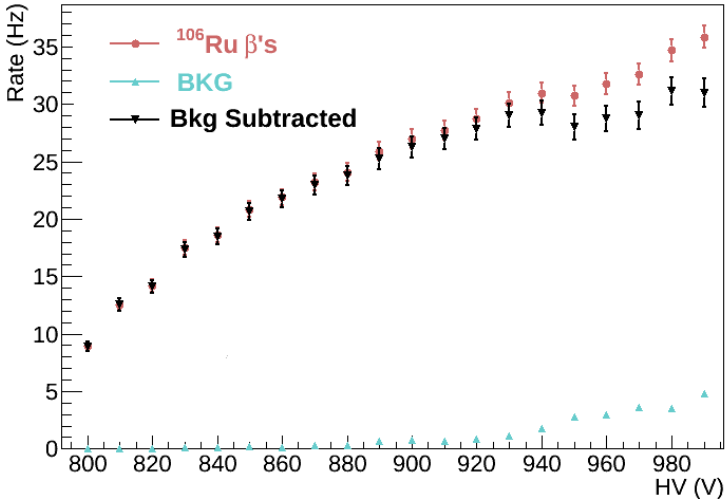

Figure 1.21: Panel response to ^{106}Ru source (red), background rate (green) and background subtracted response to the source (black) vs the applied voltage.

Response to two simultaneous β sources

It is expected (desired) that the different pixels will operate independently. This trait was measured with the use of two partially collimated β sources (^{106}Ru and ^{90}Sr) yielding approximately similar rates of betas entering the gas gap region. Four adjacent 32 cm long signal readout (RO) lines (i.e. sense row electrodes) were connected to discriminators whose outputs were ORed and then their combined signal rates were measured with a rate counter. HV was applied to two transverse column electrodes (i.e. cathodes) at varying distances from each other. The configuration is shown in figure 1.22, specifically, HV was applied always to one fixed line (#110) while the second line receiving high voltage was allowed to vary from #100 up to #110. The two sources were positioned, one below the panel and one above, over the active pixels as indicated by the two oval shaded regions in figure 1.22. The second source position was incremented from left to right across the panel starting from line #100. The rate was measured twice, first, the rate was measured with the different sources separately, than both sources were measured simultaneously. It is expected that the sum of the two separate measurements will be equal to the rate in the simultaneous measurement. A large quenching resistor was deliberately selected or this measurement in order to produce long cell recovery times close to the saturation value along the high voltage line. Figure 1.23 shows the results for this measurement. As expected the sum of the separate measurements rate equals the rate measured in the simultaneous measurement. As the HV lines get closer together (i.e radiation from the two sources start

to overlap) the active area starts to saturate. Due to this saturation the sum of the separate rates cease to be equal to the simultaneous rate.

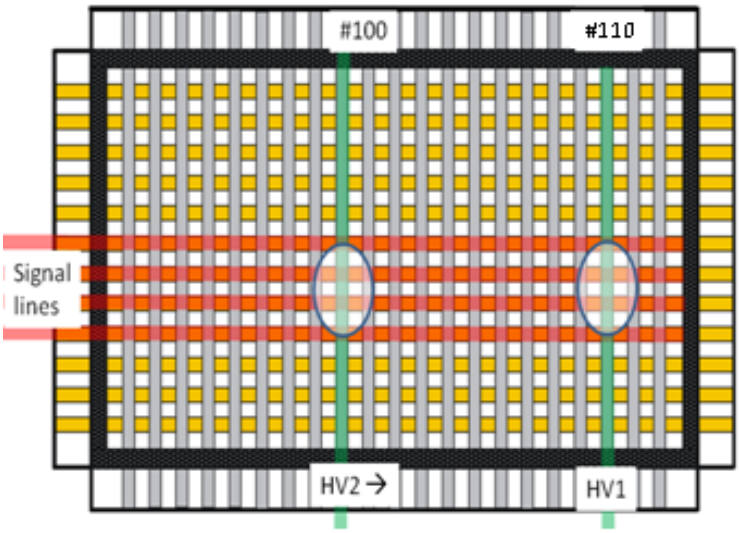

Figure 1.22: Configuration for double source test. Shaded regions show approximate location of radioactive beta sources. The line labeled HV2 is incremented from left to right towards HV1.

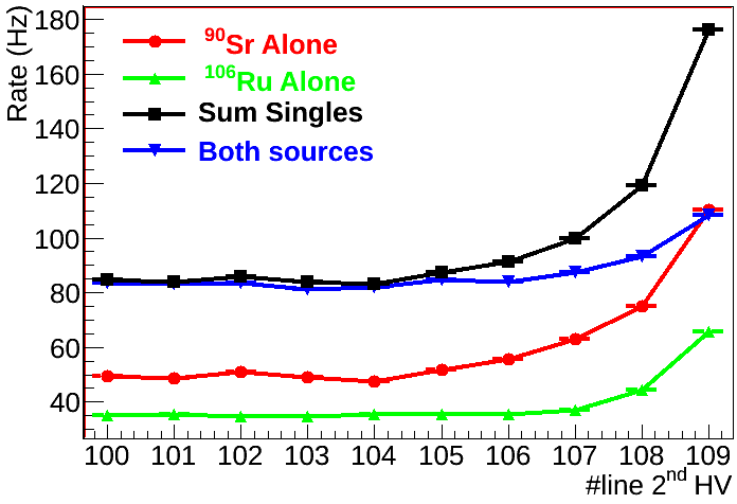

Figure 1.23: Simultaneous sources response measurement, red (green) are the rates measured with ^{90}Sr (^{106}Ru) source. Violet is the sum of the separate rates and blue is the rate measured with both sources simultaneously.

Quench resistor dependance

PPS characteristic response curve of dependence of the rate on the HV quench resistance can be made for a given panel and gas mixture. As shown in figure 1.24 the panel response

is the rate of hits detected and is plotted as a function of the reciprocal of the line quench resistor. In the presented result the panel was filled with 1% CO2 in Ar at 600 torr and was operated at 815 volt. The radioactive source is ^{106}Ru and the hits were collected on a single HV line, across four readout lines. The quench resistors covered the range from 10 to 600 MΩ. A pixel recovery time (i.e the minimal time between two consecutive pulses) is roughly three times the pixel's RC constant. The results of this experiment show that for resistance values below 20 MΩ the recovery time is not sufficient and after pulses (i.e spontaneous rejuvenation of the discharge) start to appear giving rise to false multiplication of signals. On the other hand, for resistance values above roughly 200 MΩ the pixel's RC constant is too high and the hit rate saturates (i.e measured rate is with accordance to the RC constant and much lower than the expected rate). We find that For resistance values between 20 to 200 MΩ we get a working plateau in which the measured hit rate does not depend on the resistor value.

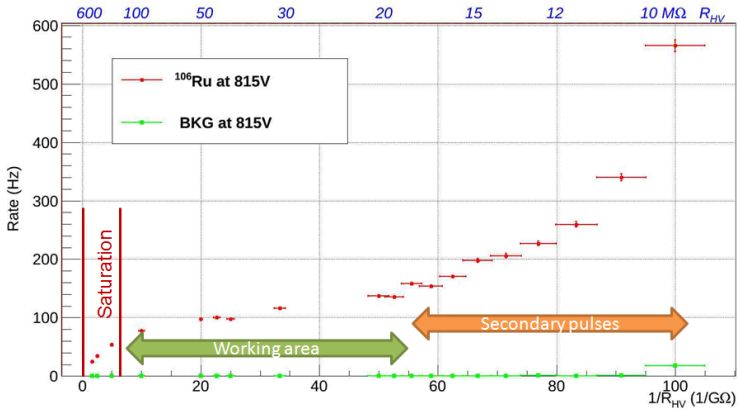

Figure 1.24: Signal induced by ^{106}Ru source (red) and background rate (green) dependance of the reciprocal of the line quenching resistor.

1.5.3 Timing resolution

In order to measure the time it takes the signal to form and the timing resolution of these panels, two methods are used. The first is with the use of cosmic (or beam) muons, in which we measure directly the time between the scintillator trigger and the signal induced in the panel. In the second we are measuring the time between the signal induced by radioactive source or cosmic radiation and the time a secondary pulse is induced in the panel by the means of discharge spreading. In the 2.5 mm pitch panels any discharge spreading was

estimated to occur in about twenty percent of the events and will be discussed in the next sections.

1.5.4 Cosmic ray muons detection

Cosmic ray muons allow us to test the panel response to minimally ionizing particles. Using the setup shown in figure 1.25 we are able to associate signals induced in the panel with cosmic muons.

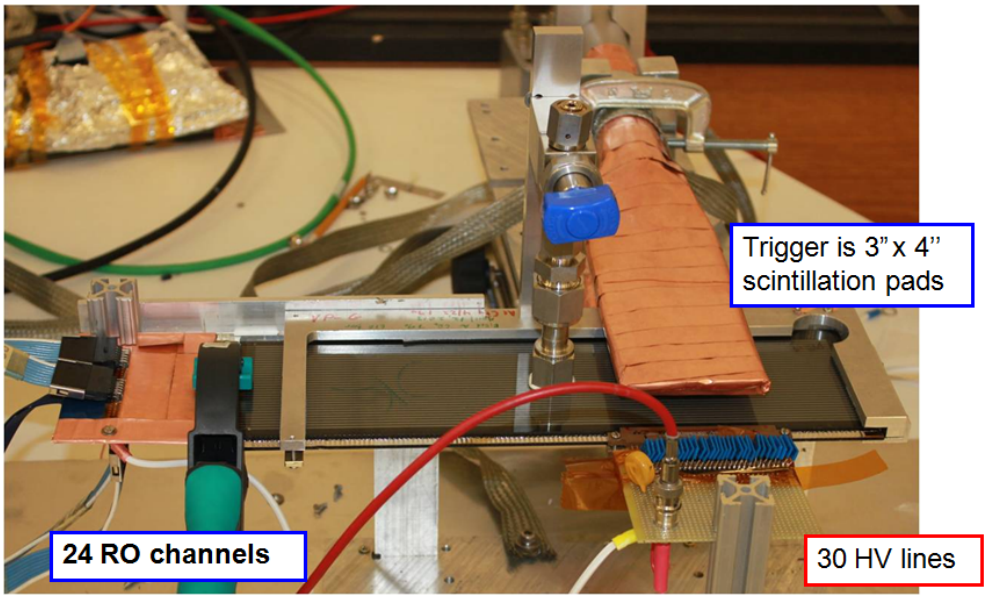

Figure 1.25: Picture of cosmic ray muon measurement setup, counting the number of signals induced in the panel which coincide with triggers from the scintillators (associated with cosmic ray muons).

We have also measured the elapsed time between the trigger (The time the muon passed through the panel in which arrival time = 0) and the time of the signal in the panel with various gas content.

Figure 1.26 shows a representative result of successful cosmic ray muons time distribution. We measured cosmic ray muons in various conditions (i.e different gas content and pressure as well as different applied HV). Two parameters from the muon arrival time distributions are of importance, the arrival time (i.e the actual time it takes for the discharge to form) and the width of the distribution (i.e the timing resolution of the detector).

Figures 1.27 and 1.28 show the mean and RMS of the muon arrival time distribution for various operating conditions. From these distributions we see that the timing resolution

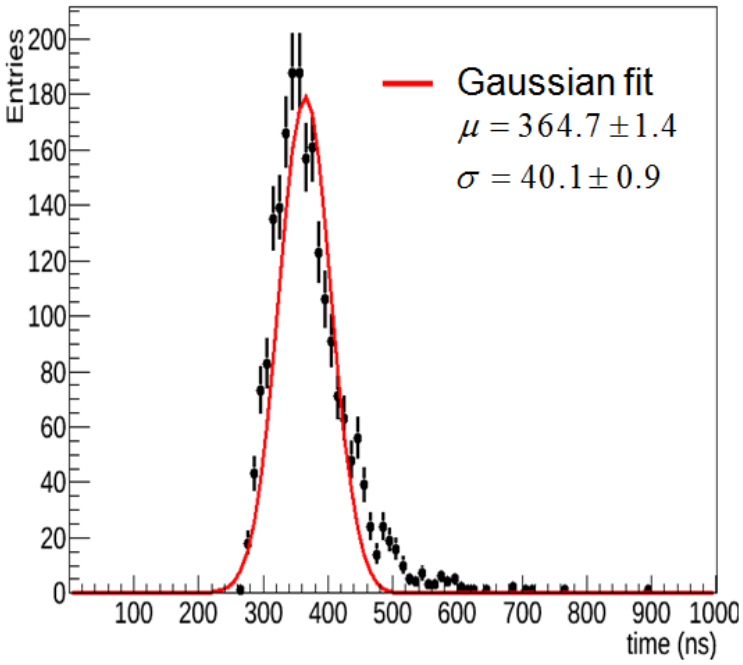

Figure 1.26: Cosmic ray muons arrival time distribution. Gas content: 1% CF4 in Ar at 730 torr and 1100 volts.

improves as the HV increases.

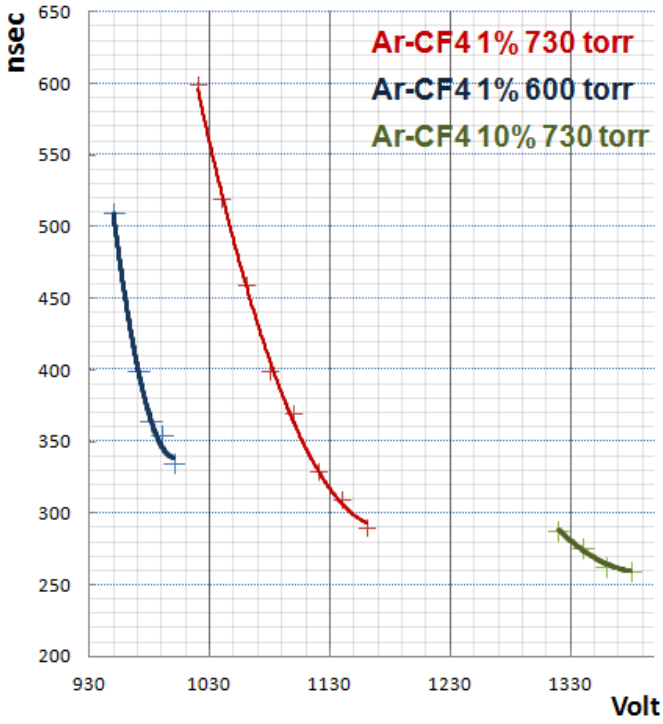

Figure 1.27: Compilation of muon mean arrival time for various gas conditions.

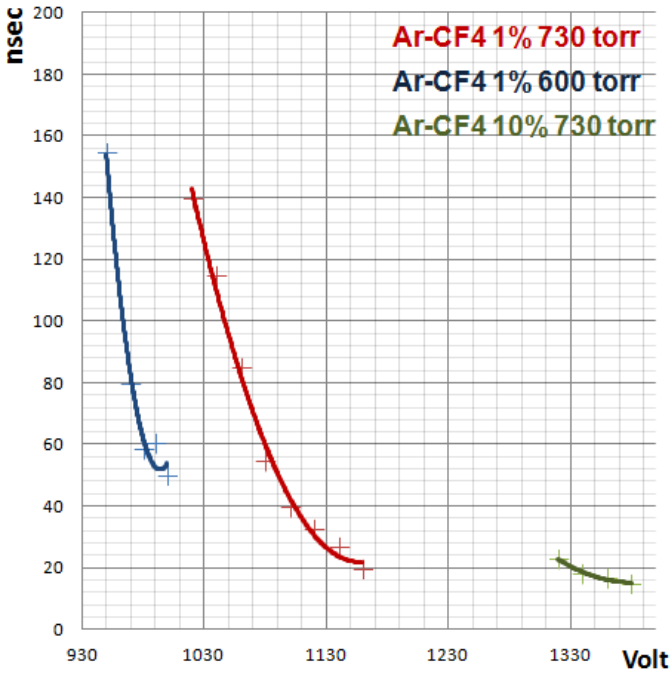

Figure 1.28: Compilation of muon RMS of the arrival time distributions for various gas conditions.

Muon beam

The setup used for the measurement of 180 GeV muons in CERN H8 test beam facility is sketched in figure 1.29. the panel was filled with 7% CO2 in Ar at 600 torr, the applied voltage is 1090 volt. Instrumented are 8 HV lines each quenched with 100 MΩ resistors, 16 readout channels each is attenuated by 40 dB (× 100) and discriminated. The trigger in use is the coincidence between two square scintillation pads 4 cm^2 each, placed close together and about 15 cm away from the panel active area (along the beam path). We have measured the time between the trigger and the signal induced in the panel. The arrival time distribution fitted with a double Gaussian function is shown in figure 1.30. From this distribution we see that for these conditions (gas content and applied voltage) the timing resolution is better than 10 nsec and with latency of about 40 nsec (from the parameters of the narrow Gaussian cited in the figure).

1.5.5 Position Scans

We performed a set of measurements in which we successfully reconstructed the relative position of a radiation source with respect to the plasma panel sensor. In these measure-

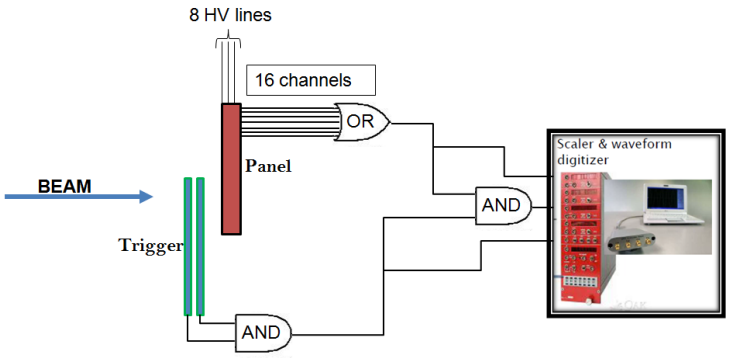

Figure 1.29: A scheme of the muon test beam measurement setup.

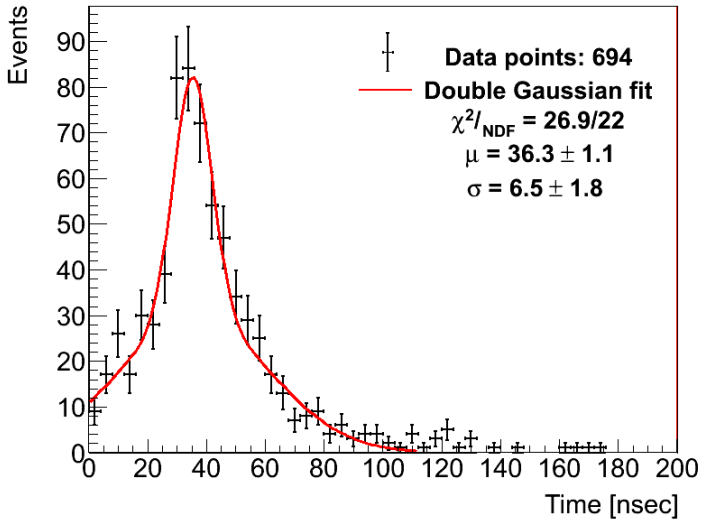

Figure 1.30: Arrival time distribution of 180 GeV muons with respect to scintillator trigger signal.

ments, a large working area ($\sim$ 20 read out lines) was instrumented. A collimated radiation source (betas or protons) was detected giving rise to a hit map distribution. Two different types of position scan measurements were conducted. The first type of measurement was held in our laboratories using a collimated radioactive source, typically ^{106}Ru, and the second was held at the IBA ProCure cancer treatment facility using a 226 MeV proton beam.

Radioactive sources

We designed a routine to automatically perform position scans of our detector. In this setup the collimated ^{106}Ru source (a graphite collimator with a 1.25 mm slit opening) was

mounted on a motorized robotic arm. The robotic arm is controlled by a Labview program enabling the movement of the source in both x and y directions with step sizes as small as 2.5 μm. At each step of the position scan, we acquire data for the same amount of time and signals from each channel are inserted (after discrimination) into a 20 channel scalar (see section 1.4.2).

Figure 1.31 is the result of a single step of a position scan. The position scan shown used the ^{106}Ru source and at each step data was acquired for 20 minutes. In general, for each complete scan, the hit map from each step is fit with a Breit-Wigner plus linear function to model the peak and long tails of the distribution. The position of the source, as seen by the detector, is then taken to be the mean of the aforementioned fit function. Figure 1.32 shows reconstructed source positions for a series of steps (100 μm step size) from a single position scan.

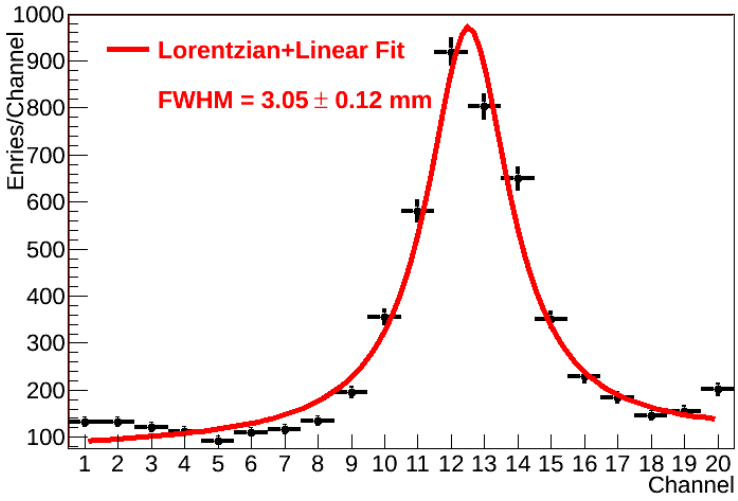

Figure 1.31: Representative hit map distribution induced in MP1 (1 mm pitch) panel by the collimated ^{106}Ru source.

Proton beam

VPA panel (table 1.1) was filled prior to the test with a gas mixture of 99% Ar and 1% CO_2 at a pressure of 600 Torr.

We have instrumented the panel with 24 read out lines (channels 1 to 24 which correspond to lines 4 to 27 on the panel). However, the electrodes on channels 18-24 were masked off and were not connected to the panel. The connector from the panel to the read-out electronics was instrumented with 100X attenuation circuit (for each channel). After

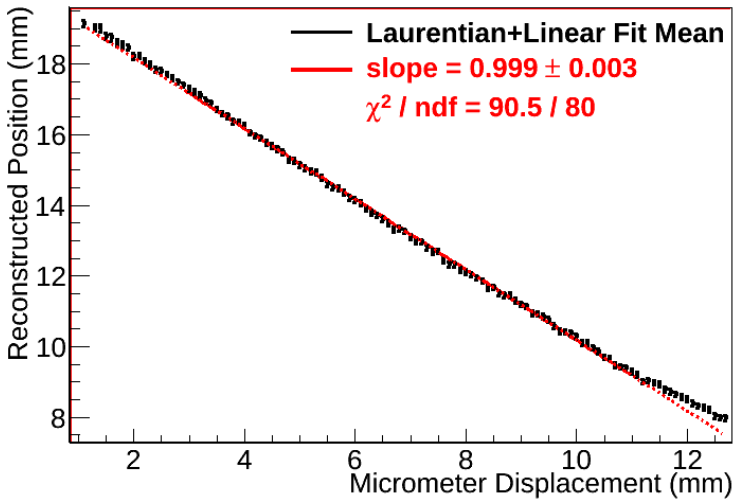

Figure 1.32: Results of the position scan using MP1 panel (table 1.1), each data point is the Breit-Wigner fit mean that corresponds to the position of the source.

the attenuation the signals induced in the panel are carried with four ribbon coax LEMO cables to discriminators (the discriminating threshold for all channels is 216 mV). As a master trigger we used the logical OR from all 24 channels (after passing the threshold). A second set of ribbon coax cables carries the signals from the panel to the Minidaq DAQ system where the time and charge information from the signals induced in the panel is processed and saved for offline analysis.

For this experiment we have connected 11 neighboring high voltage lines to the power supply (corresponding to panel's electrode lines 90 to 100). This gives rise to a working area of 17 $\times$ 11 pixels. Each HV line is separately quenched starting with a 200 MOhm resistors. In the last set of measurements we have changed to 66 MOhm resistors. The high voltage used in all measurements is 860 Volt.

The panel was instrumented on the medical table and the panel's active area was placed perpendicular to the beam . The NIM based electronics (discriminators and logic units) were placed in the patient room near the panel while the VME based Minidaq system was placed in the control room, where a 25 meter long optical fiber connecting the front end electronics with the Minidaq.

In the first set of measurements we used a 6.4 cm thick cylindrical brass collimator with 1 cm diameter hole placed in front of the beam line, but shifted in the X axis (perpendicular to the HV lines) 2.5 cm off of the beam center. In the other measurements we used a 6.4 cm thick cylindrical brass collimator with 1 mm diameter hole directly in the center of the

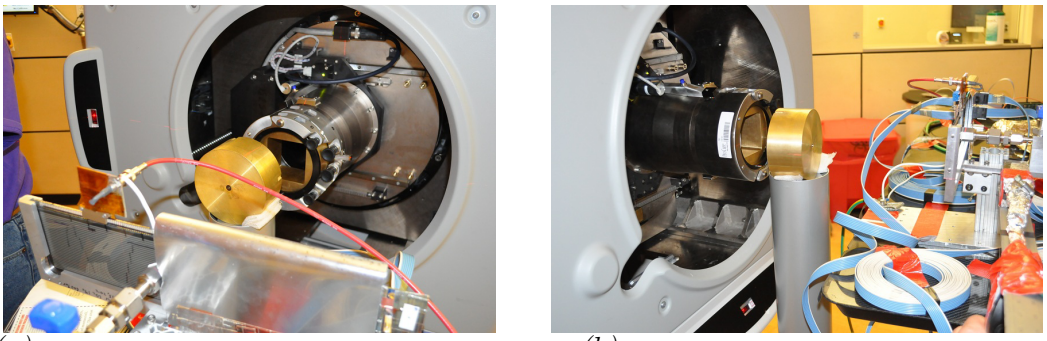

(a) *(b)*

Figure 1.33: Pictures of the IBA proton test beam setup: *(a)* Brass collimator is 2.5 cm off-axis from the center of the beam (the center of the square aperture in the snout), the red cable above the panel is the HV cable *(b)* Side view of the beam snout, the brass collimator and the panel surrounded with all the readout cables.

beam.

As mentioned for the first set of measurements, a 6.4 cm thick cylindrical brass collimator with 1 cm diameter hole was placed in front of the primary aperture with its axis translated by about 2.5 cm away from the beam center (point where the two X and Y lasers are crossing). Being the intrinsic width of the Gaussian beam is 5 mm, this position insured that we were off the beam by 5 standard deviations, and so selecting only an highly reduced fraction of the intensity of the proton beam (roughly 10^{-6} of the rate in the beam center). The shift of the collimator was done in the direction parallel to the readout lines, so that the beam intensity Gaussian varied between the different RO lines, enabling us to eventually see the beam profile movement (on the contrary all HV strips relative to the same RO line had a pretty much uniform illumination throughout the scan). We moved the table (the panel) across in the vertical direction (the HV strips direction). This way the center of the beam moved across the PDP, illuminating different RO lines allowing us to establish the position sensitivity of the detector. We attached a plastic ruler to the panel in order to measure the vertical displacement of the panel (controlled by hand) by aiming the markers on the ruler to the center of the laser, whose width on the ruler is around 2 mm, giving us an error on the positioning of ± 1 mm. For this position scan, we run at a set initial position close to one edge of the instrumented line. Then we shifted the panel by 1 cm and acquired more data, repeating these operations three more times before completing the test going back to the initial position. The hit maps acquired in this procedure are presented in figure 1.34 *(a)*, in which, every hit map (position in the scan) is

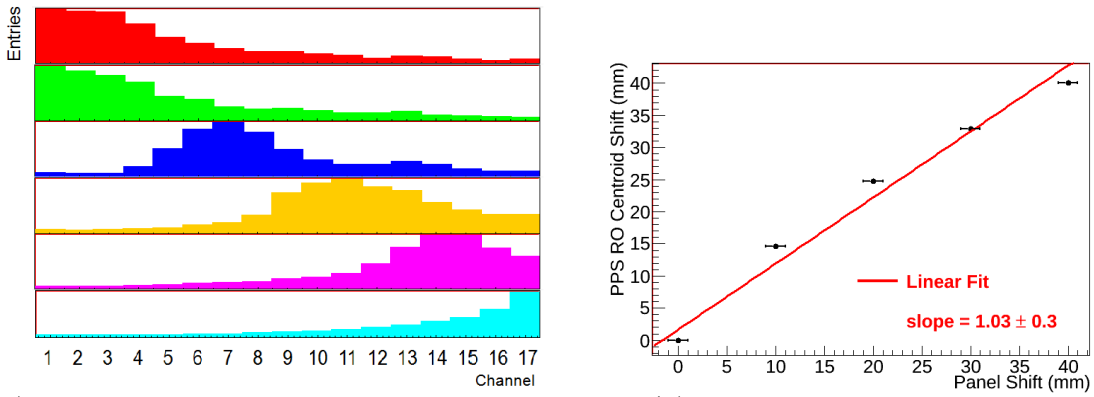

(a) *(b)*

Figure 1.34: Proton beam 1 cm position scan results: *(a)* Position scan with 1 cm aperture collimator shifted from the beam center axis *(b)* Linear fit for the position scan with 1 cm aperture.

drawn in a different color, one above the other. In all these runs all the beam parameters were kept constant (current, delivery time, radiation dose per time interval, ...), as well as the PDP setup and parameters (HV value, HV quenching resistor value, DAQ thresholds, gas content etc.).

A second position scan was performed, starting again from the previous initial position, but this time with a 1 mm collimator and moving the panel by 1 mm each time. When we changed the brass collimator and took a test run, we realized that the beam profile was not Gaussian at all and that the entire active area got sprayed. We suspected that the 1 mm collimator was not aligned with the beam, and since we did not have the tools to realize a good alignment, it was decided to replace the big aperture in the beam nozzle directly with the 1 mm collimator. In this configuration we got the center of the beam and reduced the delivery time from the previous 24 seconds in the 1 cm position scan to 12 seconds. All the other beam and PDP parameters were left unchanged for all 16 runs of this 1 mm translation scan. The hit maps acquired in this procedure are presented in figure 1.35 *(a)*. Again, every hit map (position in the scan) is drawn in a different color, one above the other.

Spatial Resolution and Position Scan Simulations

Based on our position scan data and simulations of the ^{106}Ru source we attempted to examine properties of the panel's resolution using the following equation

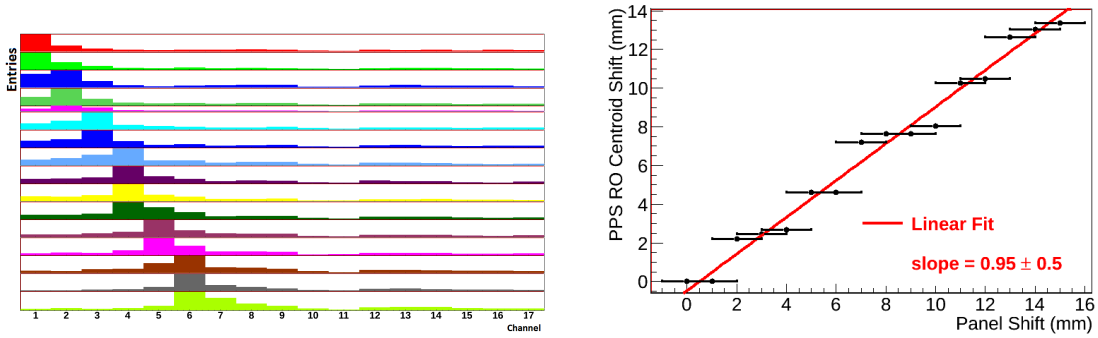

(a) *(b)*

Figure 1.35: Proton beam 1 mm position scan results: *(a)* Position scan with 1 mm aperture collimator aligned with the beam center axis *(b)* Linear fit for the position scan with 1 mm aperture collimator.

$$\sigma_m^2 = \sigma_i^2 + \sigma_s^2, \tag{1.6}$$

where σ_m^2 is taken directly from our data, σ_i^2 is the derived intrinsic resolution of the panel, and σ_s^2 is obtained from the distributions produced in our simulation efforts. GEANT4 simulations of the spatial distribution of betas at the time they enter the gas discharge volume are described in section 3.2. The simulations indicate that, at the top of the gas discharge volume, the Full Width at Half Maximum (FWHM) of the Breit-Wigner distribution of betas is $\sim 2.1 \pm 0.2$ mm. The uncertainty comes from possible degradation of materials in the panel as well as the gas mixture within. We propagated this distribution further through the gas discharge volume with a toy Monte Carlo simulation to produce a final hit map distribution like the ones we see in our data. This represents the spatial distribution of the betas at the point which they interact in the gas discharge volume. The average FWHM after complete simulations however is only ~ 2.6 mm. When compared with the measured width seen in figure 1.31 of 3.1 mm via equation 1.6, the simulated width suggests a poor intrinsic resolution for the panel. However, the resolution of the panel appears to be much better than the 100 μm position scan results shown on figure 1.32.

Noting the discrepancy between the apparent poor intrinsic resolution calculated and what we saw in the 100 μm position scan, we decided to take another look at the role gammas play in our data (our simulations did not account for any interactions that do not come from betas). We used a gamma source, ^{60}Co, on the panel and measured the distribution at several locations. The hit rate for the gamma source was well below that of our beta sources but it couldnt be ignored. We estimated the full width of the gamma

distribution to be about 14 mm. Subsequently, using equation 1.6, we were able to come up with an estimate on the percentage of our events that are produced from gammas interacting in the glass. To do this we assumed a perfect detector resolution (1mm pitch $\Rightarrow \sigma_i = 1/\sqrt{12}$) and we added the width of our GEANT4 simulation that gave us our beta distribution in quadrature with the estimated width of the ^{60}Co gamma distribution. The idea is that, at a certain level, the wider gamma distribution will spread the overall hit map distribution like in equation 1.6. Under these assumptions we estimate that $\sim 7\%$ of our total events in the final hit map are the result of gammas from the source interacting in the glass. So while we are not yet able to constrain the intrinsic resolution of the panel, we do provide an estimate on gamma contribution for ^{106}Ru that gets us closer to understanding the source. There are still more tests to be done in the future to constrain the intrinsic resolution of the panel. Before we can get there we require a better understanding of our radioactive sources, which we are currently developing.

1.5.6 Discharge spreading

In order to test for discharge spreading it is sufficient to use self trigger i.e. any pulse induced in any of the active pixels triggers an event. We use a CAEN v1290 TDC set up with search window of 1 μsec. The NIM signal from every active RO channel is inserted into the TDC (after discrimination) into a different channel. The logic OR from all the channels is used as the trigger. The distribution in figure 1.36 is the multiplicity of pulses induced in the panel per event (for each trigger we count the number of pulses induced in the entire panel). This measurement does not give us the full details about the direction in which the spreading occur (between HV lines RO lines or both). But, the spreading between the RO lines (both in the same HV line and in different HV lines) is given in figure 1.36 for 7% CO2 in Ar at 600 torr. From the multiplicity distribution we see that about twenty percent of the events have at least one extra pulse induced in the panel. A representative timing distribution of the secondary pulses, acquired in the same conditions as the multiplicity measurement is presented for one channel in the panel in figure 1.37. From this timing distribution of the secondary events we see that secondary pulses follow a Landau distribution with Most Probable Value (MPV) of about 100 nsec, therefore can be omitted in the analysis.

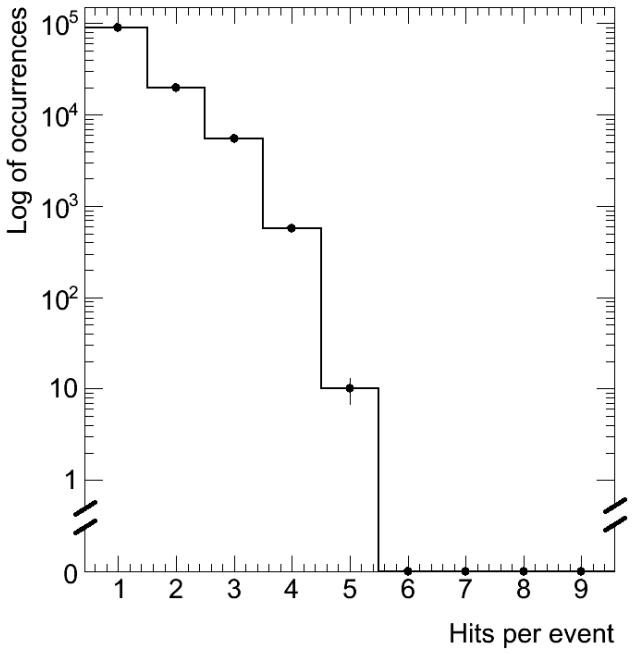

Figure 1.36: Multiplicity of pulses within one event.

1.5.7 Efficiency estimation

From the muon detection experiments we can calculate the panel's efficiency (times acceptance), roughly as

$$\epsilon \times A = \frac{\#(triggers \& signals)}{\#triggers} \tag{1.7}$$

Where ϵ is the efficiency and A is the acceptance taken as the fraction between the triggered events also producing signal in the panel and the total number of triggers. This rough estimation result with total efficiency in the the order of few percent (depending on the operating conditions), an example for the efficiency is shown in figure 1.38, from this example we can see that even though that the raw efficiency is very low ($\mathcal{O}(5\%)$) the muon detection rate is very stable. Few factors should be taken into account when discussing the panel efficiency,

1. The triggered area is much larger than the instrumented area. The scintillators in use for the measurements are 12 in^2, while 31 HV lines and 24 readout lines give rise to total instrumented area of 6.82 in^2.

2. Only a small fraction of the panel's total instrumented area is an active area. For

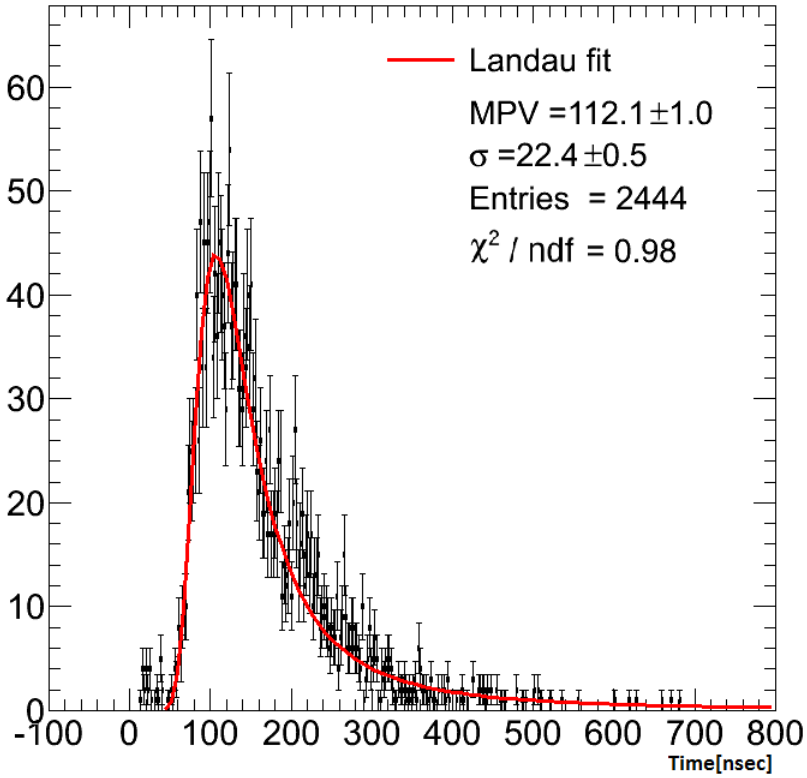

Figure 1.37: Representative arrival time distribution of the secondary pulses induced in one channel in the VPA (2.5 mm pitch) panel. First pulse in the event can be from any of the channels and correspond to arrival time 0 nsec (not shown in in the graph).

the panel in use, this fraction is estimated to be 23.5%.

3. The gas gap in the panel in use is about 385 μm, the average number of primary ion pairs, N_P is determined by the poisson distribution. With Ar as the host gas (a passing MIP resulting with 25 ion pairs per cm Atm [11]) an average of only 0.92 ion pairs is created by a passing cosmic ray muon. Equation 1.8 shows that the probability to get at least one ion pair in the panel by a passing MIP is about 60%

$$P(N_P > 0) = 1 - e^{-0.92} = 0.6 \tag{1.8}$$

By including these factors in the efficiency calculations we find that the individual pixel efficiency is $\mathcal{O}(50\%)$ (only taking into account the area considerations) while the maximum expected efficiency is $\mathcal{O}(60\%)$ (taking into account also the thin gas gap). The calculated efficiency for a few operating voltages is shown in figure 1.39. We find that for 10% CF4 in

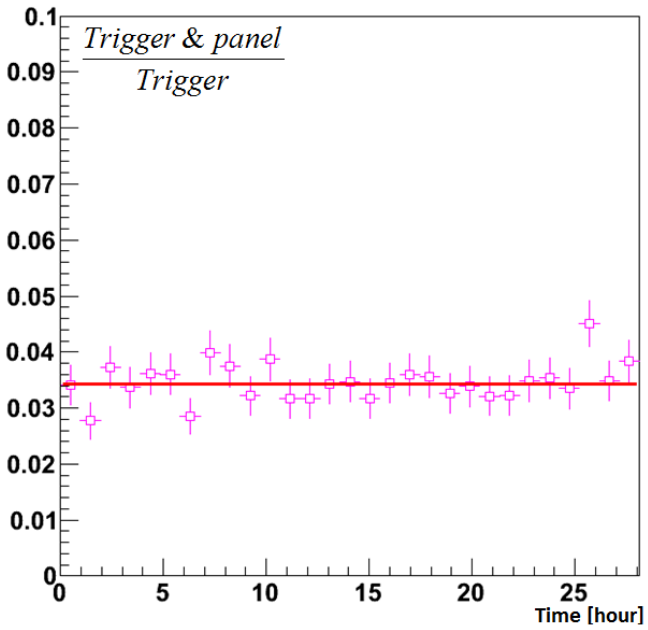

Figure 1.38: Uncorrected efficiency, gas content is 1% CF4 in Ar at 600 torr, applied voltage is 1000 volt.

Ar at 730 torr operating at 1360 volts the corrected pixel efficiency is 53%, which is 88% of the maximum expected efficiency of 60%. In order to validate this calculation we assume:

1. The trigger rate is uniform across the entire triggering area
2. Uniform scintillator response
3. Pixels are binary, i.e the area of the pixel is active and the area around it is not active (no fringe or edge effects)
4. The effective pixel size is constant, i.e the active area does not increase with the applied voltage (the electric field)

1.5.8 Degradation and stability

The materials in use are glass, non-reactive refractory/metal electrodes and inert or non-corrosive gas mixtures. The panels contain no thin-film polymers or plastics used in other micropattern detectors, and no hydrocarbons that can degrade. The first tested panel, sealed at 2003 still produce signals when being subjected to radioactive sources. Non the less, no real measurements have been made in order to test the degradation of the panels in harsh radiation environment to date.

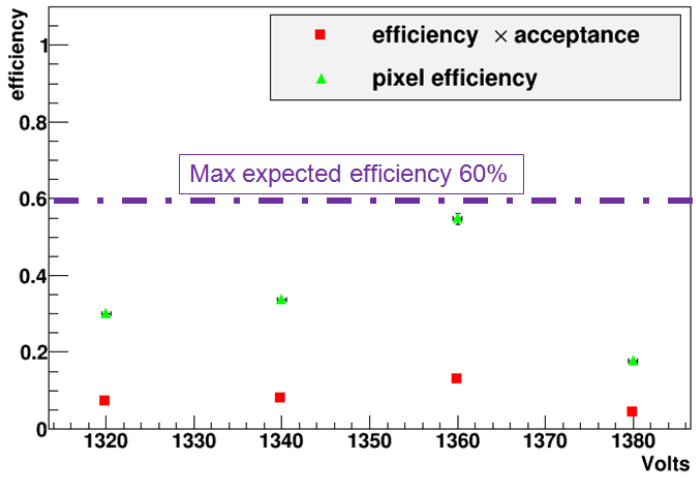

Figure 1.39: Corrected pixel efficiency. Taking into account only the area differences between the instrumented area and the triggered area (red), including the correction arising from the pixels packing fraction (green). The purple dashed line is the maximum expected efficiency

1.6 Plasma Panels Sensors Summary

We have reported on the advances in the PPS development program. We have made detailed measurements of the panel's response to radioactive sources and cosmic ray muons. We have also started to systematically characterize the pulses induced in the panel, thus expanding on our previously reported laboratory results regarding radiation detection with commercial PDPs [26]. We have described the potential attributes of this new gaseous detector that has the potential for inexpensive, hermetically sealed, large area coverage, high resolution, high granularity, and fast timing response performance in an intense radiation environment. We have undertaken a program to develop these detectors in which the first generation prototypes are adapted directly from monochromatic plasma display panels. We have modified these panels to have a mechanical valve/seal system together with a panel baking and gas filling procedure that allows each panel to operate as a stable, portable test chamber for evaluating the PPS device performance as a function of the discharge gas mixture and pressure. These detectors have worked months after being filled with gas and valved off.

We have investigated a number of performance metrics using these inexpensive off-the-shelf commercial devices. The measurement of a PPS characteristic response curve of a

panel (depending on its structure, on the gas mixture and on the bias voltage), allows one to select a quench resistance value to work in a region where the panel is most sensitive, yet not producing self-sustaining discharges. This is a first important step toward a good evaluation of the efficiency of the PPS. We have demonstrated that high gain, fast time response, high spatial resolution and high granularity are achievable. The first prototype detectors have successfully measured high energy muons in a test beam, cosmic rays, medium energy protons, and betas from radioactive sources.

As we transition to discharge cells with better cell physical and electrical isolation, a longer drift space and higher fill factors we expect to achieve lower capacitance and faster discharge times in the sub-nanosecond range, very high position resolution, and improved response to high luminosity sources. We also expect that deeper cells with longer interaction paths will further improve the detector efficiency.

Part II

Search for signals of Physics beyond the Standard Model with the ATLAS detector at the LHC

Chapter 2

Introduction

This part of my thesis describes the search for resonant deviations from the Standard Model (SM) [27–29] in the e^+e^- invariant mass spectrum (the $\mu^+\mu^-$ channel results are shown for completeness). Chapter 3 is based on an analysis of the 7 TeV pp collision data recorded with the ATLAS detector [5] during 2011, corresponding to an integrated luminosity of about 5 fb^{-1}. Chapter 4 is based on an analysis of the 8 TeV pp collision data recorded with the ATLAS detector during the first half of 2012, corresponding to an integrated luminosity of about 6 fb^{-1}.

The thesis reports on two interpretations of the collected data, namely: new heavy spin-1 neutral gauge bosons: Z' and $Z_{\rm KK}/\gamma_{\rm KK}$ [30, 31].

2.0.1 Z'

The benchmark model for Z' bosons is the Sequential Standard Model (SSM) [32], in which the Z' ($Z'_{\rm SSM}$) has the same couplings to fermions as the Z boson. A more theoretically motivated model is the Grand Unification model in which the E_6 gauge group is broken into $SU(5)$ and two additional $U(1)$ groups [33]. The lightest linear combination of the corresponding two new neutral gauge bosons, Z'_ψ and Z'_χ, is considered the Z' candidate: $Z'(\theta_{E_6}) = Z'_\psi \cos\theta_{E_6} + Z'_\chi \sin\theta_{E_6}$, where $0 \leq \theta_{E_6} < \pi$ is the mixing angle between the two gauge bosons. The pattern of spontaneous symmetry breaking and the value of θ_{E_6} determines the Z' couplings to fermions; six different models [32, 33] lead to the specific Z' states named Z'_ψ, $Z'_{\rm N}$, Z'_η, $Z'_{\rm I}$, $Z'_{\rm S}$ and Z'_χ respectively. The expected intrinsic width of the $Z'_{\rm SSM}$ as a fraction of the mass is $\sim 3\%$, while for any E_6 model the intrinsic width is predicted to be between 0.5% and 1.3% [34, 35].

2.0.2 The Kaluza-Klein process

The model proposed in [6] assumes a single extra spatial dimension of size of order TeV^{-1}, compactified onto an S^1/Z_2 orbifold. It predicts Kaluza-Klein (KK) infinite tower of excitations of the gauge bosons, which can decay to dilepton final states in the neutral case. In the minimal model considered here, these KK excited states, denoted by $Z_{\mathrm{KK}}/\gamma_{\mathrm{KK}}$, are of both the photon and the Z (contrary to other Z' models where there is no γ'). This model is completely specified by a single parameter, the compactification scale, which drives the masses of the KK modes.

For this study the process $q\bar{q} \to \sum_n (Z_{\mathrm{KK}}/\gamma_{\mathrm{KK}})_n \to l\bar{l}$ was implemented in PYTHIA8 [7]. In this process, q and $\bar{q}$ are incoming quark and anti quark, and l and $\bar{l}$ are outgoing leptons, At tree-level, the formulation for the differential cross section for the process $f\bar{f} \to \sum\limits_n (Z_{\mathrm{KK}}/\gamma_{\mathrm{KK}})_n \to F\bar{F}$ can be written as

$$\frac{d\hat{\sigma}\,(\hat{s})}{d\cos\theta^*} = 2\pi\frac{\alpha_{\mathrm{em}}^2}{4\hat{s}}\frac{N_C^F}{N_C^f}\frac{\hat{s}^2}{4}\sum_{\lambda_f=\pm\frac{1}{2}}\sum_{\lambda_F=\pm\frac{1}{2}}\left|\sum_{n=0}^{\infty}M_{\lambda_f\lambda_F}^{(n)}\right|^2(1+4\lambda_f\lambda_F\cos\theta^*)^2 \tag{2.1}$$

where $\hat{s}$ is the squared invariant mass of the $q\bar{q}$ state, $N_C^{f(F)}$ is the number of colors of $f(F)$, $\lambda_{f(F)}$ is the helicity of the $f(F)$ fermion and $\cos\theta^*$ is the cosine of the scattering angle with respect to the incoming fermion direction of the outgoing fermions in the $f\bar{f}$ rest frame. The complete amplitude consists of an infinite tower of Kaluza-Klein excitations with increasing mass. For practical reasons in this analysis, the tower is truncated at $n = 10$ since depending on the KK mass, which is simply the inverse of the extra dimension radius ($m_{\mathrm{KK}} \sim R^{-1}$), only the first few excited states can potentially contribute in the current direct-search region.

$$\sum_{n=0}^{\infty}M_{\lambda_f\lambda_F}^{(n)} \equiv M_{\lambda_f\lambda_F} + \sum_{n=1}^{\infty}M_{\lambda_f\lambda_F}^{(n)}, \tag{2.2}$$

where the SM term ($n = 0$) is,

$$M_{\lambda_f\lambda_F} \equiv \frac{e_f e_F}{\hat{s}} + \frac{g_{\lambda_f}g_{\lambda_F}}{\hat{s} - m_{Z^0}^2 + i\hat{s}\frac{\Gamma_{Z^0}}{m_{Z^0}}}, \tag{2.3}$$

and the contribution of the n^{th} excitation for $n = 1, 2, 3, ...$ can be written as,

$$M_{\lambda_f\lambda_F}^{(n>0)}\,(\hat{s}) \equiv \frac{e_f^{(n)}e_F^{(n)}}{\hat{s} - \left(m_{\gamma_{KK}}^{(n)}\right)^2 + i\hat{s}\frac{\Gamma_{\gamma_{KK}}^{(n)}}{m_{\gamma_{KK}}^{(n)}}} + \frac{g_{\lambda_f}^{(n)}g_{\lambda_F}^{(n)}}{\hat{s} - \left(m_{Z_{KK}}^{(n)}\right)^2 + i\hat{s}\frac{\Gamma_{Z_{KK}}^{(n)}}{m_{Z_{KK}}^{(n)}}}. \tag{2.4}$$

The SM helicity couplings [36] of the Z^0 to the incoming and outgoing fermions are,

$$g_{\lambda_f} = \begin{cases} -\dfrac{e_f \sin^2\theta_W}{\sin\theta_W \cos\theta_W} & \text{for } \lambda_f = +\dfrac{1}{2} \\ \dfrac{I_f^3 - e_f \sin^2\theta_W}{\sin\theta_W \cos\theta_W} & \text{for } \lambda_f = -\dfrac{1}{2} \end{cases} \tag{2.5}$$

where the couplings of the KK states to fermions are larger than their SM counterparts (equation 2.5) by a factor of $\sqrt{2}$ [6, 37]. The n^{th} KK excitation masses $m^{(n)}_{Z_{KK}}$ and $m^{(n)}_{\gamma_{KK}}$ are given by,

$$\begin{aligned} m^{(n)}_{Z_{KK}} &= \sqrt{m^2_{Z^0} + (n \cdot m_{KK})^2} \\ m^{(n)}_{\gamma_{KK}} &= n \cdot m_{KK}. \end{aligned} \tag{2.6}$$

where the KK mass, m_{KK}, is dependent on the extra dimension size, R, through the relation $m_{KK} \equiv R^{-1}$.

The total decay width of the Z_{KK} appearing in Eq. 2.4, is given by,

$$\Gamma^{(n)}_{Z_{KK}} = \Gamma_{Z^0} \times 2\frac{m^{(n)}_{Z_{KK}}}{m_{Z^0}} + \Gamma^{(n)}_{Z_{KK}\to t\bar{t}}, \tag{2.7}$$

where $\Gamma^{(n)}_{Z_{KK}\to t\bar{t}}$, , the decay width of the $Z_{KK}(n)$ to $t\bar{t}$ pair, is calculated separately due to the mass of the top quark,

$$\Gamma^{(n)}_{Z_{KK}\to t\bar{t}} = 2\frac{N_C^t G_\mu m^2_{Z^0} m^{(n)}_{Z_{KK}}}{24\pi\sqrt{2}} \left[1 - \frac{4m_t^2}{\left(m^{(n)}_{Z_{KK}}\right)^2}\right]^{\frac{1}{2}} \tag{2.8}$$

$$\times \left[1 - \frac{4m_t^2}{\left(m^{(n)}_{Z_{KK}}\right)^2} + \left(2I_t^3 - 4e_t \sin^2\theta_W\right)^2 \left(1 + \frac{2m_t^2}{\left(m^{(n)}_{Z_{KK}}\right)^2}\right)\right] \tag{2.9}$$

The total decay width of the (massive) γ_{KK} appearing in Eq. 2.4, is,

$$\Gamma^{(n)}_{\gamma_{KK}} = \sum_{F\neq t} \frac{N_C^F \alpha_{\text{em}} m^{(n)}_{\gamma_{KK}}}{6} \times \begin{Bmatrix} 0 & \text{for } n = 0 \\ 4e_F^2 & \text{otherwise} \end{Bmatrix} + \Gamma^{(n)}_{\gamma_{KK}\to t\bar{t}}, \tag{2.10}$$

where the sum is over all the fermionic decay channels, $F\bar{F}$ except for $t\bar{t}$, assuming SM channels only and where $\Gamma^{(n)}_{\gamma_{KK}\to t\bar{t}}$, the decay width of the excited photon to $t\bar{t}$, is,

$$\Gamma^{(n)}_{\gamma_{KK}\to t\bar{t}} = 2\frac{\alpha_{\text{em}} N_C^t m^{(n)}_{\gamma_{KK}}}{6} 2e_t^2 \left[1 - \frac{4m_t^2}{\left(m^{(n)}_{\gamma_{KK}}\right)^2}\right]^{\frac{1}{2}} \left[1 + \frac{2m_t^2}{\left(m^{(n)}_{\gamma_{KK}}\right)^2}\right] \tag{2.11}$$

Eq. 2.1 and 2.2 represent a large tower of interfering contributions at increasing masses and is illustrated in Fig. 2.1.

Contrary to other Z' models, the interference with the Drell Yan (DY) is very strong and is a potentially distinctive feature of this type of models [8, 38]. The exact features of the model considered in this analysis can be found in [8] and the corresponding implementation can be found in [7]. The analysis presented here is the first direct search for this kind of models where previous bounds on the KK mass were obtained from indirect measurements [6, 11].

The invariant mass distributions of the processes $pp \to \gamma/Z^0$ or $Z'_{\rm SSM}$ or $\sum_n (Z_{\rm KK}/\gamma_{\rm KK})_n \to e^+e^-$, can be seen in Fig. 2.2 for the nominal signal masses of 4 TeV. The strong suppression of the cross section for the KK line-shape with respect to the SM is clearly seen for masses below half the mass of the first KK resonance. Note that the $Z'_{\rm SSM}$ does not differ from the SM line-shape as strongly as the KK line-shape and that this difference is generally to increase the cross section with respect to the SM expectation.

The search for the $Z_{\rm KK}/\gamma_{\rm KK}$ took place only in the 2011 analysis (described in chapter 3). In both analyses 2011 and 2012 we have performed the search for Z' (both the benchmark $Z'_{\rm SSM}$ model and the more motivated resulting from the E_6 breaking model) this shall be described in chapters 3 and 4.

The current, indirectly obtained theoretical lower bound for m_{KK} assuming that there are no other beyond-the-SM (BSM) effects besides the KK model, is around 4 TeV [11, 37, 39].

Direct searches at the Tevatron set a limit on the $Z'_{\rm SSM}$ mass of 1.071 TeV [40, 41].

LEP results on Z' searches can be found in the following references [42–46].

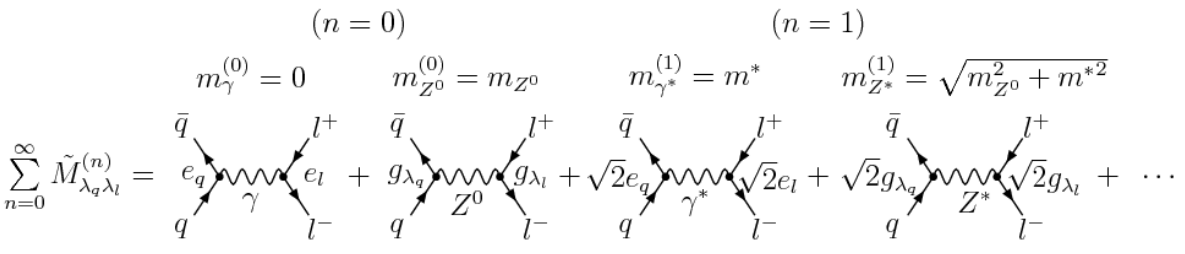

Figure 2.1: *The KK tower of the gauge bosons γ/Z^0 starting from the 0^{th} SM state.*

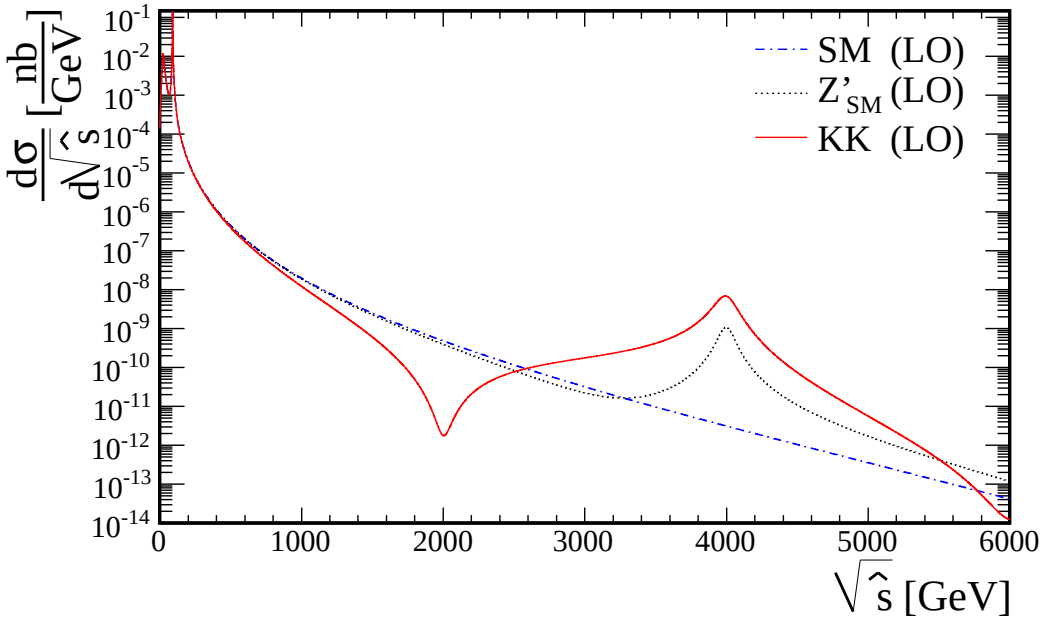

Figure 2.2: *The invariant-mass distributions , $Z_{\mathrm{KK}}/\gamma_{\mathrm{KK}}$(solid red), Z'_{SSM} (dotted black) and the SM γ/Z^0 (dash-dot blue).*

2.1 The ATLAS detector

The ATLAS detector [5] consists of an inner tracking detector surrounded by a 2 T superconducting solenoid, electromagnetic and hadronic calorimeters, and a muon spectrometer. Charged particle tracks in the pseudorapidity[1] range $|\eta| < 2.5$ are reconstructed with the inner detector, which consists of silicon pixel, silicon strip, and transition radiation detectors. The superconducting solenoid is surrounded by a hermetic calorimeter that covers $|\eta| < 4.9$. For $|\eta| < 2.5$, the electromagnetic calorimeter is finely segmented and plays an important role in electron identification. Outside the calorimeter, air-core toroids provide the magnetic field for the muon spectrometer. Three stations of precision drift tubes (with cathode strip chambers for the innermost station for $|\eta| > 2.0$) provide an accurate measurement of the muon track curvature in the range $|\eta| < 2.7$. Resistive-plate and thin-gap chambers provide muon triggering capability in the range $|\eta| < 2.4$.

[1] ATLAS uses a right-handed coordinate system with the z-axis along the beam pipe. The x-axis points to the centre of the LHC ring, and the y axis points upward. Cylindrical coordinates (r, ϕ) are used in the transverse plane, ϕ being the azimuthal angle. The pseudorapidity is defined in terms of the polar angle θ as $\eta = -\ln\tan(\theta/2)$.

Chapter 3

2011 dilepton analysis

This chapter describes the search for heavy neutral gauge bosons (namely $Z'_{\mathrm{SSM}}$and $Z_{\mathrm{KK}}/\gamma_{\mathrm{KK}}$) within the ATLAS experiment. It includes the results from two analyses of pp collisions decaying into l^+l^- pairs at a center-of-mass energy of 7 TeV collected during 2011 at the Large Hadron Collider (LHC) at CERN. It will focus on the analysis of the electron channel but for completeness I will present the results from the muon channel, as well as, the combined results (where applicable). The results described in this chapter were published in [47].

3.1 Samples and Cross sections

3.1.1 Data samples

The data sample used for this analysis was collected in 2011, and corresponds to an integrated luminosity of about 4.9 (e^+e^-) / 5.0 ($\mu^+\mu^-$) fb^{-1} (details in subsections below). In general the format used for the analysis is the D3PD[1].

The data used for this study are required to have been recorded during periods of stable LHC beams, and when all relevant systems of the detector were operating normally i.e. requiring good calorimetry, full inner detector tracking, as well as full solenoidal magnetic field and good EGamma trigger.

The integrated luminosity for this data set is 4.9 fb^{-1}(for the muon channel is 5.0 fb^{-1}).

[1]The format is NTUP_SMWZ and the D3PDMaker tag is p716; The "D3PD" is essentially a flat and compact ROOT [48] ntuple where almost all the event properties are kept while allowing various analyses to be done using this convenient format.

We select events with two electrons with transverse energy, $E_{\mathrm{T}} > 20$ GeV. Detailed information about the electrons are kept, but only for objects with $E_{\mathrm{T}} > 20$ GeV. We also store some general event level information, such as run, event, and lumi block numbers, flags for LAr noise bursts, beam spot position etc. Basic jet information and missing E_T information is also stored. Such selection allows for conducting the analysis, background estimation as well as trigger and identification efficiency performance studies.

Data taken from specific runs included (amounting to about 0.99 fb^{-1}) have a missing region in the LAr calorimeter due to a failure in the readout Front End Boards (FEB). This is taken care of in the data and in the simulation (see section 3.2.4). The equal treatment of the real and simulated data is possible thanks to the simulation closely following the detector conditions (see next section).

For the muon channel we also required the presence of at least one combined *Staco* [49] or *Muid* [50] muon with transverse momentum $p_{\mathrm{T}} > 20$ GeV.

3.1.2 Monte Carlo samples

All samples are generated and fully simulated (using GEANT4 [17]) in the ATHENA MC11 framework [51], with reconstruction in release 17. Table 3.1 lists some of the relevant software tools/generators.

Table 3.1: Simulation software used in the analysis

Program	Version	References
ATHENA	17	[51]
PYTHIA	6.425	[52]
PYTHIA8	8.1	[7]
HERWIG	6.520	[53, 54]
JIMMY	4.31	[55]
CompHEP	4.4.3	[56]
MadGraph	4	[57]
MC@NLO	4.01	[58]
ALPGEN	2.13	[59]

The MC11 samples were produced using 50 ns LHC bunch spacing, which is consistent

with the bulk of the 2011 data. The detector and pile-up conditions varied in the simulation according to the real conditions (detail in table 3.2) and because of using two different generators for pile-up simulation: MC11a and MC11b used PYTHIA8 whereas MC11c used PYTHIA6, which reproduces the data better.

Table 3.2: Simulation conditions.

Data taking period	L_{int} [pb^{-1}]	$<\mu>$	detector conditions	fraction of data	fraction in MC11a	fraction in MC11b/c
B-D	181.2	low	all FEBs OK	3.7%	7%	3.3%
E-H	993.4	low	6 missing FEBs	20.2%	41%	17.8%
I-K	1229.8	low	2 missing FEBs	25.0%	41%	24.2%
L-M	2509.9	high	2 missing FEBs	51.1%	10%	54.7%

Simulated signal processes

MRST2007LO** (LHAPDF set number 20651, also known as MRSTMCal) [60–62] parton distribution functions (PDF) are used for all samples generated with PYTHIA. The cross section calculation is detailed later (section 3.1.3). The full list of simulated signal samples is given in appendix A.1.

For this analyses, we use a 'flat' sample for the Sequential Standard Model (SSM) $Z'(Z'_{\text{SSM}})$, obtained using a modified version of PYTHIA in which the differential cross section is multiplied by the inverse Breit-Wigner and divided by an exponential:

$$\frac{d\sigma}{dm} \rightarrow \frac{d\sigma}{dm} \times ((m^2 - M(Z')^2)^2 + m^2\Gamma(Z')^2) / \exp(-0.00195m)$$

This allows to build as many fully simulated signal "templates" as needed, by reweighting the events according to the desired invariant mass shape. These templates are used in the cross section × Branching fraction (σB) limit setting procedure (see section 3.4).

In addition, smaller signal samples are simulated for a few pole masses (see table A.1 in appendix). The PYTHIA generator is used, with DY and all interferences (between photon, Z and Z') switched on. These samples have a generator level mass cut at half the resonance pole mass to restrict the lower mass range of the Z/γ^*. These samples are used for dedicated studies and for convenience in the figures whenever hypothetical signal is shown.

The KK model signal templates used for this study are produced by reweighting the same DY samples with the analytical 3-dimensional weighting function,

$$\mathcal{W}_0\left(m_{\ell\ell}, \cos\theta^*, q\right) = \frac{\left|\mathrm{DY} + X\right|^2}{\left|\mathrm{DY}\right|^2} \tag{3.1}$$

where DY and X are the amplitudes for DY or X with X being either the KK tower or the Z'_{SSM} (for validations). Both the DY and the X parts are functions of the truth dilepton invariant mass, m_{ee}, the truth lepton $\cos\theta^*$ measured in the $\ell^+\ell^-$ center of mass frame with respect to the truth incoming quark direction, and the incoming quark flavor, q.

The weight can be evaluated precisely at any point in the phase space for any "X" mass where this was validated against the official Z'_{SSM} signal samples (see appendix A.1). For the KK templates, the KK tower, $X = \sum_n \gamma^{(n)}_{\mathrm{KK}}/Z^{(n)}_{\mathrm{KK}}$ is truncated at $n = 10$ for practical reasons, where n is the sequential index of the KK excitation.

Since the full interference structure has to be considered for the KK search, in contrast with the minimal Z' above, we apply the electro-weak (EW) K-factor to the full amplitude: $\mathcal{W}\left(m_{\ell\ell}, \cos\theta^*, q\right) = K_{\mathrm{EW}}\mathcal{W}_0$. In this way, not only the DY and the interference term are modified, but also the pure KK term. We make this approximation because this is the most conservative option; it is also consistent with ATLAS' Contact Interaction analysis [63].

A single KK model signal sample was simulated for $m_{\mathrm{KK}} = 2$ TeV using the Pythia8 generator [7] for validation purpose. The sample was generated in bins of (generator-level) dilepton invariant mass above $m_{\ell\ell} = 120$ GeV (see table A.2 in appendix A.1) with full interferences between the DY and the KK tower.

Simulated background processes

The full list of simulated background samples is given in appendix A.3. The official 2011 pile-up re-weighting tool (Extended Pileup Re-weighting) recovers the same distribution of the number of primary vertices in Monte Carlo as measured in data. QCD background is estimated in a data-driven way (see section 3.2.6).

Drell Yan samples are generated with Pythia using the "ATLAS Underlying Event Tune 2B" (AUET2B) and LO** PDFs. Inclusive $Z \to e^+e^-$ and $Z \to \mu^+\mu^-$ samples covering masses above 60 GeV are used. To ensure adequate statistics at high invariant mass (i.e. above 250 GeV), additional samples are generated in kinematic windows of the

true dilepton invariant mass (150, 200 or 250 GeV-wide ranges, see details in appendix A.3), which are used instead of the high mass tail of the inclusive sample. A $Z \to \tau\tau$ sample was also considered to show that its contribution is completely negligible.

The retuning of MC11 degraded the good agreement between data and Monte Carlo in the p_{T} distribution of the Z candidates, which existed in MC10. Therefore, we apply a re-weighting procedure to the simulated Drell Yan events in order to recover the agreement. This does not affect the rest of the analysis (neither the K-factors calculation nor the selection acceptance).

The W + jets background is generated with ALPGEN to generate matrix elements, JIMMY to describe multiple parton interactions and HERWIG to describe the remaining underlying event and parton showers; AUET2 and CTEQ6L1 [64] PDFs are used.

Diboson samples are generated with HERWIG (same tune and PDFs as PYTHIA) with a filter requiring at least one lepton. Additional samples are generated in two bins of high dilepton invariant mass using a lepton filter and a dilepton mass filter[2]. These events replace the inclusive sample events above 400 GeV.

The $t\bar{t}$ background is generated with MC@NLO to generate matrix elements, JIMMY to describe multiple parton interactions and HERWIG to describe the remaining underlying event and parton showers; AUET2 and CT10 [65] parton distribution functions are used. The top mass is set to 172.5 GeV.

The $t\bar{t}$ and diboson samples have insufficient statistics, therefore a fitting procedure using the functional form $y(x) = p_1 \cdot x^{p_2+p_3 \log x}$ is used to extrapolated at very high mass, namely above 400 GeV for the $t\bar{t}$ sample and 1.4 TeV for the diboson sample.

3.1.3 Cross sections

Signal and Drell Yan cross sections

The signal and SM background cross sections are typically generated using leading-order (LO) matrix elements and the corresponding parton distribution functions (PDFs). The normalization and the shape of these differential cross sections are modified by higher-order QCD and electroweak corrections. However, next-to-leading order (NLO) or next-to-next-

[2]For the WW sample, both Ws are forced, and for the WZ and ZZ samples, one Z boson is forced to decay leptonically at generator level.

to-leading order (NNLO) calculations are typically not available for all the processes of interest. We use NNLO QCD calculations of the DY process to compute a mass-dependent K-factor. We define this K-factor as a function of invariant mass which, when used to multiply the LO differential cross section, yields the NNLO differential cross section as a function of mass. It is conventional to assume that all colorless final states have similar QCD radiation in the initial state, and therefore the K-factor derived for the Drell Yan process can be applied to our signal processes as well: Z' and $Z_{\rm KK}/\gamma_{\rm KK}$.

For the analysis, the simulation samples have been generated using PYTHIA and the LO** PDFs. Therefore we use the $K^{**}_{\rm NNLO}$ to weight our simulated signal and Drell Yan background events as a function of the dilepton invariant mass. Some representative values of $K^{**}_{\rm NNLO}$ are shown in Table 3.3.

Table 3.3: QCD K-factor for several Z' mass points obtained with PYTHIA (LO) and PHOZPR (NNLO) using the central value of MSTW2008 NNLO PDF.

Z' mass [GeV]	250	500	750	1000	1250	1500	1750	2000	2250	2500
$K^{**}_{\rm NNLO}=\frac{\sigma_{\rm NNLO}}{\sigma_{\rm LO**}}$	1.152	1.136	1.121	1.100	1.069	1.025	0.973	0.914	0.853	0.791

Similarly, a mass-dependent electroweak correction is defined to take into account the effects of higher order electroweak corrections. The PYTHIA simulated samples already include real photon emission via the PHOTOS program. We use the HORACE [66, 67] program to calculate the weak K-factor due to virtual gauge boson loops. For convenience, some representative values are shown in Table 3.4. The weak K-factor is not applied to the signal cross section, since this K-factor depends on the W and Z boson couplings to the new boson (Z', $Z_{\rm KK}/\gamma_{\rm KK}$) and is therefore model-dependent.

Table 3.4: Electroweak K-factor for both lepton flavour and for several masses obtained with HORACE using MRST2004QED PDF set.

Mass [GeV]	500	750	1000	1250	1500	1750	2000	2250	2500
$K^{**}_{\rm EW}$ (ee)	1.035	1.019	1.004	0.988	0.972	0.956	0.920	0.881	0.832

The uncertainties on the QCD and EW K-factors are 3% and 4.5% respectively for a 2

TeV Z'. The uncertainty of the QCD K-factor includes variations of the renormalization and factorization scales by factors of two around the nominal scales and the difference in obtained K-factors when computing them for Z/γ^* vs for Z alone. Fig 3.1 shows the PDF uncertainties as well as the different contributions to the uncertainty of the QCD K-factor. The uncertainty in the EW K-factor includes the effects of neglecting the running of the coupling and the real gauge boson emission.

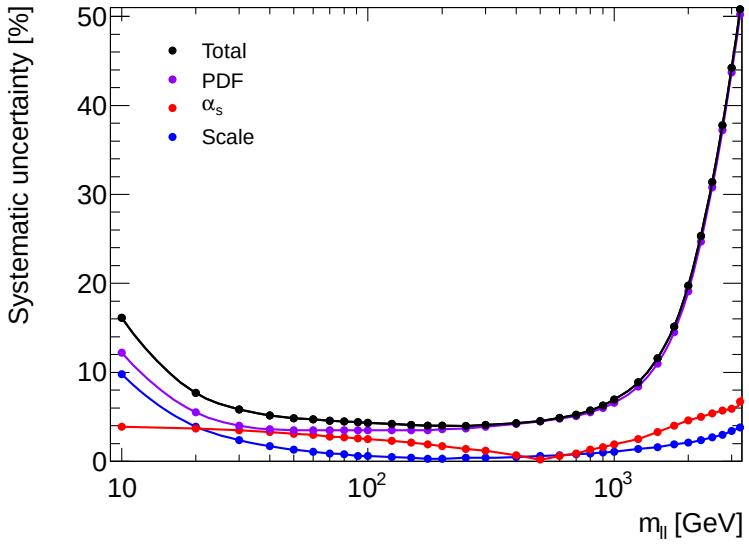

Figure 3.1: Non EW theoretical systematic uncertainties on Drell Yan prediction. The PDF and α_s uncertainties are evaluated using the MSTW2008NNLO sets. The PDF uncertainty is given at 90% C.L.

Other background cross sections

Cross section calculations for W/Z are described in references [68] and [69]. They are performed at NLO and normalized to NNLO in the case of W + jets. The theoretical uncertainties are 5% for inclusive diboson production and about 27.6 % for $W + n$ jets ($n > 0$) production. Cross section calculations for $t\bar{t}$ are performed at approximate-NNLO as described in reference [68]. The related uncertainty is 8.3%.

3.2 Electron Channel

This section describes the dielectron part of the analysis: selection, efficiencies, electron energy corrections, background estimation and data/Monte Carlo comparison.

3.2.1 Electron identification and event selection

The selection criteria used in this analysis are listed below.

- Event was taken during stable operation of the LHC beam, and when all relevant systems of the detector were operating normally;
- Event has at least one primary vertex, with more than 2 tracks;
- Event passes the trigger EF_2g20_loose (demand 2 photons with $P_T > 20$ GeV);
- Event fulfills LArError< 2, which is a variable providing protection against noise bursts and data corruption in the Liquid Argon detector;
- Each electron must have $|\eta| < 2.47$ excluding the crack region $1.37 < |\eta| < 1.52$;
- Each electron must have $p_{\mathrm{T}} > 25$ GeV;
- Each cluster must pass calorimeter quality requirements;
- Each electron must have at least isEM *medium* identification as defined in [70];
- Each electron must have a B-layer hit, if one is expected;
- The leading electron must be isolated ($\mathtt{Iso}_{\mathrm{corr}} < 7$ GeV).

The two highest-E_{T} electrons passing the selection criteria described above are used to reconstruct the dielectron candidate. No requirement is made regarding the charge balance of the two electrons. According to the simulation, this would imply losing about 7% efficiency for a 2 TeV resonance.

Fig. 3.2 shows the event yield per run of the full electron selection normalized to 1 pb^{-1}. The yield is fairly flat and averages to (258.9 ± 0.2) pb. Fitting separately the 4 periods defined in MC, we find a small decrease of the yield in periods E to H, due to the missing FEBs, which is recovered starting from period I. There is a second small decrease during periods L and M, which we attribute to the loss of identification efficiency due to high pile-up conditions.

Table 3.5 shows selected properties of the electrons in the three highest invariant mass events after event selection. An ATLANTIS displays for each of these events is available in appendix E.1.

The full analysis was run on the debug stream[3] and no candidate was retained.

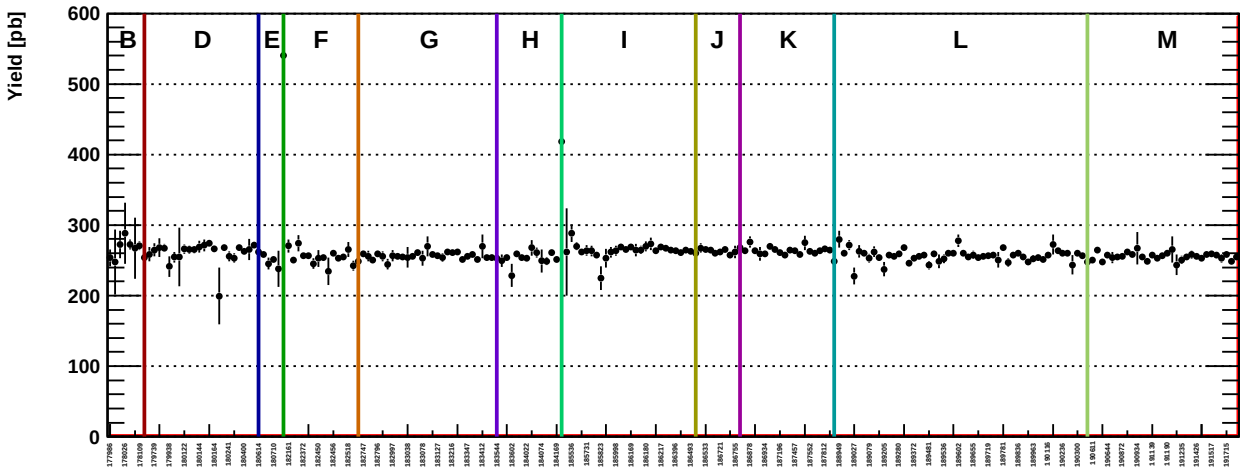

Figure 3.2: Electron channel: yield of the full selection per 1 pb^{-1}, shown by run

3.2.2 Electron trigger and identification efficiency

We measure the trigger efficiency in data using the tag-and-probe method in order to validate the MC trigger simulation in the energy range accessible by the data (electrons with E_T up to ∼200 GeV). In this range, the trigger efficiency is found to be well described by the MC. Nevertheless, scale factors which are very close to 1 are derived as a function of both η and E_{T} and are used to re-weight the MC events. It is assumed that the good agreement between data and MC trigger efficiencies extends to electrons with $E_T > 200$ GeV. Possible inefficiencies at higher energies (due to trigger signals saturation and wrong BCID) have been investigated; no such inefficiencies were found.

Measurements of the electron reconstruction and identification efficiency in data show small differences in the η and E_T distributions. To account for this and similarly to the trigger, a weight is applied to each Monte Carlo event which is the product of η and E_T dependent scaling factors. These scale factors are a combination of the ones provided by the EGamma group [71] for the standard part of the electron selection (electron reconstruction and *medium* level of identification, valid for all MC11 flavours), and additional scaling factors computed specifically for the present analysis to account for differences in data and

[3]There are four streams of data generated based on the trigger decision: Physics stream, calibration stream, express stream and debug stream. The debug stream contains events for which the trigger was not able to make a decision because those events caused failures in some part of the online system.

Table 3.5: Selected properties of the electrons in the events with invariant mass greater than 1 TeV after event selection.

Run, Event	m_{ee} [TeV]	p_T [GeV]	Author	isEM	Q	η	ϕ [rad]	E/p	BL,Si,TRT,HTRT # hits	TRT ratio	Hadronic Leakage	Fside	$\texttt{Iso}_{\text{corr}}$ [GeV]
186721,	1.214	458.98	1	*tight*	1	-0.47	2.51	2.07	1,13,37,13	0.35	0.0006	0.20	0.45
111269544		446.30	1	*tight*	-1	1.14	-0.73	2.06	1,11,35,14	0.40	0.0006	0.29	3.26
186729,	1.132	141.63	1	*medium*	-1	-1.85	1.41	2.17	0,11,26,7	0.27	0.0034	0.20	1.77
251454622		121.57	1	*tight*	1	2.43	-1.75	1.06	2,9,0,0	-	0.0005	0	2.31
187811,	1.068	507.83	1	*tight*	1	0.64	1.43	1.24	1,13,36,10	0.28	0.0001	0.23	0.55
12520737		460.25	1	*tight*	-1	1.55	-1.71	0.41	1,11,38,20	0.53	0.0043	0.23	2.87
189781,	1.083	386.81	1	*tight*	1	-0.49	0.81	0.88	1,13,28,8	0.29	0.0002	0.18	1.74
26763510		382.57	1	*tight*	-1	1.26	-2.42	1.01	2,15,35,24	0.69	0.0001	0.27	1.34
190120,	1.004	303.77	1	*tight*	1	2.38	1.29	8.32	2,13,0,0	-	0.0002	0	1.59
22308590		284.93	1	*tight*	-1	0.12	-1.81	1.39	1,11,32,11	0.34	0.0025	0.23	0.69
190300,	1.658	329.15	1	*tight*	-1	2.00	1.02	1.63	1,11,17,12	0.71	0.0014	0.18	5.62
75300042		216.66	1	*medium*	1	-1.60	-1.83	19.61	1,12,38,12	0.32	0.0044	0.25	2.24
191426,	1.477	522.12	1	*tight*	-1	0.61	0.45	0.62	0,11,31,15	0.48	0.0021	0.19	3.85
165261677		510.31	1	*tight*	1	-1.19	-2.68	4.29	2,13,37,26	0.70	0.0021	0.33	9.38

MC efficiencies of the B-layer and isolation requirements. The resulting combined values are displayed in table 3.6; table 3.7 displays additional correction factors as a function of transverse energy. The scale factors are calculated for each of the two electrons individually and the product is applied to every MC event passing the cut flow.

Table 3.6: Additional scale factors in η for B-layer and isolation requirements (with respect to *medium* identification), valid for MC11a and MC11c. The quoted uncertainties are systematic and statistical.

η	B-layer only	B-layer and isolation
-2.47,-2.37	1.0403 ± 0.0038	1.0398 ± 0.0043
-2.37,-2.01	1.0060 ± 0.0065	1.0059 ± 0.0074
-2.01,-1.81	0.9981 ± 0.0058	0.9983 ± 0.0066
-1.81,-1.52	0.9994 ± 0.0029	0.9996 ± 0.0040
-1.52,-1.37	0.9987 ± 0.0043	0.9965 ± 0.0079
-1.37,-1.15	0.9988 ± 0.0014	0.9987 ± 0.0032
-1.15,-0.8	0.9996 ± 0.0018	0.9997 ± 0.0031
-0.8,-0.6	1.0000 ± 0.0010	0.9998 ± 0.0025
-0.6,-0.1	1.0002 ± 0.0010	1.0000 ± 0.0023
-0.1,0	1.0006 ± 0.0012	1.0006 ± 0.0027
0,0.1	0.9999 ± 0.0008	1.0000 ± 0.0014
0.1,0.6	1.0007 ± 0.0011	1.0006 ± 0.0023
0.6,0.8	0.9998 ± 0.0006	0.9994 ± 0.0017
0.8,1.15	1.0001 ± 0.0013	1.0002 ± 0.0026
1.15,1.37	0.9997 ± 0.0015	0.9997 ± 0.0036
1.37,1.52	0.9989 ± 0.0036	0.9965 ± 0.0073
1.52,1.81	0.9985 ± 0.0036	0.9989 ± 0.0049
1.81,2.01	0.9988 ± 0.0056	0.9984 ± 0.0077
2.01,2.37	1.0037 ± 0.0059	1.0035 ± 0.0071
2.37,2.47	1.0364 ± 0.0056	1.0358 ± 0.0060

Table 3.7: E_{T} correction factors to the scale factors for B-layer and isolation requirements (with respect to *medium* identification), valid for MC11a and MC11c. The quoted uncertainties are systematic and statistical

E_{T} [GeV]	B-layer only	B-layer and isolation
20-25	1.0023 ± 0.0082	1.0018 ± 0.0113
25-30	1.0014 ± 0.0052	1.0011 ± 0.0084
30-35	1.0001 ± 0.0043	1.0003 ± 0.0073
35-40	1.0003 ± 0.0034	1.0006 ± 0.0054
40-45	0.9999 ± 0.0027	1.0001 ± 0.0043
45-50	0.9994 ± 0.0025	0.9996 ± 0.0040
50-60	0.9994 ± 0.0027	0.9995 ± 0.0044
60-80	0.9982 ± 0.0029	0.9979 ± 0.0044
> 80	0.9973 ± 0.0030	0.9959 ± 0.0047

3.2.3 Electron energy smearing and rescale

At the energies relevant to this analysis, the resolution is dominated by the constant term, denoted c in the following parametrization: $\sigma(E)/E = a/\sqrt{E} \oplus b/E \oplus c$, where $\oplus$ represents addition in quadrature, and E is the energy in GeV. The latest published constant term values measured in data are 1.2% in the barrel and 1.8% in the endcaps [70]; we use the latest unpublished results of this measurement, namely $(0.97 \pm 0.02)\%$ in the barrel and $(1.64 \pm 0.06)\%$ in the endcaps. The simulation is adjusted to reproduce this resolution: the energy is smeared using the EGamma official tool [72]. In the end, the uncertainty on the resolution has a negligible effect. Furthermore the data energies are corrected by values provided by the EGamma group, which were obtained using the Z peak for calibration [72].

All these corrections are derived from data at energies basically below 200 GeV. We check the behaviour at higher energies with the simulation and find that both energy resolution and bias are expected to improve with increasing energies.

3.2.4 LAr front-end board failure

From data taking run 180614 to run 184169 (periods E-H, ~ 0.99 fb^{-1} of data), 6 front-end boards (FEBs) in the Liquid Argon calorimeter were defect due to hardware problems. A region of $\Delta\phi = 0.2, \Delta\eta = 1.4$, centered at $\phi = -0.7$ and $\eta = 0.7$, in EMBA (barrel) was lost, which corresponded to 0.8% of the precision coverage. Both in data and MC, this bad detector region is taken into account by applying the electron Object Quality flag. It was shown in [73] that the absolute acceptance loss for a Z' signal was about 3%, therefore the net effect in the full data sample is $\sim 0.5\%$.

3.2.5 Signal efficiencies

The overall acceptance times efficiency ($\mathcal{A}\epsilon$) of the final selection for the Z'_{SSM} 'flat' samples are displayed in Figure 4.2 as a function of the dielectron mass. For the $Z_{\mathrm{KK}}/\gamma_{\mathrm{KK}}$ signal, the very high statistic Z/γ^* samples are used, instead of flat samples, when building the signal templates. The angular distributions of DY and Z'_{SSM} are very close, although not strictly identical; the resulting acceptances are therefore very close.

In order to give an idea of the relative efficiencies of each step of the selection, Table 3.8 shows the cut flows measured in 2 TeV Z'_{SSM}. It should be noted that the Z'_{SSM} 2 TeV sample is generated with DY and full interference, contrary to the flat sample; the final efficiency of the cut flow can therefore be slightly different from the one displayed in Figure 3.3.

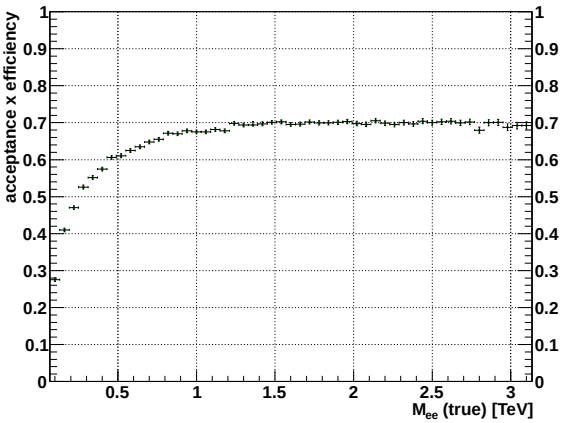

Figure 3.3: Electron channel: total acceptance times efficiency as a function of m_{ee} for Z' (and $Z_{\mathrm{KK}}/\gamma_{\mathrm{KK}}$)

Table 3.8: Cut flows for the electron channel at 2 TeV

Selection	Z'	
	Relative efficiency	Absolute efficiency
Primary Vertex	100.00	100.00
Trigger	90.12	90.12
η	96.45	86.71
p_{T}	95.81	83.08
Object Quality	98.24	81.62
Both *medium*	90.76	74.08
B-layer	97.68	72.36
Isolation	98.24	71.08
Mass Window	99.99	71.07

3.2.6 Background Estimation

All backgrounds are modeled using Monte Carlo simulation except the QCD plus W + jets background which is measured directly from data[4].

It was shown for the analysis of ATLAS presented at the EPS 2011 conference (EPS2011) [73] that the background arising from conversions from direct photon production (gamma-jet and diphoton) is negligible compared to diboson production, therefore it is neglected here.

Four different methods are used to estimate the QCD & W + jets background.

The first technique, referred to as the "Reverse identification" (or "Reverse ID") technique, it only measures the QCD background. It uses a template fit in m_{ee}, performed in the range 70-200 GeV, to determine the amount of QCD multijet background. The fit uses two templates that are allowed to float: a Drell Yan plus W + jets plus $t\bar{t}$ plus diboson template (all normalized relatively to each other according to their cross sections) taken from Monte Carlo, and a QCD template, built from real data by reversing identification cuts. The same method was used for the ATLAS analysis presented at the Moriond 2012 conference (Moriond2012), with a change in the reversed identification cuts: former anti

[4]To be precise, the Reverse ID method still uses the W + jets MC, but the three other methods are fully data driven.

strip cuts are now replaced by anti track-match cuts, which seems to increase the statistics and lower the contamination by real electrons. In order to form the QCD template, the invariant mass distribution obtained by applying the reverse identification cuts is fitted with the functional form $y(x) = p_1 \cdot x^{p_2+p_3 \log x}$ (the so called "dijet" function) to smooth the shape and extrapolate to high invariant masses.

The second technique, referred to as the "Isolation fits" technique, also employs template fitting, but on two-dimensional (leading and sub-leading) $\texttt{Iso}_{\text{corr}}$ distributions in bins of m_{ee}.

A third independent data-driven estimate was carried out using QCD fake rates measured from inclusive jet samples, and is an update of what had been done for EPS2011 [73] and Moriond2012 [74]. A fourth and last method ("Fake factors (EGamma stream)") also computes fake rates, but from the EGamma stream instead, using the same trigger as in the signal selection.

Table 3.9 and figure 3.4 show a comparison of the QCD plus W + jets estimates using the four described methods. Since all but the Reverse ID method do not provide separate estimates for QCD and W + jets contributions, the comparison is done on the sum. For the reverse ID method, the W + jets component is taken from MC (as described above).

The four methods agree within their large uncertainties.

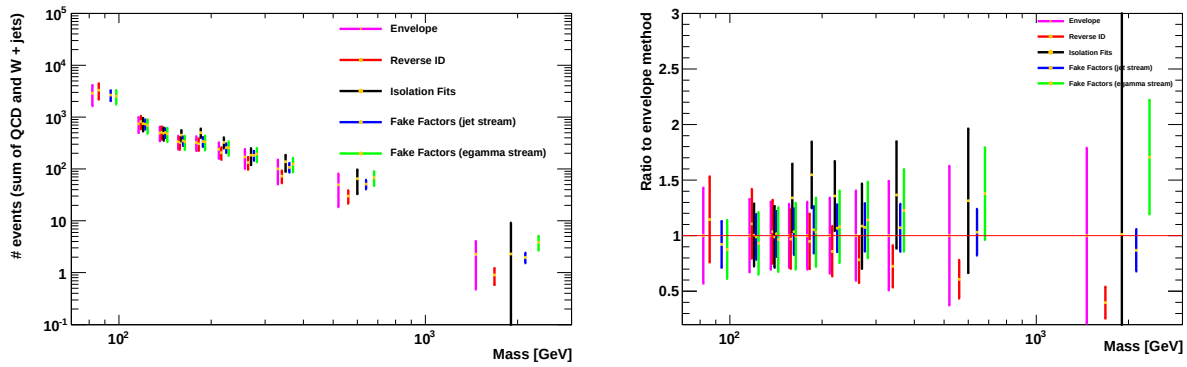

Figure 3.4: Comparison of the four methods used in electron QCD background evaluation. Displayed are the total numbers of events for the (QCD plus W + jets) contributions summed up. The right graph shows the ratio of the isolation fit and fake rate (jet and EGamma) methods to the baseline method (enveloppe)

Combination of the different methods is done via averaging of the central values and taking the envelope of the error bands as uncertainty, and is shown in figure 3.5. The

Table 3.9: Comparison of the four methods used in electron QCD background evaluation. Displayed are the total numbers of events for the (QCD plus W + jets) contributions summed up. If a method does not provide an estimate for a mass bin, the entry is marked by N/A

Method / mass range [GeV]	70 - 110	110 - 130	130 - 150	150 - 170	170 - 200
Envelope	2885.66	740.35	493.65	335.84	322.14
Reverse ID	3304.60	818.98	510.85	325.33	305.49
Isolation Fits	N/A	744.60	488.34	449.89	498.18
Fake Factors (jet stream)	N/A	732.34	501.62	347.93	339.14
Fake Factors (egamma stream)	2525.66	689.17	475.71	334.18	332.22
Method / mass range [GeV]	200 - 240	240 - 300	300 - 400	400 - 800	800 - 3000
Envelope	239.72	170.09	100.65	49.52	2.27
Reverse ID	205.97	133.26	72.88	30.07	0.90
Isolation Fits	325.43	184.55	137.50	65.07	2.29
Fake Factors (jet stream)	255.83	182.87	107.76	51.03	1.97
Fake Factors (egamma stream)	258.72	194.11	123.53	68.24	3.87

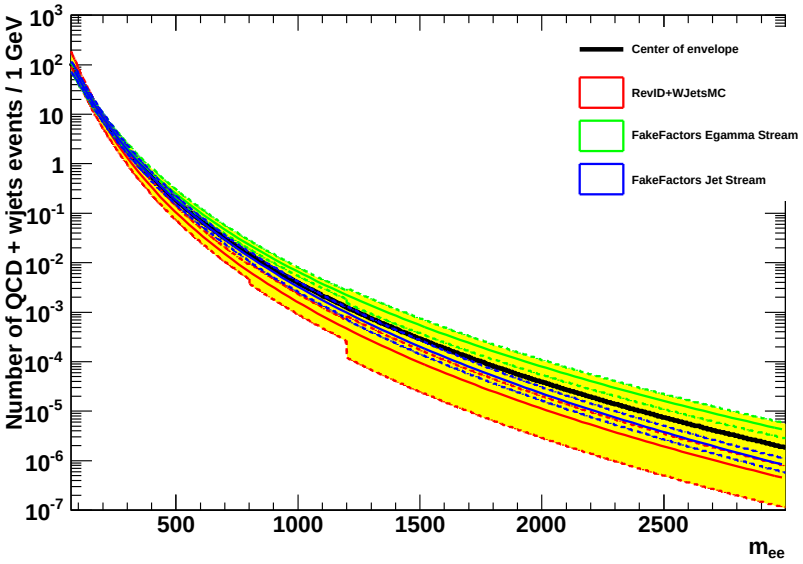

Figure 3.5: Combination of the QCD plus W + jets via the background envelope method. The central value of the envelope is shown in black with the yellow error band. The separate methods are shown as colored lines with their uncertainty band shown with dashed lines in the same color

"isolation fits" method is only used as a cross-check and not used in the average, because of too large uncertainties (e.g. an intrinsic 300% relative uncertainty at 800 GeV).

The average of the central values is done in 1 GeV steps using the fitted functions which describe the mass shapes of the individual methods. The uncertainty is assigned to be the maximum of the largest deviation up and down. For this uncertainty estimation, the method's central values and the one sigma fluctuations of their uncertainties are taken into account.

For the total background evaluation, the QCD plus W + jets (taken from the envelope combination) and the Monte Carlo components are summed; the total background is scaled such that the number of events matches the number of data events in the 70-110 GeV range. The resulting MC normalization factor is 1.0395. Using the Reverse ID method, a normalization factor of 1.039 is found.

3.2.7 Data - Monte Carlo Comparison

The invariant mass of the electron pair (m_{ee}) distribution for selected events is shown in Fig. 3.6 for the data and the expected SM background. Three Z'_{SSM} signals are overlaid for illustration. The invariant mass of the electron and muon pairs ($m_{ee}$and $\mu^+\mu^-$) distributions for selected events are shown in Fig. 3.7 for the data and the expected SM background. Three $Z_{\mathrm{KK}}/\gamma_{\mathrm{KK}}$ signals are overlaid for illustration. Table 3.10 shows the number of observed and expected events in bins of reconstructed m_{ee}. The number of observed events in the normalization region, from 70 to 110 GeV, is 1236646.

Table 3.10: Expected and observed number of events in the dielectron channel. The errors quoted include both statistical and systematic uncertainties. The systematic uncertainties are correlated across bins.

m_{ee}[GeV]	110–200	200–400	400–800	800–1200	1200–3000
Z/γ^*	26700 ± 1100	2960 ± 120	265 ± 13	12.1 ± 0.9	1.47 ± 0.18
$t\bar{t}$	1300 ± 120	410 ± 40	26.5 ± 2.8	0.41 ± 0.17	0.034 ± 0.034
Diboson	415 ± 21	146 ± 8	16.2 ± 0.9	0.88 ± 0.05	0.101 ± 0.011
QCD and W + jets	1900 ± 600	510 ± 200	50 ± 31	2.0 ± 1.8	0.26 ± 0.31
Total	30300 ± 1300	4030 ± 240	357 ± 34	15.4 ± 2.0	1.86 ± 0.35
Data	29816	4026	358	17	3

Figure 3.8 shows the E_{T} distributions of the leading (highest E_{T}) and sub-leading (second highest E_{T}) electron after full event selection. Figures 3.9 and 3.10 show the η and ϕ distributions of the two electrons respectively. Figure 3.11 shows the p_{T} and rapidity distributions of the electron pair. All these kinematic plots are produced using an average of the Reverse ID and Fake factors (EGamma stream) methods for the QCD and W + jets component; only the invariant mass distribution uses the baseline combination of the three methods.

Figure 3.12 shows the isolation distribution for the leading electron after full event selection but without the isolation cut. The isolation of both leading and sub-leading electrons are shown after the full event selection, including isolation selection, on figure 3.13; it should be kept in mind that neither the QCD nor the W + jets components have any

isolation requirement.

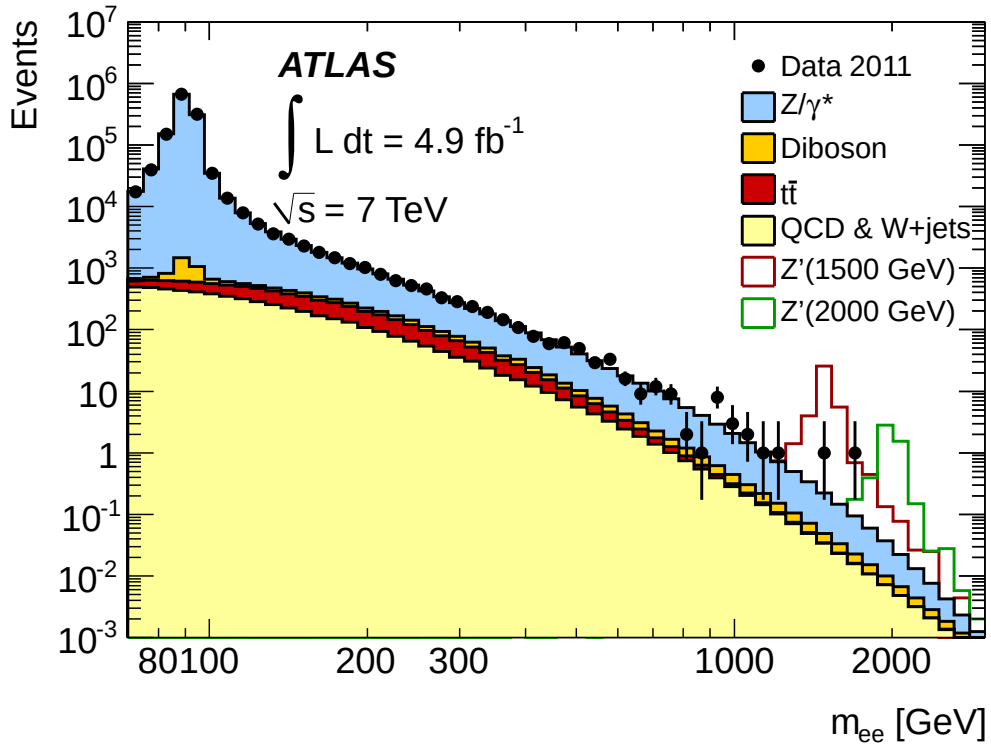

Figure 3.6: Dielectron invariant mass (m_{ee}) distribution after event selection with selected SSM Z' signals overlaid

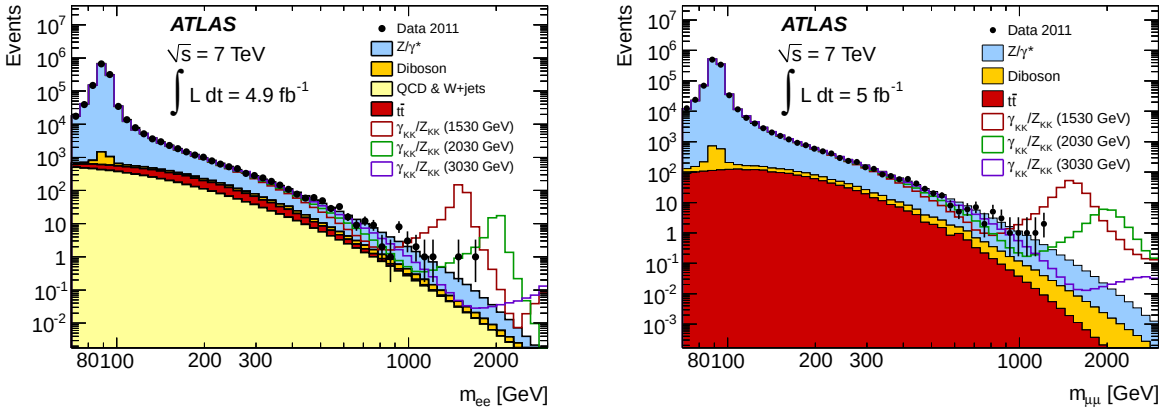

Figure 3.7: Dielectron invariant mass m_{ee} (left) and dimuon invariant mass $m_{\mu\mu}$ (right) distributions after event selection, with selected $Z_{\mathrm{KK}}/\gamma_{\mathrm{KK}}$ signals overlaid

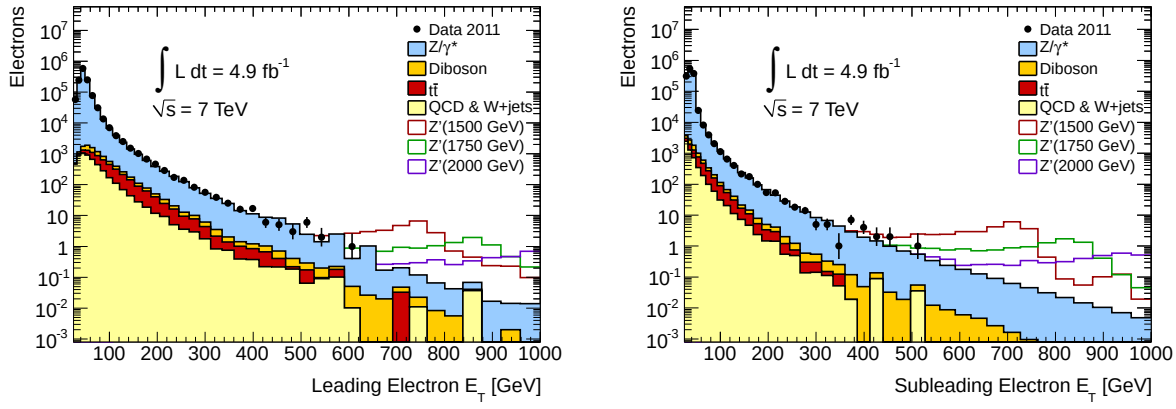

Figure 3.8: E_{T} distribution for the leading (left) and sub-leading (right) electron after event selection. As described in section 3.1.2, the signal shapes come from dedicated samples generated at a given mass point.

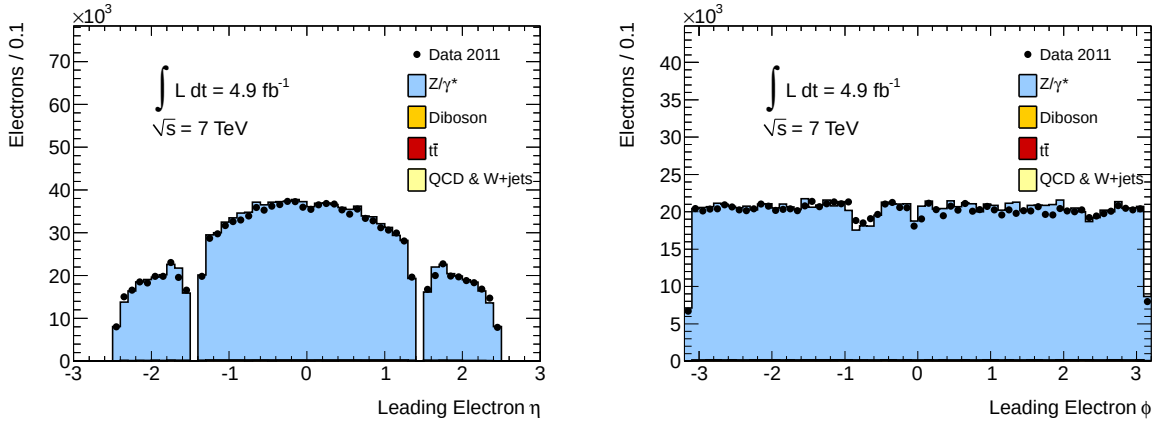

Figure 3.9: η and ϕ distributions for the leading electron after event selection

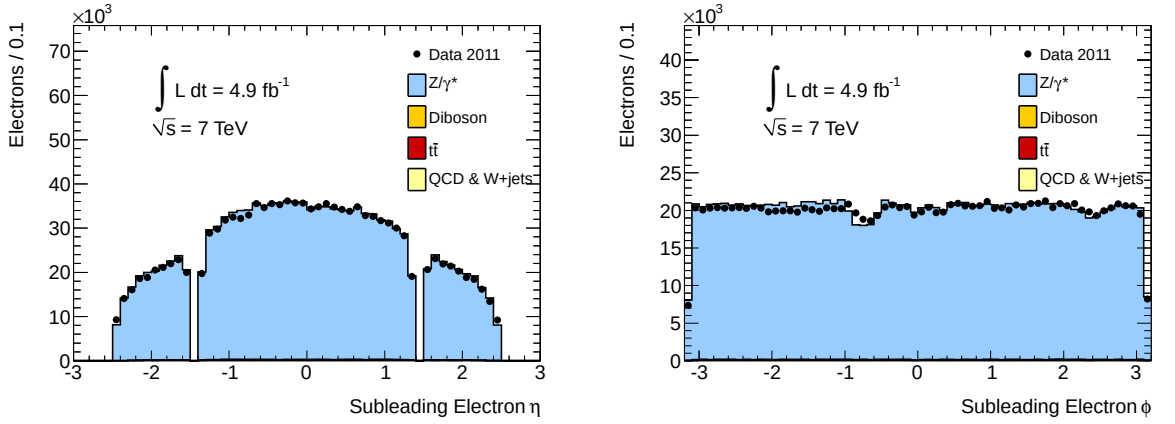

Figure 3.10: η and ϕ distributions for the sub-leading electron after event selection

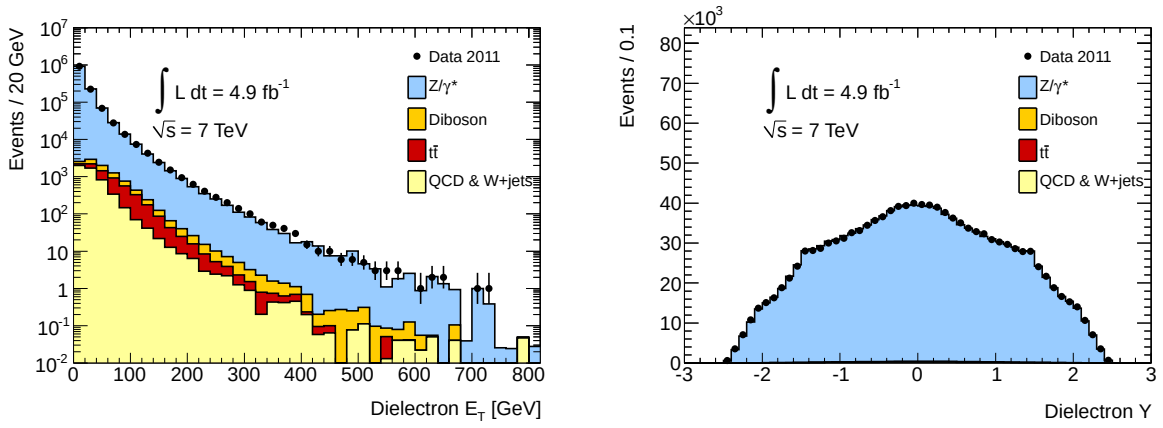

Figure 3.11: Dielectron p_T and rapidity after event selection

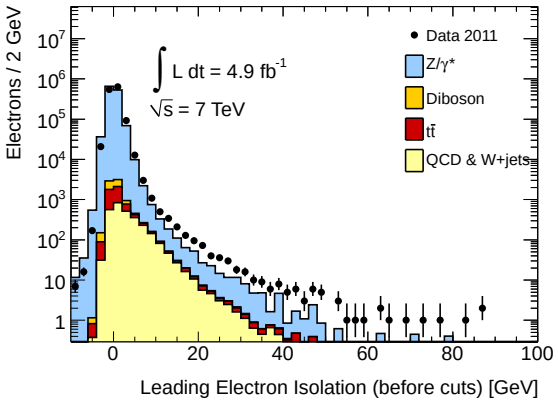

Figure 3.12: Corrected calorimeter isolation ($\texttt{Iso}_{\text{corr}}$) for the leading electron after the full event selection except the $\texttt{Iso}_{\text{corr}} < 7$ GeV and $m_{ee} > 70$ GeV selections

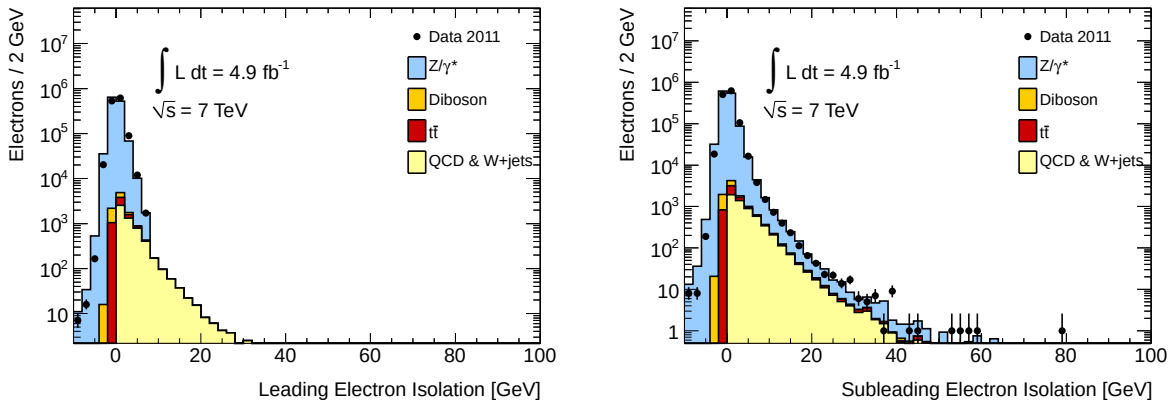

Figure 3.13: Corrected calorimeter isolation ($\texttt{Iso}_{\text{corr}}$) for the leading electron (left) and sub-leading (right) electron after event selection, including applying $\texttt{Iso}_{\text{corr}} < 7$ GeV on the leading electron

3.3 Systematic uncertainties

The systematic uncertainties in this analysis are reduced by the fact that the backgrounds are normalized to the data in the region of the Z peak. This procedure makes the analysis insensitive to the uncertainty on the integrated luminosity as well as other mass-independent systematic uncertainties. In the signal search and limit setting, mass-dependent systematic uncertainties are incorporated as nuisance parameters whose variation is integrated over in the computation of the likelihood function [75]; most are small at low mass and grow at high mass.

The main systematic uncertainties of this analysis are listed in tables 3.11, 3.12 and 3.13. They include theoretical effects due to the PDF, QCD and electroweak corrections, as well as experimental effects, namely efficiency and resolution. These uncertainties are correlated across all bins in the search region. In addition, there is an uncertainty on the QCD component of the background affecting the electron channel. We assume that the experimental uncertainties are correlated between signal and all types of backgrounds. A flat uncertainty of 5%, due to the uncertainty on the Z/γ^* cross section in the normalization region, is assigned to the signal expectation. According to group recommendations, no theoretical uncertainties are applied on the signal expectation when setting limits.

A more detailed description of the uncertainties is listed below. The uncertainty on the PDF is 4% at 200 GeV, 7% at 1 TeV and 20% at 2 TeV for both channels. It is obtained by variations of the parameter set, and also contains uncertainties due to α_S variations, as well as uncertainties on the QCD corrections: variations of the renormalization and factorization scales by factors of two around the nominal scales, which are added linearly. Furthermore the largest difference in obtained K-factors for Z and Z/γ^* production is added. Using the difference in NNLO and NLO cross sections, we obtain a comparable estimate.The uncertainty of the electroweak corrections is 4.5% at 2 TeV for both channels, and includes the effects of neglecting real boson emission, the difference in the electroweak scheme definition between Pythia and Horace, and higher order electroweak and $\mathcal{O}(\alpha\alpha_s)$ corrections.

On the experimental side, the systematic effects are as follows. In the electron channel, we assign a systematic uncertainty for the electron reconstruction and identification efficiency at high p_{T} of 2% at 2 TeV. This uncertainty is estimated by studying the mass dependence of adding the calorimeter isolation cut and affects both signal and background

expectations. The calorimeter resolution is dominated at large transverse energy by a constant term which is 1.0% (1.2% in the latest public reference [70]) in the barrel and 1.6% (1.8% in the latest public reference) in the end-caps with a small uncertainty [72]. The simulation was adjusted to reproduce this resolution at high energy and the uncertainty on it has a negligible effect. The calorimeter energy calibration uncertainty is between 0.5% and 1.5% depending on transverse momentum and pseudorapidity. The non-linearity of the calorimeter response is negligible according to test beam data and Monte Carlo studies [76]. The uncertainty on the energy calibration has minimal impact on the sensitivity of the search, since its main effect is a shift of a potential peak in dilepton mass without change of the line-shape. Finally, the QCD multijet background has a large systematic uncertainty, which translates into a systematic uncertainty on the total background of 7% at 200 GeV, 12% at 1 TeV, and 26% at 2 TeV. This number is obtained by taking a ratio of the total background, where the QCD background was increased by 1 σ, and the total nominal background.

For the muon channel, the combined uncertainty on the trigger and reconstruction efficiency was estimated to be 6% at 2 TeV. This uncertainty is dominated by a conservative estimate of the impact from large energy loss from muon Bremsstrahlung in the calorimeter which may interfere with reconstruction in the muon spectrometer. We are using the uncertainty that was evaluated for this source in the context of the EPS2011 analysis, which is documented in [73]. The uncertainty on the resolution due to residual misalignments in the muon spectrometer propagates to a change in the observed width of signal line-shape, and affects the sensitivity of the search. However, this effect leads to a loss of less than 3% of the events in the Z' signal peak at 2 TeV ($\pm$ one RMS), so it is neglected in the likelihood. The muon momentum scale is calibrated with a statistical precision of 0.1% using the $Z \to \ell^+\ell^-$ mass peak. As with the electron channel, the momentum calibration uncertainty has negligible impact in the muon channel search. The effect of pileup on the total signal acceptance are negligible. Finally, the extrapolation of the $t\bar{t}$ and diboson invariant mass shape has a systematic uncertainty which is less than 3% relative to the total background at all invariant masses.

Uncertainties of 3% and under at 2 TeV are neglected in the statistical treatment described below.

Table 3.11: Summary of systematic uncertainties on the expected numbers of events at $m_{\ell\ell} = 200$ GeV. NA indicates that the uncertainty is not applicable, and "-" denotes a negligible entry (i.e. $< 3\%$). The uncertainty on the PDF includes the QCD corrections uncertainty

Source	Dielectrons		Dimuons	
	Signal	Background	Signal	Background
Normalization	5%	NA	5%	NA
PDF/α_s /scale	NA	4%	NA	4%
W + jets and QCD background	NA	7%	NA	-
Total	5%	8%	5%	4%

Table 3.12: Summary of systematic uncertainties on the expected numbers of events at $m_{\ell\ell} = 1$ TeV. NA indicates that the uncertainty is not applicable, and "-" denotes a negligible entry (i.e. $< 3\%$). The uncertainty on the PDF includes the QCD corrections uncertainty

Source	Dielectrons		Dimuons	
	Signal	Background	Signal	Background
Normalization	5%	NA	5%	NA
PDF/α_s /scale	NA	7%	NA	7%
Efficiency	-	-	3%	3%
W + jets and QCD background	NA	12%	NA	-
Total	5%	14%	6%	8%

3.4 Results

3.4.1 Discovery statistics

We test the consistency of the observed data with the standard model prediction using several methods.

Template shape fitting

First, we use the template shape fitting technique and search for a Z' signal of unknown mass and unknown rate in ATLAS dilepton data. Template shape fitting is essentially a

Table 3.13: Summary of systematic uncertainties on the expected numbers of events at $m_{\ell\ell} = 2$ TeV. NA indicates that the uncertainty is not applicable, and "-" denotes a negligible entry (i.e. $< 3\%$). The uncertainty on the PDF includes the QCD corrections uncertainty

Uncertainty source	Signal	Drell-Yan	Other backgrounds	Signal	All backgrounds
Normalization	5%	NA	NA	5%	NA
PDF/α_s /scale	NA	19%	19%	NA	19%
Electroweak corrections	4.5%	4.5%	NA	NA	4.5%
Efficiency	6%	6%	6%	6%	6%
Resolution	4.5%	4.5%	4.5%	4.5%	4.5%
Diboson and $t\bar{t}$ tail fit	NA	NA	12%	NA	1.3%
Total	9%	21%	24%	9%	21%

counting experiment in many bins of the m_{ll} distribution and the likelihood function is the product of the single bin counting experiment likelihood function.

The significance of a potential Z' signal is summarized by a p-value, the probability of observing an outcome of an analysis at least as signal-like as the one observed in data, assuming that a signal is absent. The common convention is that a p-value less than 1.35×10^{-3} constitutes evidence for a signal and a p-value less than 2.87×10^{-7} constitutes a discovery. These are one-sided integrals of the tails of a unit Gaussian distribution beyond $+3\sigma$ and $+5\sigma$, respectively.

Experimental outcomes are ranked on a one-dimensional scale using a test statistic that is used to calculate the p-value. A natural choice for the test statistic is based on the Neyman-Pearson lemma which states that when performing a hypothesis test between two hypotheses - in our case one assuming the presence of signal and background (S+B) and one hypothesis that assumes only SM background (B) - the log-likelihood-ratio (LLR) $LLR = -2ln\frac{L(S+B)}{L(B)}$ is the best test to reject (B) in favor of (S+B).

Since the mass and the rate of a hypothetical Z' is unknown *a-priori*, we perform a likelihood fit for the best-fit signal cross section ($\sigma_{Z'}$) and the best-fit mass of Z' ($M_{Z'}$) present in data. This approach accounts naturally for the 'look elsewhere effect'.

Figure 3.14 shows the absolute value of the LLR test statistic as a function of $\sigma_{Z'}$ and $M_{Z'}$ for the likelihood fit to ATLAS data in the dielectron (left) and dimuon channel

(right), while Figure 3.15 shows the same for the combination of all channels.

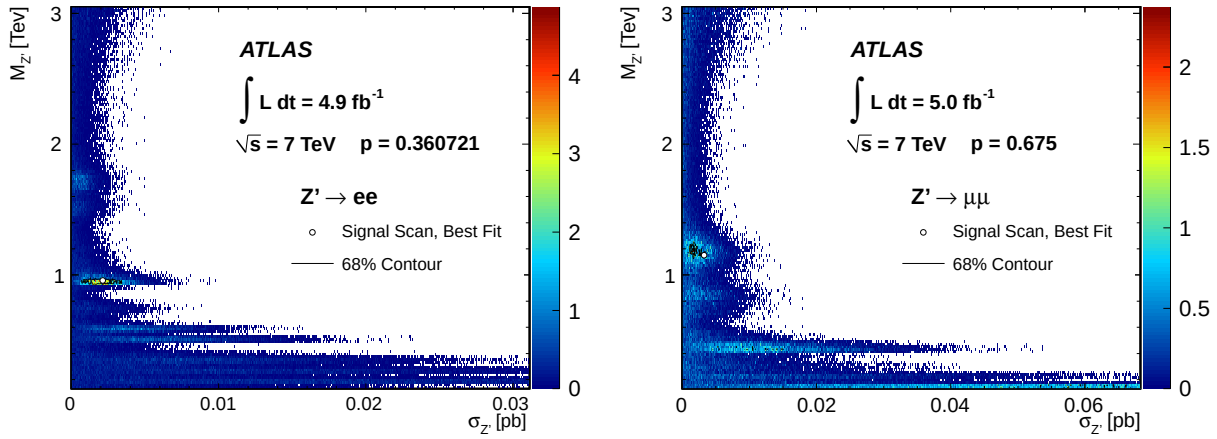

Figure 3.14: Absolute value of the log-likelihood-ratio test statistic as a function of $\sigma_{Z'}$ and $M_{Z'}$ for the likelihood fit to ATLAS data in the dielectron (left) and dimuon channel (right).

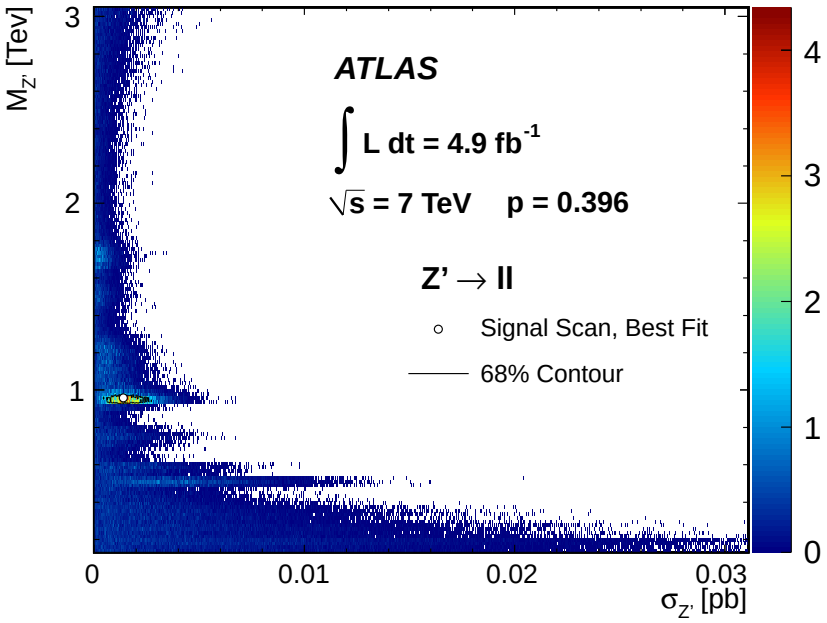

Figure 3.15: Absolute value of the log-likelihood-ratio test statistic as a function of $\sigma_{Z'}$ and $M_{Z'}$ for the likelihood fit to ATLAS data for the combination of the dielectron and dimuon channel.

For the dielectron sample we observe a p-value of 36% and for the dimuon sample, we observe a p-value of 68%. For the combination of both channels, we observe a p-value of 40%.

Bump hunting

We also test for presence of a resonance using the BumpHunter algorithm [77]. The BumpHunter algorithm scans the spectrum of interest (in this case the electron-electron and muon-muon invariant mass) in windows of progressively increasing width. In a given window the algorithm computes a negative logarithm of the Poisson probability for the background to fluctuate to or above the prediction. The largest value of the computation over all assumed search windows and all considered window widths is the final test statistic.

The reported p-value in the electron channel is 64% and in the muon channel 91%.

Local significances

Finally, we display the differences between data and expectation using the tool developed by G. Choudalakis and D. Casadei [78]. The result is shown in figure 3.16 for both electron and muon channels. The largest positive local significance is $< 2\sigma$ in the electron channel

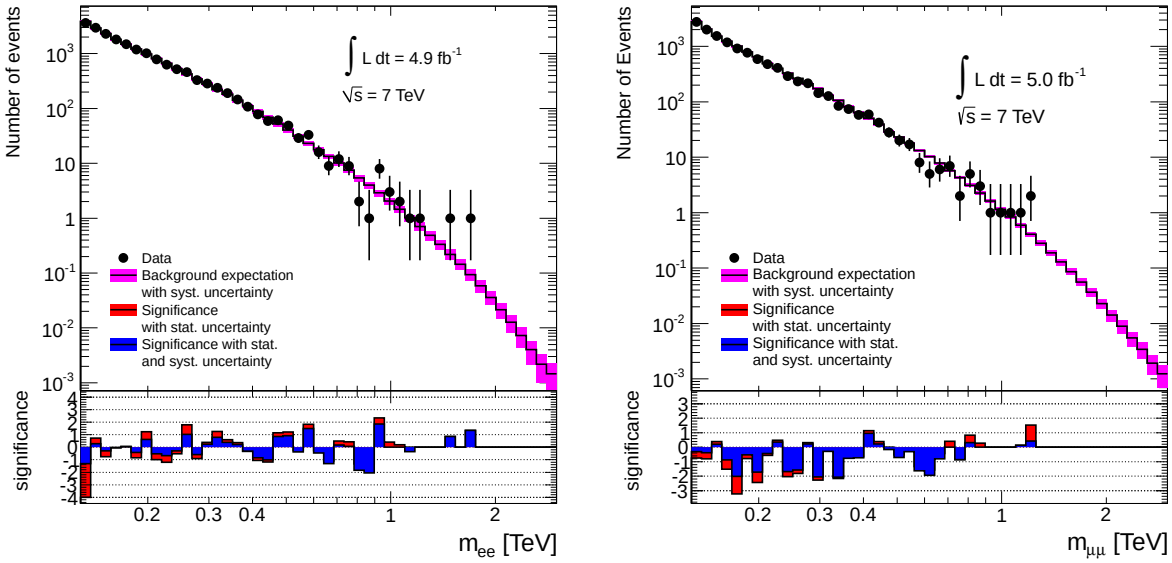

Figure 3.16: Differences between data and expectation in the electron (left) and muon (right) channels. The mass range goes from 128 GeV to 3 TeV

and $\sim 1\sigma$ in the muon channel, and the largest negative local significance is about -1.5σ and -2σ respectively).

In conclusion: the data are consistent with the Standard Model prediction in this search.

3.4.2 Cross section and mass limits

In the absence of a signal, an upper limit on the number of events N_X produced by the decay of a new resonance X ($X = Z'$ for example) is determined at the 95% confidence level (C.L.) using a Bayesian approach [75], in exactly the same manner as in the EPS2011 and Moriond2012 analyses.

The invariant mass distribution of the data is compared to templates of the expected backgrounds and varying amounts of signal at varying pole masses in the 0.13-3.0 TeV range[5]. The templates provide the expected yield of events (μ) in each $m_{\ell\ell}$ bin: $\mu = N_X(\lambda, \bar{\nu}) + N_{DY}(\bar{\nu}) + N_{obg}(\bar{\nu})$, where λ represents the model parameters, $\bar{\nu}$ the set of nuisance parameters and N_X, N_{DY}, N_{obg} are respectively the number of new resonance, Drell-Yan and other backgrounds events. The interference between signal and Drell-Yan is neglected. Some example signal templates are shown in appendix C.

A likelihood function is defined as the product of the Poisson probabilities over all mass bins in the search region, where the Poisson probability in each bin is evaluated for the observed number of data events given the expectation from the template. The total acceptance for signal as a function of mass is propagated into the expectation. For each X pole mass, a uniform prior in the X production cross section is used.

The limit on N_X is converted into a limit on cross section times branching ratio $\sigma B(X \to \ell^+\ell^-)$ by scaling with the observed number of Z boson events and the known value of $\sigma B(Z \to \ell^+\ell^-)$:

$$\sigma B(X) = \sigma B(Z) \frac{N_X \, \mathcal{A}\epsilon(Z)}{N_Z \, \mathcal{A}\epsilon(X)},$$

where

- $\sigma B(Z) = 0.989$ nb is the inclusive Z cross section for $m_{\ell\ell} > 60$ GeV [69];
- $\mathcal{A}\epsilon(Z)$, calculated with the inclusive Z MC sample, is the efficiency of requiring $70 < m_{\ell\ell} < 110$ GeV times the average selection efficiency for events with $m_{\ell\ell} > 60$ GeV:

  $$\mathcal{A}\epsilon(Z) = N^{MC}(\text{selected events},\ 70 < m_{\ell\ell} < 110\,\text{GeV})/N^{MC}(\text{all events},\ m_{\ell\ell} > 60\,\text{GeV});$$

- N_Z is the number of Z events in the $70 < m_{\ell\ell} < 110$ GeV range;
- $\mathcal{A}\epsilon(X)$ is the acceptance times efficiency for a given X pole mass.

$\mathcal{A}\epsilon(X)$ is obtained from a weighted average of $\mathcal{A}\epsilon$ versus $m_{\ell\ell}$ over the full line-shape between 0.13 and 3 TeV and is shown on figures 3.17. The luminosity normalization is replaced by

[5]The exact range actually starts at 128.05 GeV.

a normalization to the data, using the Z number of events and acceptance above 0.13 TeV in order to cancel systematic uncertainties.

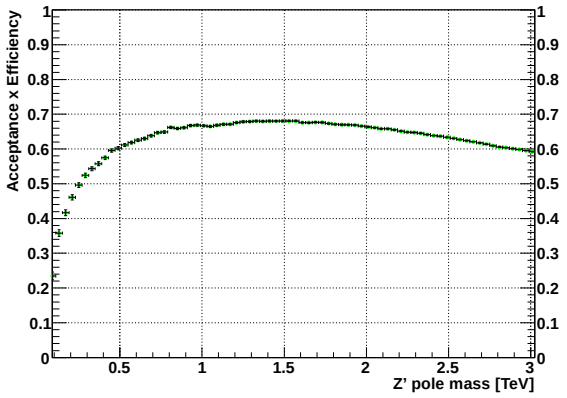

Figure 3.17: Electron channel: total acceptance times efficiency as a function of the pole mass for Z'

The expected exclusion limits are determined using simulated pseudoexperiments containing only Standard Model processes by evaluating the 95% C.L. upper limits for each pseudoexperiment for each fixed value of M_X. The median of the distribution of limits is chosen to represent the expected limit. The ensemble of limits is also used to find the 68% and 95% envelope of the expected limits as a function of M_X.

We perform combinations of the channels (dimuon and dielectron) by using a joint likelihood: the combination is performed by defining the likelihood function in terms of the total number of Z' events produced in the two channels. The details of the statistical treament are given in [79]. For two combined channels, nuisance parameters can be correlated for each process and channel.

Finally, lower limits on M_X are obtained by comparing the expected σB with the upper limits on σB as a function of M_X.

Limits on spin-1 Z'

Figure 3.18 (left) shows for the dielectron channel the 95% C.L. observed and expected exclusion limits on $\sigma B(Z' \rightarrow e^+e^-)$. It also shows the theoretical cross section times branching ratio for the Z'_{SSM} and for the lowest and highest σB of E_6-motivated Z' models. Similarly, Figure 3.18 (right) show the same results in the case of the dimuon selection. Figure 3.19 shows the 95% C.L. exclusion limit on σB for the combination of the electron

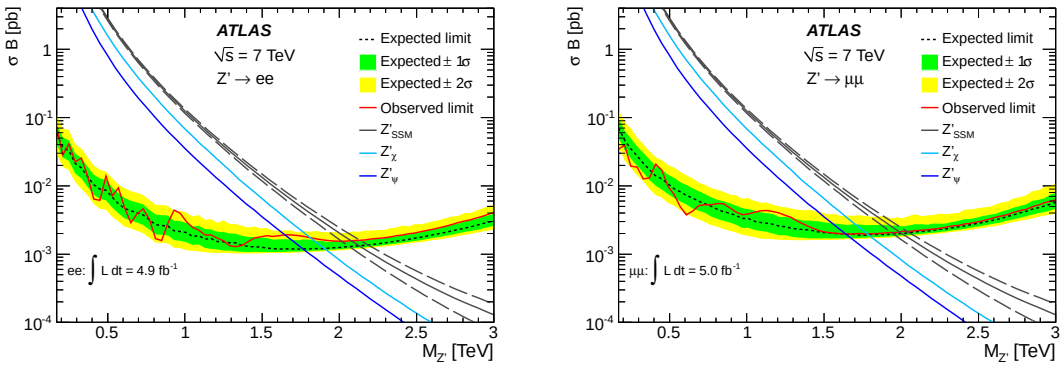

Figure 3.18: Expected and observed 95% C.L. limits on σB and expected σB for Z'_{SSM} production and the two E_6-motivated Z' models with lowest and highest σB for the di-electron (left), and the dimuon selection (right). The thickness of the SSM theory curve represents the theoretical uncertainty and holds for the other theory curves.

and muon channels, and Figure 3.20 shows the ratio of this limit divided by the Z'_{SSM} cross section.

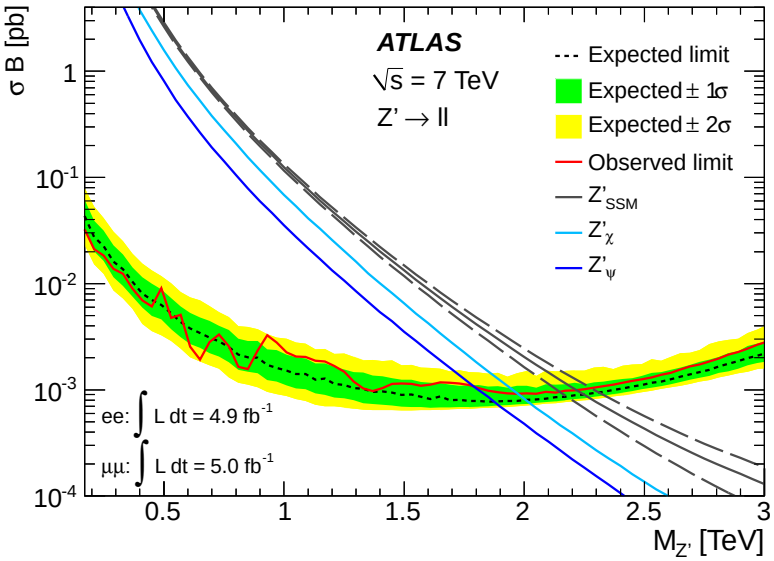

Figure 3.19: Expected and observed 95% C.L. limits on σB and expected σB for Z'_{SSM} production and the two E_6-motivated Z' models with lowest and highest σB for the combination of the electron and muon channels. The thickness of the Z'_{SSM} theory curve represents the theoretical uncertainty and holds for the other theory curves.

The 95% C.L. σB limit is used to set mass limits for each of the considered models. Mass limits obtained for the Z'_{SSM} are displayed in Table 3.14. The combined mass limit

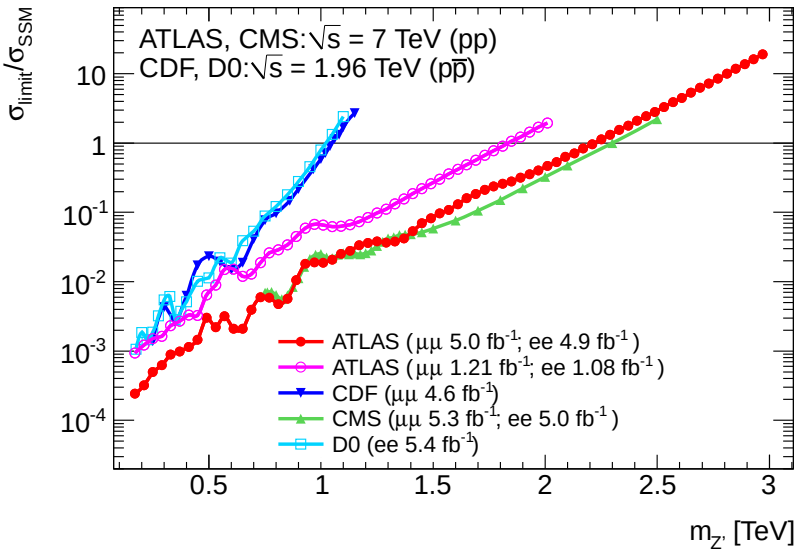

Figure 3.20: Ratio of observed combined limit for the Z' search divided by the Z' cross section, using the combination of both channels.

for the Z'_{SSM} is 2.22 TeV (observed) and 2.25 TeV (expected). The combined mass limits on the E_6-motivated models are given in Table 3.15.

Table 3.14: e^+e^-, $\mu^+\mu^-$ and combined 95% C.L. mass limits on Z'_{SSM}

	Observed limit mass [TeV]	Expected limit mass [TeV]
$Z'_{\mathrm{SSM}} \to e^+e^-$	2.08	2.13
$Z'_{\mathrm{SSM}} \to \mu^+\mu^-$	1.99	2.00
$Z'_{\mathrm{SSM}} \to \ell^+\ell^-$	2.22	2.25

Table 3.15: Combined mass limits at 95% C.L. on the E_6-motivated Z' models

Model	Z'_ψ	Z'_{N}	Z'_η	Z'_{I}	Z'_{S}	Z'_χ
Observed Mass limit [TeV]	1.79	1.79	1.87	1.86	1.91	1.97
Expected Mass limit [TeV]	1.87	1.87	1.92	1.91	1.95	2.00

3.4.3 Coupling limits

Limits on spin-1 Kaluza-Klein γ/Z

Because of the strong interference with the DY, it is not possible to set limits on σB in the Kaluza-Klein model. Moreover, the $m_{\ell\ell}$ shape with the interference can become the discriminant feature. This is done by introducing a coupling scale that multiplies the fermion couplings, $g^X_{\lambda_f}$, where λ_f can be e.g. the helicity coupling, $\lambda_f = L, R$, like it is done in [8]. As shown in appendix B, the pure signal (resonance X) term is proportional to g^4 and the interference term is proportional to g^2:

$$\begin{aligned} \frac{d\sigma_{\text{off-shell}}}{ds_{\ell\ell}} &= |\text{DY}|^2 + 2\text{Re}\left[\text{DY}^* X\right] + |X|^2 \\ &\sim |\text{DY}|^2 + \quad g^2\frac{A}{c_1^2} \quad + g^4\frac{B}{c_1^2} \end{aligned} \tag{3.2}$$

where A, B and c_1^2 are functions of the couplings masses, widths and $s_{\ell\ell}$, but not of the scale g. Depending on the values of g and $M(X)$, either term (resonance or interference), or both, could play the most significant role. Therefore we compute the limits with g^4 as the prior parameter rather than σB, and we also compute them with g^2 in order to cover all possible configurations.

Two-dimensional templates are produced for pole masses, m_X, between 130 GeV and 5130 GeV. For each template, 47 slices in $m_{\ell\ell}$ (log bins between ∼128 GeV and 3 TeV) are given to BAT [75] as functions of g^4 and the limit is put on this parameter, versus the pole mass. Example templates are shown in appendix C.

For the limit-setting, the range in which g^4 is allowed to vary is 0 to 100 (see also appendix D). The resulting limits on g are shown in figures 3.21 and 3.22 for $Z_{\text{KK}}/\gamma_{\text{KK}}$ respectively with g^4 and g^2 as prior. Figure 3.23 shows the electron plus muon $Z_{\text{KK}}/\gamma_{\text{KK}}$ combined limits with the two prior choices. The special treatment of the systematic uncertainties with respect to the Z'model is detailed in appendix D.

Finally, lower limits on M_{KK} are derived from the $Z_{\text{KK}}/\gamma_{\text{KK}}$ hypothesis ($g = 1$); they are displayed in table 3.16. Contrary to the non-interfering case, high-mass candidates in data induce observed limits which are better than expected. The obtained mass limits are higher than the indirect limits from electroweak precision measurements [6, 80].

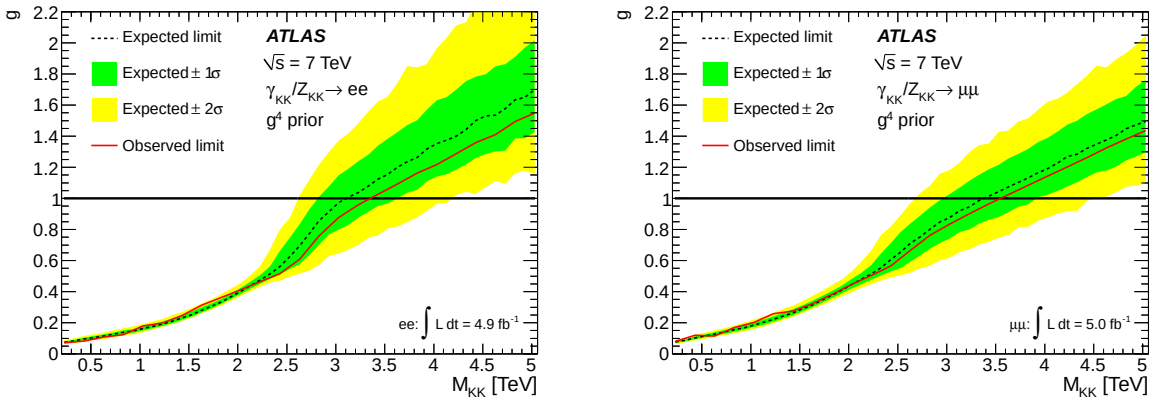

Figure 3.21: Dielectron (left) and dimuon (right) limits on g in the $Z_{\mathrm{KK}}/\gamma_{\mathrm{KK}}$ hypothesis with g^4 as prior

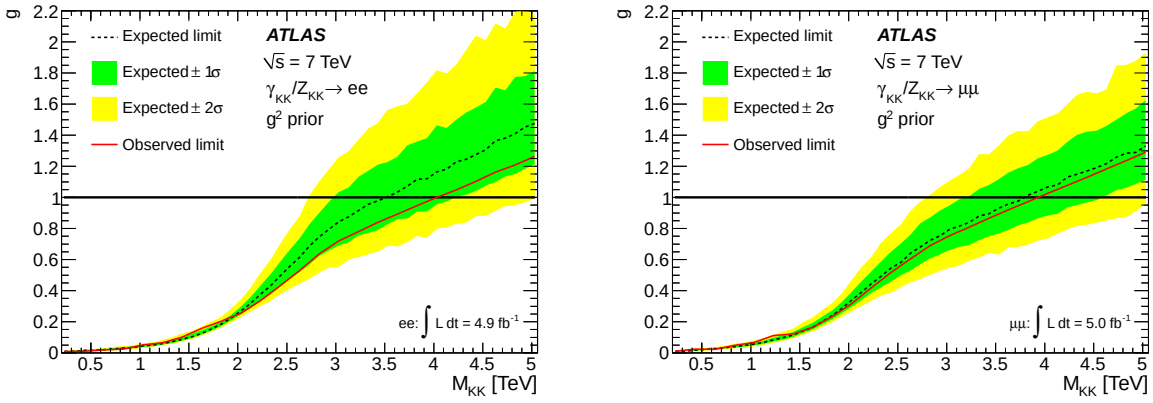

Figure 3.22: Dielectron (left) and dimuon (right) limits on g in the $Z_{\mathrm{KK}}/\gamma_{\mathrm{KK}}$ hypothesis with g^2 as prior

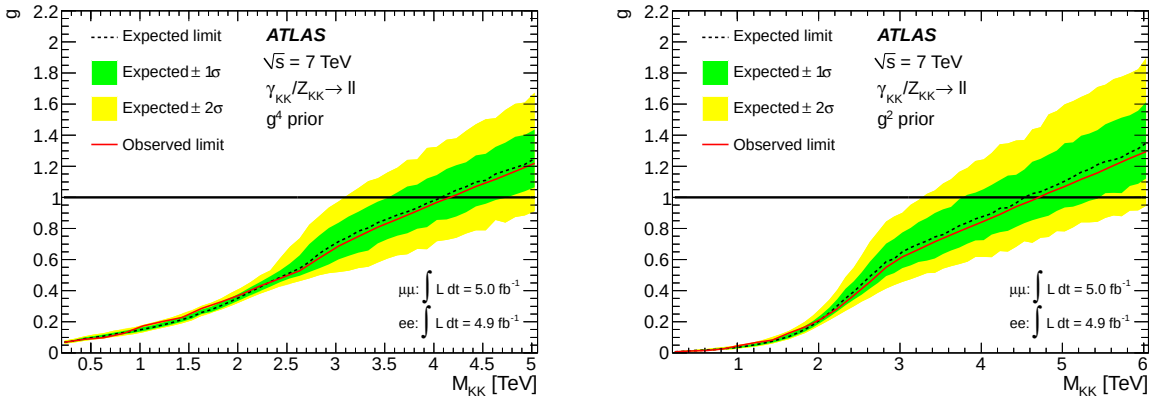

Figure 3.23: e^+e^- and $\mu^+\mu^-$ combined 95% C.L. mass limits on $Z_{\mathrm{KK}}/\gamma_{\mathrm{KK}}$ with g^4 (left) and g^2 (right) as prior

Table 3.16: e^+e^-, $\mu^+\mu^-$ and combined 95% C.L. mass limits on $Z_{\rm KK}/\gamma_{\rm KK}$.

	g^4 prior		g^2 prior	
	Observed [TeV]	Expected [TeV]	Observed [TeV]	Expected [TeV]
$Z_{\rm KK}/\gamma_{\rm KK} \to e^+e^-$	3.35	3.11	4.03	3.52
$Z_{\rm KK}/\gamma_{\rm KK} \to \mu^+\mu^-$	3.55	3.38	3.93	3.79
$Z_{\rm KK}/\gamma_{\rm KK} \to \ell^+\ell^-$	4.16	4.07	4.71	4.53

Comparison of limits obtained within different frameworks

In the $Z_{\rm KK}/\gamma_{\rm KK}$ model parametrization described above, $g4 = g = 0$ simply returns the DY shape, whereas $g4 = g = 1$ gives the KK scenario. It is also possible to get limits on the $Z'_{\rm SSM}$ within the $Z_{\rm KK}/\gamma_{\rm KK}$ framework by removing the factor of $\sqrt{2}$ from the fermion couplings, stopping the KK tower at $n = 1$ and removing the KK photon from the amplitude (the conventional KK model features are described in [8]). The expected limits on g are shown in figures 3.24 and the mass limits in table 3.17. The expected mass limits are lower than the ones obtained in the baseline analysis by 120 GeV ($\mu^+\mu^-$) and 130 GeV (e^+e^-) respectively. As a consistency check, the limits were computed again in the same framework but neglecting the interference, and by fixing the width of the resonance. It was found that the interference had a small effect (at most 10-20 GeV) compared to the width variation, and that fixing the width to the SSM value allowed to recover the baseline σB limits on $Z'_{\rm SSM}$ within 20 GeV.

The minimal Z' framework also includes a model in which the baseline σB analysis is interpreted: the Z'_χ. It gives limits which are lower by 80 GeV in both channels (see table 3.17). The same cross-checks, fixing the width and/or removing the interference, were made and lead to the same conclusion: the interference effect is very small and the difference is mainly due to the width variation.

In both cases, the worsening of the limit with the varying-width method is to be expected, since for increasing coupling, the correspondingly increasing cross section is not as strongly excluded in the case that the resonance width increases with couplings.

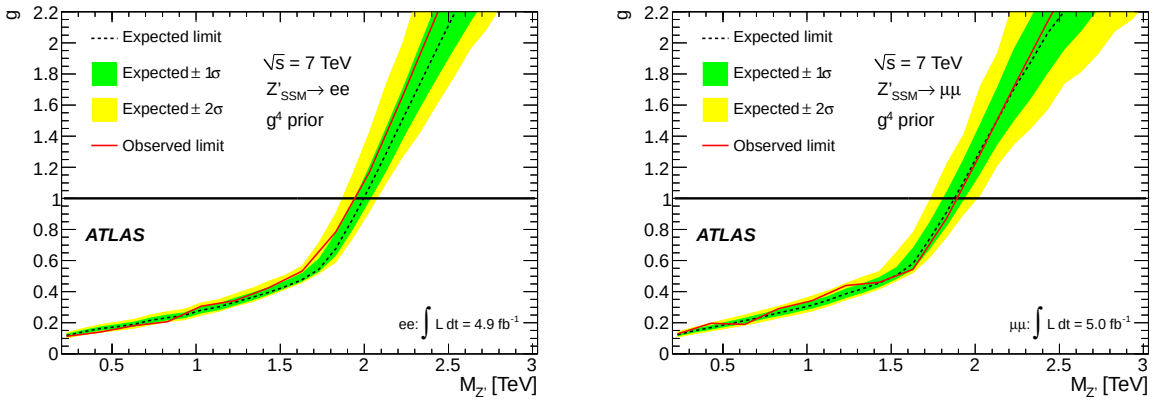

Figure 3.24: Dielectron (left) and dimuon (right) limits on g in the Z'_{SSM} hypothesis (g^4 prior)

To conclude, we have checked that the limits obtained in the different frameworks are consistent within ~ 20 GeV once the resonance width is fixed to the SSM value.

Table 3.17: Comparison of observed (expected) limits in the baseline Z' σB analysis and in the coupling limit frameworks with and without allowing the width to vary with g.

	e^+e^-	$\mu^+\mu^-$
Method	[TeV]	[TeV]
σB limit	2.08(2.13)	1.99(2.00)
Coupling limit, fixed width	2.09(2.14)	1.99(2.00)
Coupling limit, varying width	1.94(2.00)	1.89(1.88)

Chapter 4

2012 dilepton analysis

The search described on chapter 3 based on the LHC 7 TeV data was repeated using the 8 TeV data collected in the following year. In particular, this chapter describes the search for heavy neutral gauge boson (namely Z'_{SSM}) within the ATLAS experiment. It includes the results from an analyses of pp collisions decaying into l^+l^- pairs at a center-of-mass energy of 8 TeV collected during 2012. It will focus on the analysis of the electron channel but for completeness I will present the results from the muon channel, as well as, the combined results (where applicable).

4.1 Samples and Cross sections

4.1.1 Data samples

The data sample used for this analysis was collected in 2012, and corresponds to an integrated luminosity of 5.9 (e^+e^-) / 6.1 ($\mu^+\mu^-$) fb^{-1} . The data used in the analysis span all periods from A through B14 of the 2012 data-taking.

The data used for this study are required to have been recorded during periods of stable LHC beams, and when all relevant systems of the detector were operating normally i.e. requiring good calorimetry, full inner detector tracking, as well as full solenoidal magnetic field and good EGamma trigger. The equal treatment of the real and simulated data is possible thanks to the simulation closely following the detector conditions.

4.1.2 Monte Carlo samples

All samples are generated and fully simulated (using GEANT) in the ATHENA MC12 framework.

Simulated signal processes

The fully simulated signal "templates" used in the σB limit setting procedure (see section 4.4) are derived by a reweighting procedure according to the desired invariant mass line shape. The reweighting procedure,, assumes a LO Drell-Yan sample and is based on PYTHIA8 [7] generated with LO MSTW2008LO PDF [1]. To ensure adequate statistics at high invariant mass the samples are generated in 15 bins of true dilepton invariant mass between 75 GeV and 3000 GeV. The signal templates used for this study are produced by reweighting the LO DY samples with the analytical 2-dimensional weighting function,

$$\mathcal{W}\left(m_{\ell\ell}, q\right) = \frac{\left|Z'_{SSM}\right|^2}{\left|\mathrm{DY}\right|^2} \tag{4.1}$$

where DY and Z'_{SSM} are the helicity amplitudes. Both the DY and the Z'_{SSM} parts are functions of the truth dilepton invariant mass, $m_{\ell\ell}$ and the incoming quark flavor, q which determines the production couplings.

The weight can be evaluated precisely for any Z'_{SSM} mass where this was validated against the official Z'_{SSM} signal samples (see figure 4.1).

The official Z'_{SSM} samples include the DY by interference so in order to validate the templates agianst these, one needs to add the DY in the Z'_{SSM} amplitude itself. Therefore, equation 1 becomes:

$$\mathcal{W}\left(m_{\ell\ell}, q\right) = \frac{\left|\mathrm{DY} + Z'_{SSM}\right|^2}{\left|\mathrm{DY}\right|^2} \tag{4.2}$$

The small discrepancies around the maximum interference are due to the fact that the weight function do not include the angular information ($\cos\theta^*$) but since the interference with the DY is not taken into account in this analysis then this is negligible.

[1] In the earlier analyses, a 'flat' sample was used for the Sequential Standard Model (SSM) $Z'(Z'_{\mathrm{SSM}})$, obtained using a modified version of PYTHIA .

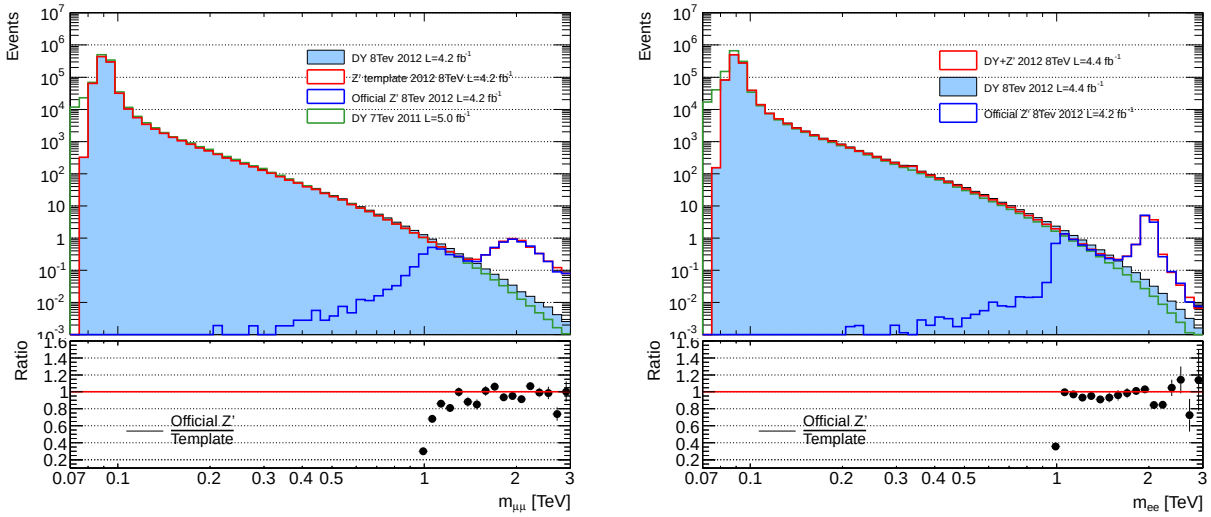

Figure 4.1: Dimuon (left) and dielectron(right) invariant mass distributions after event selection, of Z'_{SSM} signals at pole mass 2 TeV. The bottom plots shows the ratio of the official Z'_{SSM} sample (blue histogram) over the signal template (red histogram). The light blue fill is the DY background and is shown for comparison

Simulated background processes

The DY background is simulated with Powheg (NLO) + Pythia8 and the CT10 [65] PDF, covering masses above 60 GeV binned in dilepton truth invariant mass to ensure good statistics in the high mass tail.

The $W \to l\nu$ process was simulated separately for W^+ and W^-. Also here Powheg with the CT10 PDF was used. In addition, diboson samples (WW, WZ, ZZ) with the same generator and PDF were produced.

The $t\bar{t}$ background is generated with MC@NLO to generate matrix elements, Jimmy to describe multiple parton interactions and Herwig to describe the remaining underlying event and parton showers. Also the CT10 [65] parton distribution functions are used.

4.1.3 Cross sections

Signal and Drell Yan cross sections

The signal and SM background processes are typically generated using leading-order (LO) or next-to-leading-order (NLO) matrix elements and the corresponding parton distribution functions (PDFs). The normalization and the shape of these differential cross sections are modified by higher-order QCD and electroweak corrections. However, next-to-next-to-

leading order (NNLO) generators are typically not available for all the processes of interest. We follow the usual procedure of using NNLO QCD calculations of the DY process to compute a mass-dependent K-factor. We define this K-factor as a function of invariant mass which, when used to multiply the LO or NLO differential cross section, yields the NNLO differential cross section as a function of mass. It is conventional to assume that all colorless final states have similar QCD radiation in the initial state, and therefore the K-factor derived for the LO Drell Yan process can be applied to our signal processes as well.

The Z/γ^* cross section is calculated at next-to-next-to-leading order (NNLO) using PHOZPR [81] with the MSTW2008 NNLO PDF. The ratio of this cross section to the leading order cross section (or next-to-leading order in the case of Powheg) is used to determine a mass dependent QCD K-factor (K_{NNLO}). For the signal simulation, a DY sample has been generated using PYTHIA and the MSTW2008 LO PDF and is used to reweight to our target signal samples. Therefore we use the K_{NNLO} to weight our simulated signal events as a function of the dilepton invariant mass. Some representative values of K_{NNLO} are shown in Table 4.1. Similarly, we use appropriate K_{NNLO} factors to weight the

Table 4.1: QCD K-factor for several Z' mass points obtained with PYTHIA (LO) and PHOZPR (NNLO) using the central value of MSTW2008 NNLO PDF.

Z' mass [GeV]	250	500	700	1000	1250	1500	1750	2000	2250	2500
$K_{\mathrm{NNLO}}=\frac{\sigma_{\mathrm{NNLO}}}{\sigma_{\mathrm{LO}}}$	1.333	1.351	1.343	1.323	1.307	1.294	1.294	1.283	1.284	1.289

NLO Powheg DY sample to model the DY background. Furthermore, a mass-dependent electroweak correction is defined to take into account the effects of higher order electroweak corrections. The PYTHIA simulated samples already include real photon emission (FSR) via the PHOTOS program. We use the HORACE [66,67] program to calculate the weak K-factor due to the missing contributions from ISR, ISR/FSR interference and virtual gauge boson loops. Some representative values for the EW K-factor are shown in Table 4.2. A study that compares the Powheg and Pythia DY $m_{\ell\ell}$shapes after all corrections is summarized in appendix F. In particular, a correction to the Powheg MC is applied accounting for the fact that α_{em} is fixed to the value at the mass of the Z boson. The weak K-factor is not

applied to the signal cross section, since this K-factor depends on the W and Z boson couplings to the new Z'boson and is therefore model-dependent.

Table 4.2: Electroweak K-factor for both lepton flavour and for several masses obtained with HORACE using MRST2004QED PDF set.

Mass [GeV]	500	750	1000	1250	1500	1750	2000	2250	2500
K^{**}_{EW} (ee)	1.035	1.019	1.004	0.988	0.972	0.956	0.920	0.881	0.832
K^{**}_{EW} $(\mu\mu)$	1.030	1.014	0.999	0.984	0.969	0.953	0.931	0.898	0.859

The uncertainties on the QCD and EW K-factors are 3% and 4.5% respectively for a 2 TeV Z'. The uncertainty of the QCD K-factor includes variations of the renormalization and factorization scales by factors of two around the nominal scales and the difference in obtained K-factors when computing them for Z/γ^* vs for Z alone.

Other background cross sections

Cross section calculations for W and diboson production are described in references [68] and [69]. They are performed at NLO and normalized to NNLO in the case of W production, which amount to 7073.8 pb and 5016.2 pb for the W^+ and W^-, respectively. The theoretical uncertainties are 5% for inclusive diboson production and about 27.6 % for $W + n$ jets ($n > 0$) production. Cross section calculations for $t\bar{t}$ are performed at approximate-NNLO (238.06 pb) as described in reference [68]. The related uncertainty is 8.3%.

4.2 Electron Channel

This section describes the dielectron part of the analysis: selection, efficiencies, electron energy corrections, background estimation and data/Monte Carlo comparison.

4.2.1 Electron identification and event selection

The selection criteria used in the present analysis are listed below. As compared to the analysis of the 2011 data, the main change is the trigger used, which in turn requires

different and larger minimum requirements on the p_{T} of the leading and subleading electron. Also the electron ID requirement is more strict compared the one from the previous analysis.

- Event was taken during stable operation of the LHC beam, and when all relevant systems of the detector were operating normally;
- Event has at least one primary vertex, with more than 2 tracks;
- Event passes the trigger EF_g35_loose_g25_loose (demand one photon with $P_T > 35$ GeV and a second one with $P_T > 25$ GeV);
- Event fulfills LArError < 2, which is a variable providing protection against noise bursts and data corruption;
- Each electron must have $|\eta| < 2.47$ excluding the crack region $1.37 < |\eta| < 1.52$;
- Each cluster must pass calorimeter quality requirements;
- The leading electron must have $p_{\mathrm{T}} > 40$ GeV, the subleading electron must have $p_{\mathrm{T}} > 30$ GeV;
- Each electron must have at least isEM medium++ identification[2]
- The leading electron must be isolated ($\texttt{Iso}_{\mathrm{corr}} < 7$ GeV);
- The invariant mass of the pair is required to be above 80 GeV.

Note that no requirement is made regarding the charge balance of the two electrons in order to avoid effects due to possible charge miss identification, which are difficult to quantify at large transverse momenta of the electrons.

4.2.2 Corrections applied to MC and data

The only correction applied to data is for the energy scale. The data energies are corrected by values provided by the EGamma group, which were obtained using the Z peak for calibration [72].

Using the same tool, the simulation is adjusted by smearing the values in the MC in order to reproduce the energy resolution observed in data [72].

Measurements of the electron reconstruction and identification efficiency in data show small differences in the η and E_T distributions. To account for this, a weight is applied to

[2]It should be noted that the requirement for each electron to have a B-layer hit if one is expected, which was part of the 2011 data analysis, is now not anymore explicitely required as it is now part of the medium++ ID requirement.

each Monte Carlo event which is the product of η and E_T dependent scaling factors. These scale factors are provided by the EGamma group [71] for the standard part of the electron selection (electron reconstruction and *medium* level of identification). No scale factor is applied for the isolation of the leading electron. Preliminary studies found that data and MC agree within 2%. In addition, no scale factors have been applied for the trigger. Here preliminary studies show that the efficiencies in data and MC agree to better than 1% everywhere.

4.2.3 Signal efficiencies

The overall acceptance times efficiency ($\mathcal{A}\epsilon$) of the final selection for the $Z'_{\mathrm{SSM}}$is displayed in Figure 4.2 as a function of the dielectron mass.

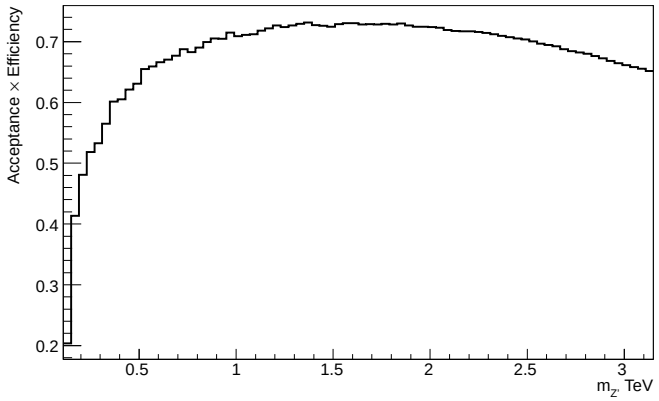

Figure 4.2: Electron channel: total acceptance times efficiency as a function of Z' pole mass.

4.2.4 Background Estimation

The method of choice to determine the background is the reverse-ID method. The final analysis of the 2011 data employs four different methods to determine the background, the reverse-ID being one of them. It was choosen as it is the most simple and thus only possible method that can be carried out in a short time. Also for the preliminary 2011 result for Moriond the only method used was the reverse-ID.

In the reverse-ID method, all backgrounds are modeled using Monte Carlo simulation except the QCD background, which is measured from data.

It uses a template fit in m_{ee}, performed in the range 80-200 GeV, to determine the amount of QCD multijet background. The fit uses two templates that are allowed to float: The first one contains the Monte Carlo (Drell Yan plus W plus $t\bar{t}$ plus diboson) after full event selection (all normalized relatively to each other according to their cross sections). The other one, the "QCD template", is built from real data by reversing identification cuts, leading to a QCD enriched sample. However, as also real electrons from Drell Yan, W + jets , $t\bar{t}$ or dibosons could dilute the QCD template, the reverse ID cuts are also aplied to those and this dilution to the QCD enriched data sample is subtracted according to Luminosity.

The reverse identification requires that the electrons satisfy the cutflow given above up to the electron pT requirement. In addition, both electrons need to satisfy all cuts of the loose++ requirement except the one that puts requirements on the matching between the track and the cluster in eta. In terms of identification this offline selection is close to what the diphoton trigger already selects. Next, in order to be selected for the QCD template, both electrons are required to fail the track–cluster matching criteria that is part of the the medium++ ID.

The fit of the two templates to data determines the factor by which the QCD templates needs to be scaled. The resulting factor for the sum of the MCs is 1.004 and thus within the luminosity uncertainty. The result of the fit after scaling is shown in Fig. 4.3. The QCD template is shown in dark blue, the sum of the other MCs is shown here already separately for the different contributions. The large first bin from 80-110 GeV is needed in order to not be sensitive to the exact shape of the Z-peak.

The extrapolation to high invariant mass, i.e., above 500 GeV for the QCD bg, is done by fitting the QCD template. A number of fits is carried out exploring various fit ranges as well as two fit functions. The lower edge of the fit is varied between 130 and 150 GeV, with a step size of 10 GeV, the upper edge is varied from 600 GeV to 725 GeV with a step size of 25 GeV. The fit results satisfying certain requirements on the chi2 as well as the fit probability are further used to caluclate the mean and RMS. Above 500 GeV ("the stitiching point") the mean is used as QCD background. The RMS is used as fit uncertainty.

Very few events of the W MC survive the cut flow. In order to get an estimate at high invariant masses the selection criteria is modified to not require any electron ID. The

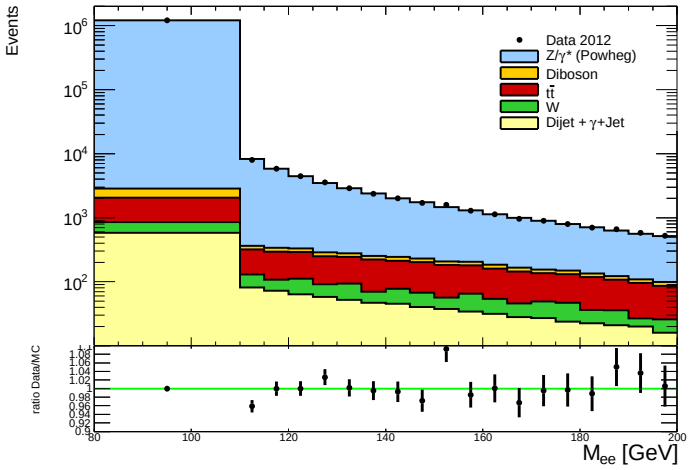

Figure 4.3: Dielectron invariant mass distributions in the binning used by the two-component fit. The separate contributions are already scaled by the output of the fit and compared to data.

resulting distribution is again fitted in order to extrapolate to high mass. The lower edge of the fit is varied between 130 and 150 GeV, with a step size of 10 GeV, the upper edge is varied from 600 GeV to 1000 GeV with a step size of 50 GeV. As described above for the case of QCD background, mean and RMS of the fit results is calculated and used above 400 GeV. As no identification criteria was used the fit is normalized to the actual full selection in the region between 130 and 200 GeV.

The $t\bar{t}$ and diboson backgrounds need to be extrapolated to high mass as well. For the $t\bar{t}$ background, the lower edge of the fit is varied between 130 and 170 GeV, with a step size of 10 GeV, the upper edge is varied from 700 GeV to 1000 GeV with a step size of 50 GeV. The mean and RMS of the fit results is used above 500 GeV. For the diboson background, the lower edge of the fit is varied between 150 and 200 GeV, with a step size of 12.5 GeV, the upper edge is varied from 700 GeV to 1200 GeV with a step size of 50 GeV. The mean and RMS of the fit results is used above 700 GeV.

4.2.5 Data - Monte Carlo Comparison

The invariant mass of the electron pair (m_{ee}) distribution for selected events is shown in Fig. 4.4 for the data and the expected SM background. The DY MC used is Powheg. Fig. 4.5 shows the same distributions including a data/MC ratio, and Table 4.3 lists the correponding numbers.

Table 4.3: Expected and observed number of events in the dielectron channel. The errors quoted include both statistical and systematic uncertainties.

m_{ee} [GeV]	80 - 110	110 - 200	200 - 400	400 - 800	800 - 1200	1200 - 3000
Z / γ	1210000 ± 50000	36200 ± 1500	4330 ± 180	412 ± 20	21.6 ± 1.5	3.03 ± 0.35
tt	1200 ± 130	2190 ± 250	750 ± 130	53 ± 19	0.86 ± 0.18	0.041 ± 0.017
W + jets	250 ± 70	470 ± 130	130 ± 40	10.6 ± 3.0	0.30 ± 0.09	0.026 ± 0.009
Diboson	780 ± 40	482 ± 34	172 ± 22	21 ± 8	0.91 ± 0.05	0.117 ± 0.014
Dijet, γ-jet	580 ± 170	720 ± 240	250 ± 120	34 ± 23	2.1 ± 2.0	0.4 ± 0.5
Total	1220000 ± 50000	40100 ± 1600	5620 ± 260	530 ± 40	25.8 ± 2.5	3.6 ± 0.6
Data	1217760	39875	5760	615	31	5

Figure 4.6 shows the E_{T} distributions of the leading (highest E_{T}) and sub-leading (second highest E_{T}) electron after full event selection. Figure 4.7 shows the η and ϕ distributions of the two electrons respectively. Figure 4.8 shows the p_{T} and rapidity distributions of the electron pair.

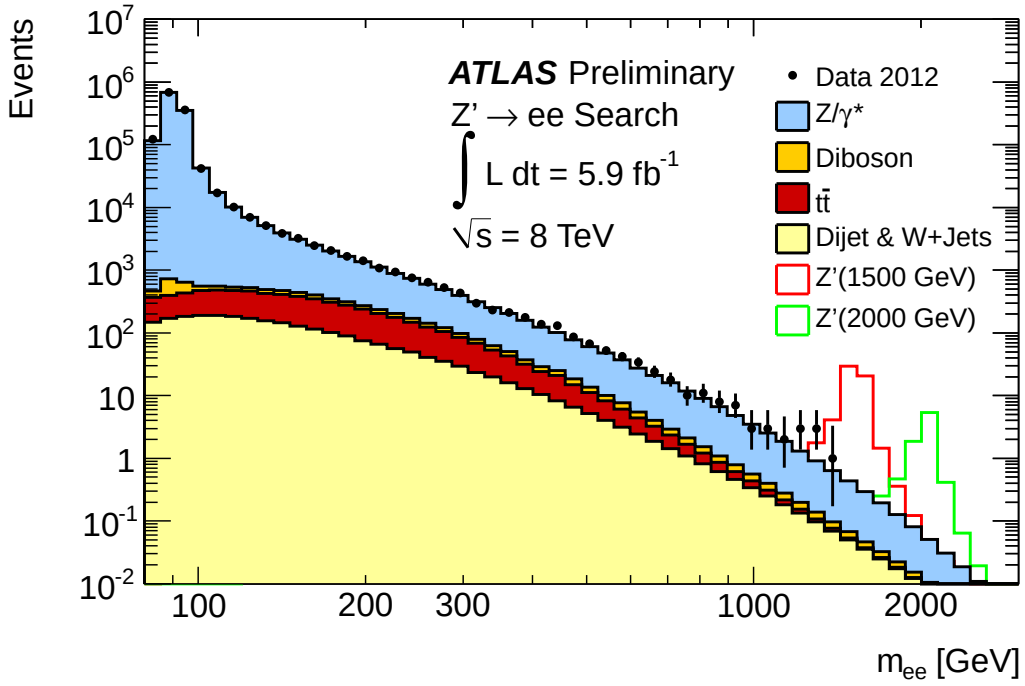

Figure 4.4: Dielectron invariant mass (m_{ee}) distribution after event selection. Here fits have been used for the extrapolation.

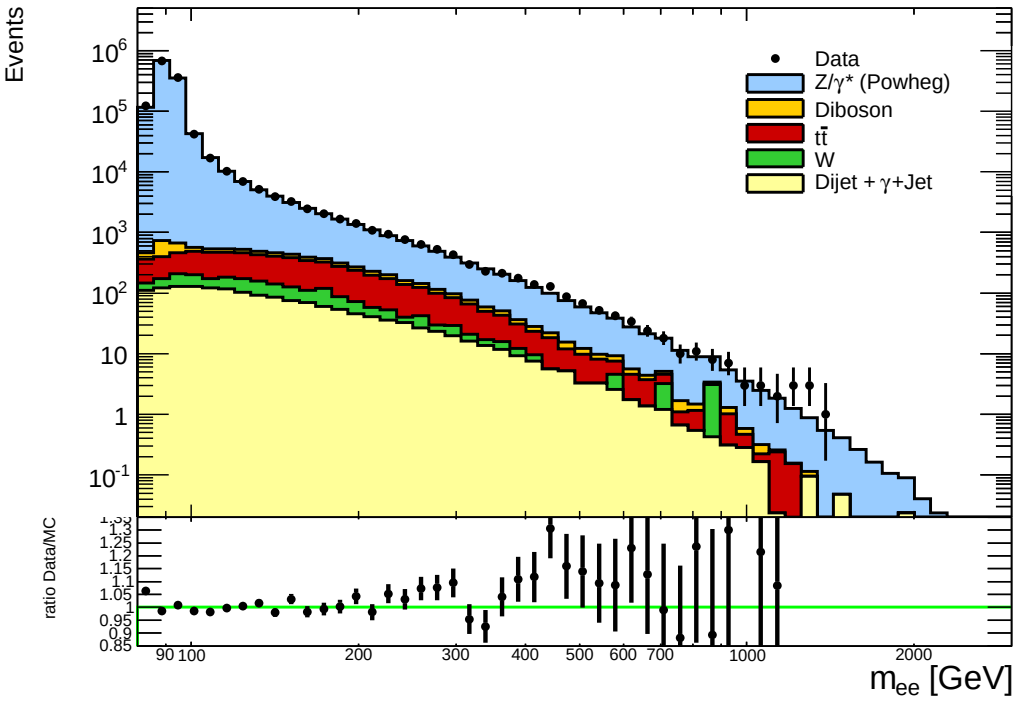

Figure 4.5: Dielectron invariant mass (m_{ee}) distribution after event selection. The distributions are not yet extrapolated to high masses by the use of fits.

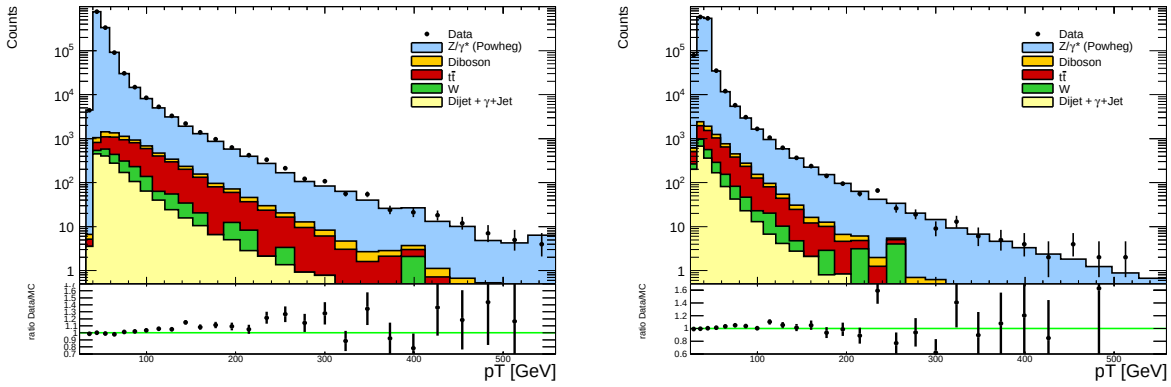

Figure 4.6: E_{T} distribution for the leading (left) and sub-leading (right) electron after event selection

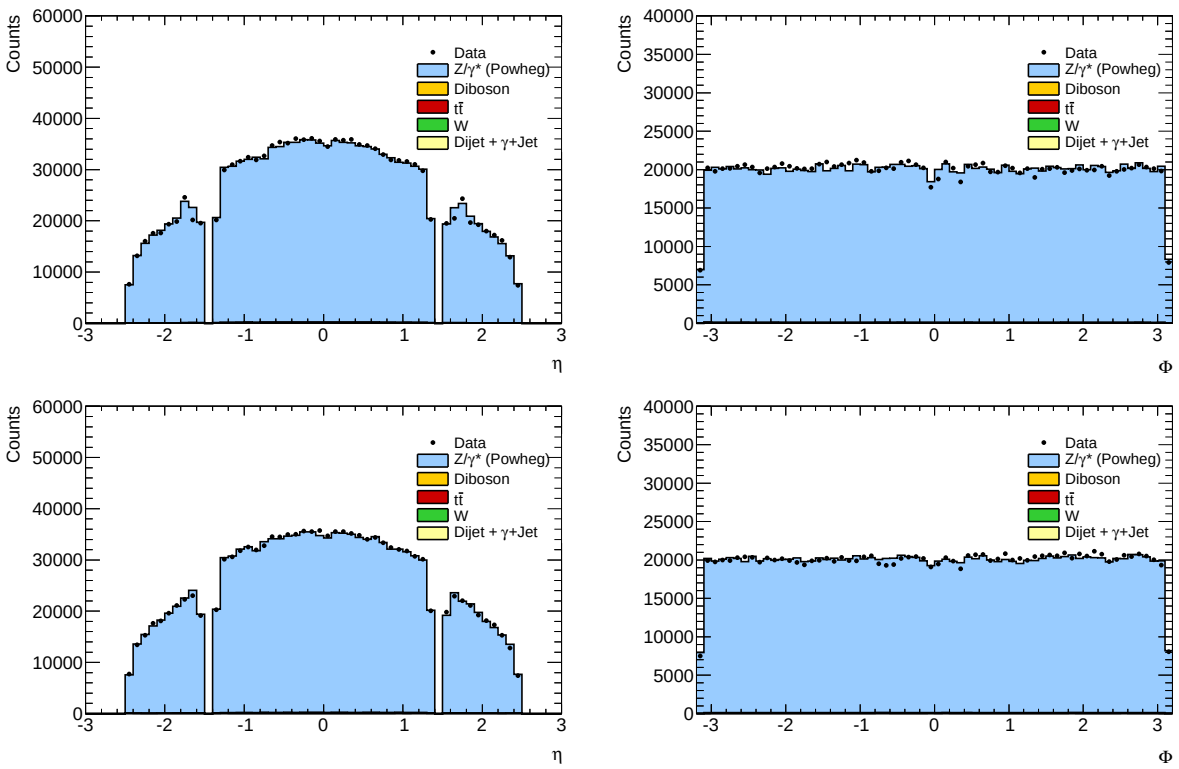

Figure 4.7: η and ϕ distributions for the leading (upper panels) and subleadig (lower panels) electron after event selection

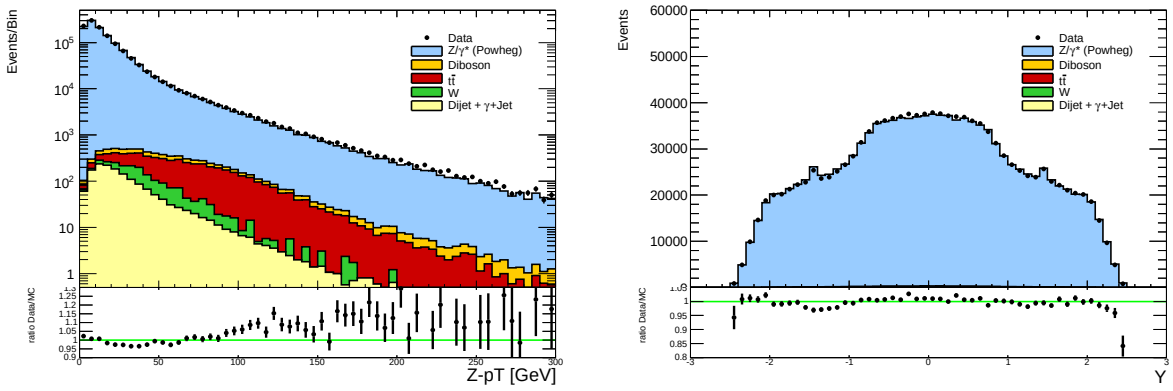

Figure 4.8: Dielectron p_T and rapidity after event selection

4.3 Systematic uncertainties

The systematic uncertainties in this analysis are reduced by the fact that the backgrounds are normalized to the data in the region of the Z peak. This procedure makes the analysis insensitive to the uncertainty on the integrated luminosity as well as other mass-independent systematic uncertainties. In the signal search and limit setting, mass-dependent systematic uncertainties are incorporated as nuisance parameters whose variation is integrated over in the computation of the likelihood function [75]; most are small at low mass and grow at high mass.

The main systematic uncertainties of this analysis are listed in tables 4.4 and 4.5. They include theoretical effects due to the PDF, QCD and electroweak corrections, as well as experimental effects, namely efficiency and resolution. These uncertainties are correlated across all bins in the search region. In addition, there is an uncertainty on the QCD component of the background affecting the electron channel. We assume that the experimental uncertainties are correlated between signal and all types of backgrounds. A flat uncertainty of 5%, due to the uncertainty on the Z/γ^* cross section in the normalization region, is assigned to the signal expectation. According to group recommendations, no theoretical uncertainties are applied on the signal expectation when setting limits.

A more detailed description of the uncertainties is listed below. The uncertainty on the PDF is 7% at 1 TeV and 20% at 2 TeV for both channels and follows the evaluation of the 2011 analysis (See the previous chapter). It is obtained by variations of the parameter set of the MSTW2008, NNPDF2.1, CT10, and CT10W PDFs and evaluating the envelope of the uncertainty bands. The PDF uncertainty also contains uncertainties due to α_S variations, as well as uncertainties on the QCD corrections: variations of the renormalization and factorization scales by factors of two around the nominal scales, which are added linearly. Furthermore the largest difference in obtained K-factors for Z and Z/γ^* production is added. Using the difference in NNLO and NLO cross sections, we obtain a comparable estimate. The uncertainty of the electroweak corrections is 4.5% at 2 TeV for both channels, and includes the effects of neglecting real boson emission, the difference in the electroweak scheme definition between Pythia and Horace, and higher order electroweak and $\mathcal{O}(\alpha\alpha_s)$ corrections.

On the experimental side, the systematic effects are as follows. In the electron channel, we assign a systematic uncertainty for the electron reconstruction and identification

efficiency at high p_{T} of 2% at 2 TeV. This uncertainty is estimated by studying the mass dependence of adding the calorimeter isolation cut and affects both signal and background expectations. The calorimeter resolution is dominated at large transverse energy by a constant term which is 1.0% (1.2% in the latest public reference [82]) in the barrel and 1.6% (1.8% in the latest public reference) in the end-caps with a small uncertainty [72]. The simulation was adjusted to reproduce this resolution at high energy and the uncertainty on it has a negligible effect, however it is included in the likelihood and affects the signal only. The calorimeter energy calibration uncertainty is between 0.5% and 1.5% depending on transverse momentum and pseudorapidity. The non-linearity of the calorimeter response is negligible according to test beam data and Monte Carlo studies [76]. The uncertainty on the energy calibration has minimal impact on the sensitivity of the search, since its main effect is a shift of a potential peak in dilepton mass without change of the line-shape. Finally, the QCD multijet background in the electron channel has a large systematic uncertainty, which translates into a systematic uncertainty on the total background of 8% at 1 TeV and 21% at 2 TeV. This number is obtained by taking a ratio of the total background, where the QCD background was increased by 1 σ, and the total nominal background.

For the muon channel, the combined uncertainty on the trigger and reconstruction efficiency is estimated to be 6% at 2 TeV. This uncertainty is dominated by a conservative estimate of the impact from large energy loss due to muon bremsstrahlung in the calorimeter, which may interfere with reconstruction in the muon spectrometer if this energy loss is not well contained within the calorimeter. We are using the uncertainty that was evaluated for this source in the context of the 2011 analysis (see previous chapter). The uncertainty on the resolution due to residual misalignments in the muon spectrometer propagates to a change in the observed width of signal line-shape, and affects the sensitivity of the search. However, this effect leads to a loss of less than 3% of the events in the Z' signal peak at 2 TeV ($\pm$ one RMS), so it is neglected in the likelihood. The muon momentum scale is calibrated with a statistical precision of 0.1% using the $Z \to \ell^+\ell^-$ mass peak. As with the electron channel, the momentum calibration uncertainty has negligible impact in the muon channel search. The effect of pileup on the total signal acceptance has been studied in 2011 and found to be negligible.

As mentioned above, no theoretical uncertainties are used for the signal in the limit setting. However, their size is illustrated by the theoretical curves on the limit plots, whose

Table 4.4: Summary of systematic uncertainties on the expected numbers of events at $m_{\ell\ell} = 1$ TeV. NA indicates that the uncertainty is not applicable, and "-" denotes a negligible entry (i.e. $< 3\%$). The uncertainty on the PDF includes the QCD corrections uncertainty.

Source	Dielectrons		Dimuons	
	Signal	Background	Signal	Background
Normalization	5%	NA	5%	NA
PDF/α_s /scale	NA	7%	NA	7%
Efficiency	$< 3\%$	$< 3\%$	3%	3%
$W +$ jets and Jet background	NA	8%	NA	$< 3\%$
Total	5%	11%	6%	8%

Table 4.5: Summary of systematic uncertainties on the expected numbers of events at $m_{\ell\ell} = 2$ TeV. NA indicates that the uncertainty is not applicable, and "-" denotes a negligible entry (i.e. $< 3\%$). The uncertainty on the PDF includes the QCD corrections uncertainty.

Source	Dielectrons		Dimuons	
	Signal	Background	Signal	Background
Normalization	5%	NA	5%	NA
PDF / α_s / α_{em} / scale	NA	20%	NA	20%
Electroweak corrections	NA	4.5%	NA	4.5%
Efficiency	$< 3\%$	$< 3\%$	6%	6%
Dijet and $W +$ jets background	NA	21%	NA	$< 3\%$
Total	5%	30%	8%	21%

thickness represents the uncertainties. For most models, these theoretical uncertainties are the same as for the Z': the PDF uncertainty, which contains the uncertainty on α_s and on the QCD corrections. However, the PDF uncertainty varies, due to different couplings to up and down quarks.

Uncertainties of 3% and under at 2 TeV are neglected in the statistical treatment described below.

4.4 Results

4.4.1 Discovery statistics

As in the 2011 analysis we test the consistency of the observed data with the Standard Model prediction using several methods.

Template shape fitting

First, we use the template shape fitting technique and search for a Z' signal of unknown mass and unknown rate in ATLAS dilepton data. Template shape fitting is essentially a counting experiment in many bins of the m_{ll} distribution and the likelihood function is the product of the single bin counting experiment likelihood function over all bins in the signal region.

The significance of a potential Z' signal is summarized by a p-value, the probability of observing an outcome of an analysis at least as signal-like as the one observed in data, assuming that a signal is absent. The common convention is that a p-value less than 1.35×10^{-3} constitutes evidence for a signal and a p-value less than 2.87×10^{-7} constitutes a discovery. These are one-sided integrals of the tails of a unit Gaussian distribution beyond $+3\sigma$ and $+5\sigma$, respectively.

Experimental outcomes are ranked on a one-dimensional scale using a test statistic that is used to calculate the p-value. A natural choice for the test statistic is based on the Neyman-Pearson lemma which states that when performing a hypothesis test between two hypotheses - in our case one assuming the presence of signal and background (S+B) and one hypothesis that assumes only SM background (B) - the log-likelihood-ratio (LLR) $LLR = -2ln\frac{L(S+B)}{L(B)}$ is the best test to reject (B) in favor of (S+B).

Since the mass and the rate of a hypothetical Z' is unknown *a-priori*, we perform a likelihood fit for the best-fit signal cross section ($\sigma_{Z'}$) and the best-fit mass of Z' ($M_{Z'}$) present in data. This approach accounts naturally for the 'look elsewhere effect'.

Figure 4.9 shows the absolute value of the LLR test statistic as a function of $\sigma_{Z'}$ and $M_{Z'}$ for the likelihood fit to ATLAS data in the dielectron (left) and dimuon channel (right), while Figure 4.10 shows the same for the combination of all channels.

For the dielectron sample we observe a p-value of 8.6% and for the dimuon sample, we

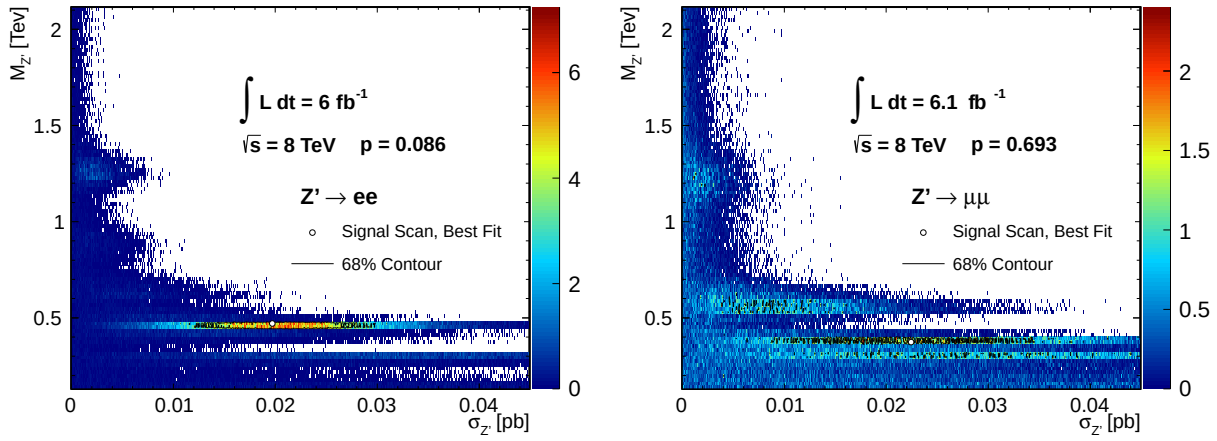

Figure 4.9: Absolute value of the log-likelihood-ratio test statistic as a function of $\sigma_{Z'}$ and $M_{Z'}$ for the likelihood fit to ATLAS data in the dielectron (left) and dimuon channel (right).

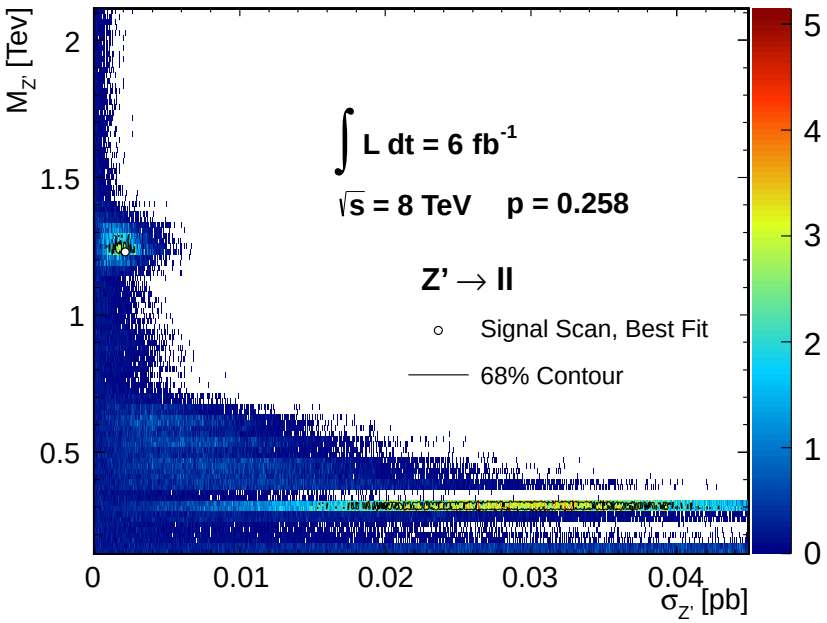

Figure 4.10: Absolute value of the log-likelihood-ratio test statistic as a function of $\sigma_{Z'}$ and $M_{Z'}$ for the likelihood fit to ATLAS data for the combination of the dielectron and dimuon channel.

observe a p-value of 69%. For the combination of both channels, we observe a p-value of 26%.

Local significances

We also display the significance of differences between data and SM prediction for each bin in the dilepton invariant mass spectra using a tool developed by G. Choudalakis and D. Casadei [78]. The result is shown in figure 4.11 for both electron and muon channels. The

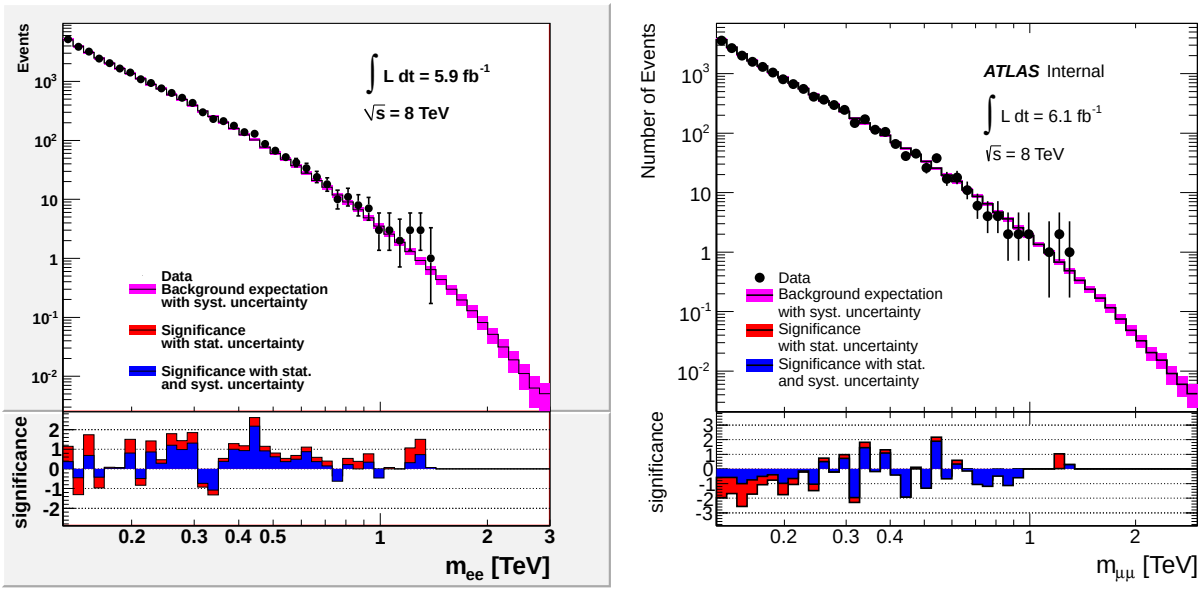

Figure 4.11: Local significance of differences between data and expectation for each bin in the dielectron (left) and dimuon (right) invariant mass spectra. The mass range covers 128 GeV to 3 TeV.

largest positive local significance including systematics is $\sim 2.1\sigma$ in the electron channel and $\sim 1.9\sigma$ in the muon channel, and the largest negative local significance is about -1.0σ and -2.0σ respectively.

In conclusion: the data are consistent with the Standard Model prediction in this search.

4.4.2 Cross section and mass limits

In the absence of a signal, an upper limit on the number of events N_X produced by the decay of a new resonance Z' is determined at the 95% confidence level (C.L.) using a Bayesian approach [75], in exactly the same manner as in the 2011 analyses (see previous chapter).

The invariant mass distribution of the data is compared to templates of the expected backgrounds and varying amounts of signal at varying pole masses in the 0.13-3.0 TeV range[3]. The templates provide the expected yield of events (μ) in each $m_{\ell\ell}$ bin: $\mu = N_X(\lambda, \bar{\nu}) + N_{DY}(\bar{\nu}) + N_{obg}(\bar{\nu})$, where λ represents the model parameters, $\bar{\nu}$ the set of nuisance parameters and N_X, N_{DY}, N_{obg} are respectively the number of new resonance, Drell-Yan and other backgrounds events. The interference between signal and Drell-Yan is neglected.

A likelihood function is defined as the product of the Poisson probabilities over all mass bins in the search region, where the Poisson probability in each bin is evaluated for the observed number of data events given the expectation from the template. The total acceptance for signal as a function of mass is propagated into the expectation. For each X pole mass, a uniform prior in the X production cross section is used.

The limit on N_X is converted into a limit on cross section times branching ratio $\sigma B(X \to \ell^+\ell^-)$ by scaling with the observed number of Z boson events and the known value of $\sigma B(Z \to \ell^+\ell^-)$:

$$\sigma B(X) = \sigma B(Z) \frac{N_X \, \mathcal{A}\epsilon(Z)}{N_Z \, \mathcal{A}\epsilon(X)},$$

where

- $\sigma B(Z) = 1.1474$ nb is the inclusive Z cross section for $m_{\ell\ell} > 60$ GeV [83];
- $\mathcal{A}\epsilon(Z)$, calculated with the inclusive Z MC sample, is the efficiency of requiring $80 < m_{\ell\ell} < 110$ GeV times the average selection efficiency for events with $m_{\ell\ell} > 60$ GeV:

  $$\mathcal{A}\epsilon(Z) = N^{MC}(\text{selected events},\ 80 < m_{\ell\ell} < 110\,\text{GeV})/N^{MC}(\text{all events},\ m_{\ell\ell} > 60\,\text{GeV});$$

- N_Z is the number of Z events in the $80 < m_{\ell\ell} < 110$ GeV range;
- $\mathcal{A}\epsilon(X)$ is the acceptance times efficiency for a given X pole mass.

$\mathcal{A}\epsilon(X)$ is obtained from a weighted average of $\mathcal{A}\epsilon$ versus $m_{\ell\ell}$ over the full line-shape between 0.13 and 3 TeV and is shown on figures 4.2 for the electron channel. The luminosity

[3]The exact range actually starts at 128.05 GeV.

normalization is replaced by a normalization to the data, using the Z number of events and acceptance above 0.13 TeV in order to cancel mass independent systematic uncertainties.

The expected exclusion limits are determined using simulated pseudoexperiments containing only Standard Model processes by evaluating the 95% C.L. upper limits for each pseudoexperiment for each fixed value of M_X. The median of the distribution of limits is chosen to represent the expected limit. The ensemble of limits is also used to find the 68% and 95% envelope of the expected limits as a function of M_X.

We perform combinations of the channels (dimuon and dielectron) by using a joint likelihood: the combination is performed by defining the likelihood function in terms of the Z' cross section in the combined channels. The details of the statistical treament are given in a separate note [79]. For two combined channels, nuisance parameters can be correlated for each process and channel.

Finally, lower limits on M_X are obtained by comparing the expected σB with the upper limits on σB as a function of M_X.

Limits on spin-1 Z'

Figure 4.12 (left) shows for the dielectron channel the 95% C.L. observed and expected exclusion limits on $\sigma B(Z' \rightarrow e^+e^-)$. It also shows the theoretical cross section times branching ratio for the $Z'_{\rm SSM}$ and for the lowest and highest σB of E_6-motivated Z' models. Similarly, Figure 3.18 (right) show the same results in the case of the dimuon selection. Figure 4.13 shows the 95% C.L. exclusion limit on σB for the combination of the electron and muon channels.

The 95% C.L. σB limit is used to set mass limits for each of the considered models. Mass limits obtained for the $Z'_{\rm SSM}$ are displayed in Table 4.6. The combined mass limit for the $Z'_{\rm SSM}$ is 2.49 TeV (observed) and 2.49 TeV (expected). The combined mass limits on the E_6-motivated models are given in Table 4.7.

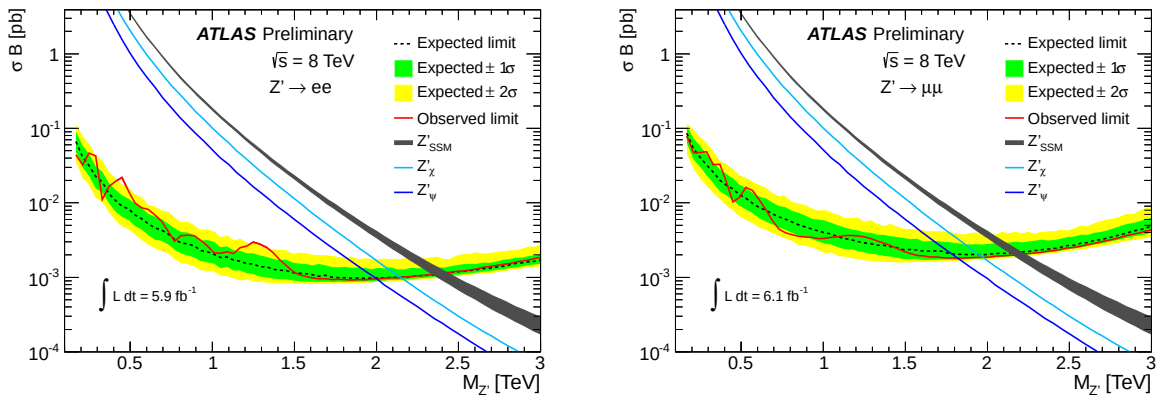

Figure 4.12: Expected and observed 95% C.L. limits on σB and expected σB for Z'_{SSM} production and the two E_6-motivated Z' models with lowest and highest σB for the di-electron (left), and the dimuon selection (right). The thickness of the SSM theory curve represents the theoretical uncertainty and holds for the other theory curves.

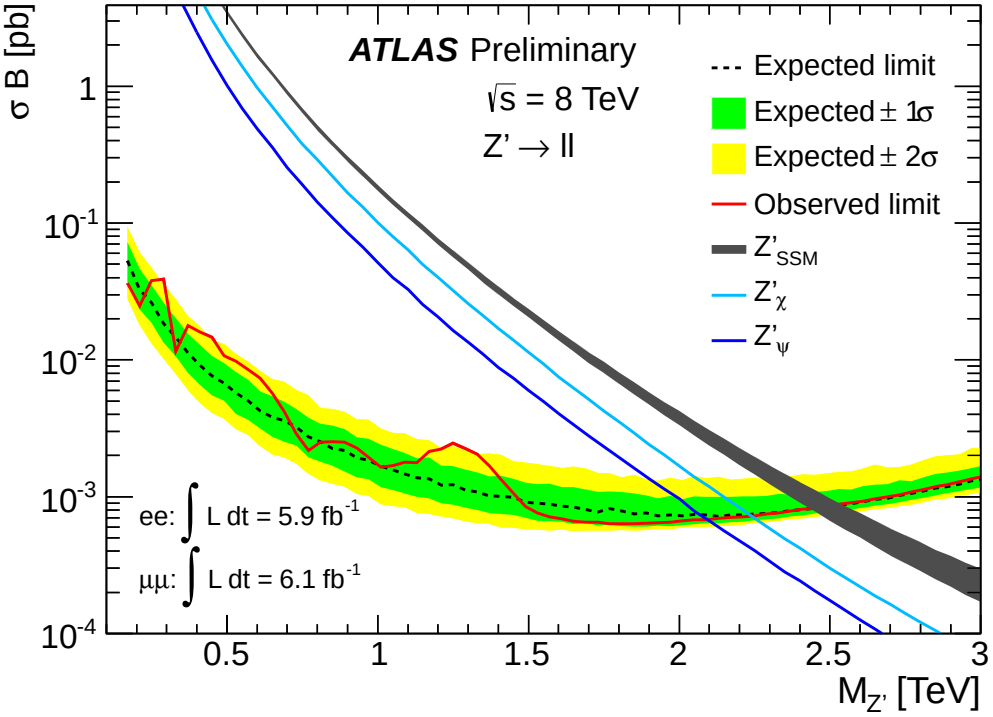

Figure 4.13: Expected and observed 95% C.L. limits on σB and expected σB for Z'_{SSM} production and the two E_6-motivated Z' models with lowest and highest σB for the combination of the electron and muon channels. The thickness of the Z'_{SSM} theory curve represents the theoretical uncertainty and holds for the other theory curves.

Table 4.6: e^+e^-, $\mu^+\mu^-$ and combined 95% C.L. mass limits on $Z'_{\rm SSM}$. In parenthesis are the results obtained with 7 TeV data described in chapter 3.

	$Z'_{\rm SSM} \to e^+e^-$	$Z'_{\rm SSM} \to \mu^+\mu^-$	$Z'_{\rm SSM} \to \ell^+\ell^-$
Observed mass limit [TeV]	2.39 (2.08)	2.19 (1.99)	2.49 (2.22)
Expected mass limit [TeV]	2.39 (2.13)	2.17 (2.00)	2.49 (2.25)

Table 4.7: Combined mass limits at 95% C.L. on the E_6-motivated Z' models. In parenthesis are the results obtained with 7 TeV data described in chapter 3.

Model	Z'_ψ	$Z'_{\rm N}$	Z'_η	$Z'_{\rm I}$	$Z'_{\rm S}$	Z'_χ
Observed mass limit [TeV]	2.09	2.10	2.15	2.14	2.18	2.24
	(1.79)	(2.22)	(1.87)	(1.86)	(1.91)	(1.97)
Expected mass limit [TeV]	2.07	2.08	2.14	2.13	2.17	2.23
	(1.87)	(1.87)	(1.92)	(1.91)	(1.95)	(2.00)

These results extend the exclusion limits obtained with the 2011 data sample. The sample presented used in my analysis is only a quarter of the data collected during the 8 TeV run. It was published by ATLAS as a preliminary results on conferences. Tables 4.6 and 4.7 show for comparison the results described on chapter 3 with the 7 TeV data. The results were not combined as this requires additional detailed study of the correlation between the two analyses. The full data set results are at he last stage of ATLAS approval and are going to be public in the coming weeks.

Appendix A

Monte Carlo samples and Z' LO cross sections

A.1 Signal samples

Tables A.1 lists the characteristics of the Monte Carlo samples for Z'_{SSM} . As already stated in the main text, the Z' samples are generated with PYTHIA with MRST2007LO**. The single mass Z' samples also include the Drell Yan contribution above a mass threshold of 0.5 times the pole mass. The cross section used in the limit computation is not the cross section of the generated samples due to this Drell Yan component; it is the cross section of the signal alone, shown in table A.3 of next subsection. The cross section of the samples have changed with respect to previous versions of the analysis because the tune parameters changed between MC10 and MC11 (see `https://twiki.cern.ch/twiki/bin/view/AtlasProtected/McProductionCommonParameters`). Table A.2 lists the characteristics of the Monte Carlo samples for Kaluza-Klein $\mu^+\mu^-$ signals; these samples are not currently used due to the PDF mismatch. The electron equivalent has not been requested yet because of a previous bug in specific implementation of the process in PYTHIA8 and because the fixed version has not yet been integrated into ATHENA in the time the muon request was submitted.

Table A.1: Monte Carlo Z' samples used for the study. The first four columns give the mass, mass threshold (M_{min}), width and leptonic branching fraction. Next is the ATLAS Monte Carlo run number followed by the cross section time branching fraction reported by the generator. The last columns give the number of generated events and the integrated luminosity $L_{\text{int}} = N_{\text{evt}}/(\sigma B)$ (not taking into account the pile-up reweighting).

Mass	M_{min}	Γ	$B(Z' \to \ell^+\ell^-)$	Run number		σB [fb]		L_{int}
[GeV]	[GeV]	[GeV]	[%]	e	μ	generated	N_{evt} [k]	[fb^{-1}]
≥ 10				115494	115495		388	
250	125	6.87	3.36	115272	115269	35401.	20	0.48
500	250	14.56	3.20	115273	115270	2607.1	20	6.7
750	375	22.64	3.10	115274	115271	473.49	20	37.5
1000	500	30.64	3.06	105603	105601	124.66	20	143.
1250	625	38.60	3.05	105549	105534	39.887	20	469.
1500	750	46.55	3.04	105624	105625	14.38	20	1312.
1750	875	54.49	3.03	105554	105544	5.6744	20	3597.
2000	1000	62.43	3.03	105409	105349	2.4357	20	9091.

Table A.2: Monte Carlo KK samples used for the study, for $m_{\mathrm{KK}} = 2$ TeV for muons only. The first column gives the phase-space for the generation ($m_{\mu\mu}$ in GeV). The next two columns are the ATLAS Monte Carlo run numbers, followed by the cross section times branching fraction reported by the generator. The last two columns give the number of generated events and the integrated luminosity $L_{\mathrm{int}} = N_{\mathrm{evt}}/(\sigma B)$ (not taking into account the pile-up reweighting

$\mu\mu$ mass bin	Run number	σB [pb]	N_{evt} [k]	L_{int} [fb^{-1}]
$\gamma_{\mathrm{KK}}/Z_{\mathrm{KK}}\,(120-450)$	145016	7.7227	40	0.00518
$\gamma_{\mathrm{KK}}/Z_{\mathrm{KK}}\,(450-850)$	145017	0.021906	10	0.456
$\gamma_{\mathrm{KK}}/Z_{\mathrm{KK}}\,(850-1300)$	145018	0.0002006	10	49.
$\gamma_{\mathrm{KK}}/Z_{\mathrm{KK}}\,(1300-1800)$	145019	0.0013579	10	7.36
$\gamma_{\mathrm{KK}}/Z_{\mathrm{KK}}\,(1800-2300)$	145020	0.0094190	10	1.06
$\gamma_{\mathrm{KK}}/Z_{\mathrm{KK}}\,(2300-2800)$	145021	0.000047462	10	210.
$\gamma_{\mathrm{KK}}/Z_{\mathrm{KK}}\,(2800-3300)$	145022	0.00000029864	10	33485.
$\gamma_{\mathrm{KK}}/Z_{\mathrm{KK}}\,(>3300)$	145023	0.0000032102	10	3115.

A.2 Z' LO cross sections

Table A.3 displays the LO Z' cross sections used in the limit calculation for various masses. Contrary to the simulated sample cross section, which include Drell Yan production (and interference), these cross sections are for Z' production only. Another difference with simulated cross sections is that the MSTW2008lo90cl PDF is used, for consistency with the calculation of the Drell Yan cross section. The actual mass spacing used in the limits calculation is 40 GeV.

Table A.3: LO order cross sections used in the limit calculation for all Z' models

Mass [GeV]	$\sigma B(Z'_{\mathrm{SSM}})$ [fb]	$\sigma B(Z'_{\mathrm{S}})$ [fb]	$\sigma B(Z'_{\mathrm{N}})$ [fb]	$\sigma B(Z'_{\psi})$ [fb]	$\sigma B(Z'_{\chi})$ [fb]	$\sigma B(Z'_{\eta})$ [fb]	$\sigma B(Z'_{\mathrm{I}})$ [fb]
250	2.735e+04	1.471e+04	9.223e+03	8.132e+03	1.589e+04	9.566e+03	1.330e+04
500	2.038e+03	1.080e+03	683.0	596.8	1.163e+03	694.6	951.8
750	366.8	188.5	119.7	106.9	210.1	123.2	170.0
1000	94.77	46.90	30.32	26.90	51.83	31.40	41.51
1250	29.60	13.63	9.069	8.171	15.56	9.704	11.87
1500	10.33	4.310	3.003	2.732	5.064	3.229	3.741
1750	3.876	1.440	1.037	9.833e-01	1.747	1.195	1.219
2000	1.579	5.090e-01	3.793e-01	3.706e-01	6.410e-01	4.550e-01	4.221e-01
2250	6.935e-01	1.911e-01	1.440e-01	1.422e-01	2.493e-01	1.775e-01	1.571e-01
2500	3.296e-01	8.032e-02	5.754e-02	5.668e-02	1.044e-01	7.255e-02	6.530e-02
2750	1.729e-01	3.834e-02	2.464e-02	2.395e-02	4.888e-02	3.083e-02	3.066e-02
3000	1.000e-01	2.102e-02	1.151e-02	1.064e-02	2.591e-02	1.399e-02	1.690e-02

A.3 Background samples

Tables A.4 to A.7 list the background samples that are used in this analysis. The binned DY samples (ee and $\mu\mu$) are also used as a base for reweighting some of the signals and produce KK and Z' (within the g^4 study).

Table A.4: Monte Carlo Drell Yan samples used for the study. The first column gives the mass range [GeV] and the second, third and fourth are the ATLAS Monte Carlo run numbers. The fifth column is the cross section time branching ratio reported by the generator. The next column is the number of generated events and the last is the integrated luminosity $L_{\text{int}} = N_{\text{evt}}/(\sigma B)$ for each lepton flavour (not taking into account the pile-up reweighting). (*) The mass binned $\tau\tau$ samples have 5 times less integrated luminosity (20k events). The cross section of the inclusive samples calculated at QCD NNLO is 989 pb.

	Run number			σB [pb]		
Process	e	μ	τ	generated	N_{evt} [k]	L_{int} [fb^{-1}]
$Z \to e^+e^-$	106046			834.6	9986	10.
$Z \to \mu^+\mu^-$		106047		834.6	9994	10.
$Z \to \tau\tau$			106052	834.6	495	0.5
$Z(75,120) \to \ell\ell$	105466	145001	105488	798.36	100*	0.12
$Z(120,250) \to \ell\ell$	105467	145002	105489	8.53	100*	11.7
$Z(250,400) \to \ell\ell$	105468	145003	105490	0.410	100*	243.
$Z(400,600) \to \ell\ell$	105469	145004	105491	0.0664	100*	1506.
$Z(600,800) \to \ell\ell$	105470	145005	105492	0.01095	100*	9128.
$Z(800,1000) \to \ell\ell$	105471	145006	105493	0.002647	100*	37778.
$Z(1000,1250) \to \ell\ell$	105472	145007	105494	0.0008901	100*	112340.
$Z(1250,1500) \to \ell\ell$	105473	145008	105495	0.00023922	100*	418025.
$Z(1500,1750) \to \ell\ell$	105474	145009	105496	0.00007343	100*	1361674.
$Z(1750,2000) \to \ell\ell$	105475	145010	105497	0.00002464	100*	4057947.
$Z(2000,2250) \to \ell\ell$	145263	145011	105498	0.00000876	100*	11413049.
$Z(2250,2500) \to \ell\ell$	145264	145012	105498	0.00000322	100*	31025068.
$Z(2500,2750) \to \ell\ell$	145265	145013	105498	0.00000120	100*	82829454.
$Z(2750,3000) \to \ell\ell$	145266	145014	105498	0.00000045	100*	223398789.
$Z(3000,) \to \ell\ell$	145267	145015	105498	0.00000025	100*	390838740.

Table A.5: Monte Carlo W/Z background samples used for the study. The first column lists the Physics process and the second is the ATLAS Monte Carlo run number. The third and fourth columns are the cross section time branching ratios first reported by the generator, and second calculated as follows: the inclusive K-factor given by the ratio of calculated (10.46 nb [69]) over generated cross sections of inclusive production (all samples added together) is applied to the generated cross section of the high-mass bin samples. The next column is the number of generated events and the last is the integrated luminosity $L_{\text{int}} = N_{\text{evt}}/(\sigma B)$ (not taking into account the pile-up reweighting).

		σB [pb]			
Process	Run number	generated	calculated	N_{evt} [k]	L_{int} [fb^{-1}]
$W \to e\nu + 0$ parton	107680	6933.	8287.1	499.6	0.06
$W \to e\nu + 1$ parton	107681	1305.1	1560.0	2499.6	1.6
$W \to e\nu + 2$ partons	107682	378.1	452.0	2000	4.4
$W \to e\nu + 3$ partons	107683	101.9	121.8	500	4.1
$W \to e\nu + 4$ partons	107684	25.7	30.7	149.5	4.9
$W \to e\nu + 5$ partons	107685	7.0	8.4	70	8.4
$W \to \mu\nu + 0$ parton	107690	6918.7	8284	3466.5	0.4
$W \to \mu\nu + 1$ parton	107691	1304.2	1561.6	642	0.4
$W \to \mu\nu + 2$ partons	107692	378.5	453.3	3769	8.3
$W \to \mu\nu + 3$ partons	107693	101.6	121.7	1010	8.3
$W \to \mu\nu + 4$ partons	107694	25.9	31.0	255	7.3
$W \to \mu\nu + 5$ partons	107695	6.9	8.3	70	8.4
$W \to \tau\nu + 0$ parton	107700	6933.	8287.	3418	0.4
$W \to \tau\nu + 1$ parton	107701	1305.	1560.	2499	1.6
$W \to \tau\nu + 2$ partons	107702	378.	452.	3751	8.3
$W \to \tau\nu + 3$ partons	107703	102.	122.	1010	8.3
$W \to \tau\nu + 4$ partons	107704	26.	31.	250	7.3
$W \to \tau\nu + 5$ partons	107705	7.	8.	65	8.

Table A.6: Monte Carlo diboson background samples used for the study. The first column lists the Physics process and the second is the ATLAS Monte Carlo run number. The third column is the filter efficiency. The fourth and fifth columns are the cross section (time branching ratios) time filter efficiency first reported by the generator, and second calculated as follows: the inclusive K-factor given by the ratio of calculated over generated cross sections of the inclusive sample are applied to the generated cross section of the high-mass bin samples. The next column is the number of generated events and the last is the integrated luminosity $L_{\text{int}} = N_{\text{evt}}/(\sigma B)$ (not taking into account the pile-up reweighting). The lepton filter is 1 lepton with $p_T > 10$ GeV, $|\eta| < 2.8$ for the inclusive mass samples, 1 electron with $p_T > 15$ GeV, $|\eta| < 2.6$ for the binned mass electron samples and 1 muon with $p_T > 15$ GeV, $|\eta| < 2.8$ for the binned mass muon samples.

Process	Run number	ϵ_f (filter efficiency)	$\sigma B \times \epsilon_f$ [fb] generated	$\sigma B \times \epsilon_f$ [fb] calculated	N_{evt} [k]	L_{int} [fb^{-1}]
WW (1 lepton filter)	105985	0.38947	12115.	17487.	1000	57.
WZ (1 lepton filter)	105987	0.31043	3565.	5743.	1000	180.
ZZ (1 lepton filter)	105986	0.21319	975.	1271.	250	198.
WW ($M_{ee} = 0.4 - 1$ TeV)	145487	0.00589	2.134	3.131	20	6388.
WW ($M_{ee} = 1 - 1.6$ TeV)	145488	0.0000610	0.022	0.032	20	625000.
WZ ($M_{ee} = 0.4 - 1$ TeV)	145493	0.00251	1.113	1.558	20	12836.
WZ ($M_{ee} = 1 - 1.6$ TeV)	145494	0.0000725	0.032	0.045	20	444444.
ZZ ($M_{ee} = 0.4 - 1$ TeV)	145499	0.00114	0.383	0.448	20	44643.
ZZ ($M_{ee} = 1 - 1.6$ TeV)	145500	0.0000206	0.0069	0.0081	20	2469136.
WW ($M_{\mu\mu} = 0.4 - 1$ TeV)	145490	0.00716	2.598	3.808	20	5252.
WW ($M_{\mu\mu} = 1 - 1.6$ TeV)	145491	0.0000739	0.027	0.039	20	508821.
WZ ($M_{\mu\mu} = 0.4 - 1$ TeV)	145496	0.00296	1.315	1.840	20	10869.
WZ ($M_{\mu\mu} = 1 - 1.6$ TeV)	145497	0.0000812	0.036	0.050	20	396317.
ZZ ($M_{\mu\mu} = 0.4 - 1$ TeV)	145502	0.00133	0.449	0.525	20	38116.
ZZ ($M_{\mu\mu} = 1 - 1.6$ TeV)	145503	0.0000237	0.0080	0.0093	20	2144458.

Table A.7: Monte Carlo $t\bar{t}$ background MC11 samples used for the study. The first column lists the Physics process including the mass or mass range [GeV] and the second is the ATLAS Monte Carlo run number. The third and fourth columns are the cross section time branching ratios reported by the generator and calculated as described in the text. The next column is the number of generated events and the last is the integrated luminosity $L_{\text{int}} = N_{\text{evt}}/(\sigma B)$ (not taking into account the pile-up reweighting).

Process	M_{ee} [GeV]	Run number	ϵ_f (filter efficiency)	$\sigma B \times \epsilon_f$ [pb] generated	calculated	N_{evt} [k]	L_{int} [fb^{-1}]
$t\bar{t} \to \ell X$		105200	0.54259	79.0	89.4	14995	168.

Appendix B

Dependence on the coupling scale of the $q\bar{q} \to Z/\gamma^* + X \to \ell^+\ell^-$ cross section

B.1 The hard process cross section

The differential cross section for the hard process $q\bar{q} \to \gamma^*/Z + X \to \ell^+\ell^-$ is

$$\frac{d\sigma}{ds_{\ell\ell}} \propto \left| \frac{Q_q Q_\ell}{s_{\ell\ell}} + \frac{g_q^Z g_\ell^Z}{s_{\ell\ell} - m_Z^2 + \imath\Gamma_Z m_Z} + g^2 \frac{g_q^X g_\ell^X}{s_{\ell\ell} - m_X^2 + \imath g^2 \Gamma_X m_X} \right|^2 \tag{B.1}$$

where g_f^X and Γ_X are the nominal values predicted by the model, and the g scale parametrizes the strength of the single-fermion couplings. Since the width is proportional to the square of the couplings, g also enters the width term. The angular term and the summation over spins (helicities) is omitted for convenience. The first two terms are simply the SM Drell-Yan (DY). The last term is the new Physics, denoted by X where X may correspond to $Z'_{\rm SSM}$ or to the first KK excitation. Note that for the complete description of the KK tower, one needs to sum also the higher excitations up to infinity but for KK masses above ~ 1.5 TeV the impact of the $n > 1$ excitations should be negligible within the current mass window 70 GeV$\leq m_{\ell\ell} \leq$3000 GeV, considering the current luminosity. In the later, there should be a similar term for the KK photon,

$$\frac{d\sigma}{ds_{\ell\ell}} \propto \left| \mathrm{DY} + g^2 \frac{2 g_q^Z g_\ell^Z}{s_{\ell\ell} - m_{Z_{\rm KK}}^2 + \imath g^2 \Gamma_{Z_{\rm KK}} m_{Z_{\rm KK}}} + g^2 \frac{2 Q_q Q_\ell}{s_{\ell\ell} - m_{\gamma_{\rm KK}}^2 + \imath g^2 \Gamma_{\gamma_{\rm KK}} m_{\gamma_{\rm KK}}} \right|^2 \tag{B.2}$$

where the factor 2 is introduced by the KK couplings due to the unique S^1/Z_2 compactification.

For simplicity, the discussion will be limited to the $X = Z'_{\mathrm{SSM}}$ case where the cross section is given by equation B.1 and where the Z'couplings are SM-like, i.e. $g_f^X = g_f^Z$. In the KK case, the two KK resonances (γ_{KK} and Z_{KK}) have almost the same denominator while the two numerators are different. This enables to treat the two KK resonances as a single resonance (X) with couplings $\propto 2\left(g_q^Z g_\ell^Z + Q_q Q_\ell\right)$.

B.2 Expansion in powers of g (very off-X-shell)

Starting from equation B.1 while putting $g_q^X = g_q^Z \equiv g_q$, we can separate the cross section into three additive terms; pure DY, pure X and the interference term I.

$$|\mathrm{DY}|^2 = \left|\frac{Q_q Q_\ell}{s_{\ell\ell}} + \frac{g_q g_\ell}{s_{\ell\ell} - m_Z^2 + \imath\Gamma_Z m_Z}\right|^2 \propto g^0 \tag{B.3}$$

$$|X|^2 = g^4\left|\frac{g_q g_\ell}{s_{\ell\ell} - m_X^2 + \imath g^2 \Gamma_X m_X}\right|^2 = g^4 \frac{g_q^2 g_\ell^2}{\left(s_{\ell\ell} - m_X^2\right)^2 + g^4\Gamma_X^2 m_X^2} \propto \frac{g^4}{c_1^2 + g^4} \tag{B.4}$$

$$I \equiv 2\mathrm{Re}\left[\mathrm{DY}^* X\right] \propto g^2 \frac{c_2 + c_3 g^2}{c_4^2 + g^4} \tag{B.5}$$

where $c_{i=1,\ldots,4}$ are real numbers depending on $s_{\ell\ell}$ and on the constant couplings, masses and widths of the γ^*/Z and X.

B.2.1 The pure signal term

Starting from equation B.4 we rewrite it in terms of $x \equiv \frac{g^4}{c_1^2}$ where c_1^2 is simply $\left(\frac{s_{\ell\ell} - m_X^2}{\Gamma_X m_X}\right)^2$ and where g^4 is allowed to vary between 0 and $\mathcal{O}(100)$. For very off-shell $s_{\ell\ell}$ values, this is approximately $c_1^2 \sim \left(\frac{m_X}{\Gamma_X}\right)^2 \gg 1$ so the approximation is justified for these values of $s_{\ell\ell}$ especially for small values of g^4. In that cases, x is small enough to allow expansion in powers of $x \propto g^4$ and we get that

$$|X|^2 \sim \frac{g^4}{c_1^2 + g^4} = \frac{x}{1+x} = x - x^2 + x^3 - x^4 + \ldots \tag{B.6}$$

For $x \to 0$ one can keep only the first order in x and therefore see that $|X|^2 \sim g^4$.

B.2.2 Justification of the $|X|^2 \sim g^4$ approximation

In the Z' case, the current limit lies around ∼2 TeV where the $\ell\ell$ data goes up to ∼1.5 TeV. In light of that, being "off-shell" means e.g. $\sqrt{s_{\ell\ell}} \approx 1$ TeV where $m_X \approx 2$ TeV so, in that case one can see that

$$c_1^2 = \left(\frac{1000^2 - 2000^2}{120 \times 2000}\right)^2 \approx 156 \tag{B.7}$$

The expansion, which is therefore done in $x = \frac{g^4}{156} \approx \frac{1}{156} << 1$, is very much justified. In the last ste the couplings scale is taken to be of order 1 since at $g = 1$, one returns to the SSM case. In the "more realistic" scenarios, g should be even smaller since in a given $g > 1$ value, one needs to set the KK mass to be very large in order to explain why this signature has not been detected up to now.

B.2.3 The interference term

The interference term may be expanded in the same way as the X term. However, this is much more complicated. Instead, since the interference feature of a heavy KK resonance is the only feature seen in the low mass range (e.g. $m_{\rm KK} \geq 3.5$ TeV where the analyzed mass window is $m_{\ell\ell} \leq 3$ TeV), it is sufficient to look on $s_{\ell\ell}$ values that are very off "X"-shell, i.e. below the resonance but much above the Z-peak. This means that m_Z^2 can be neglected with respect to $s_{\ell\ell}$ and, the Z width term can also be neglected with respect to $s - m_Z^2$. In this case, the Z looks like a photon but with Z couplings. This can be seen by approximating equation B.5 for off-shell cases e.g.

$$\begin{aligned}
I_{\rm off-shell} &\approx 2{\rm Re}\left[{\rm Conj}\left(\frac{Q_q Q_\ell}{s_{\ell\ell}} + \frac{g_q^Z g_\ell^Z}{s_{\ell\ell}}\right) \times g^2 \frac{g_q^X g_\ell^X}{s_{\ell\ell} - m_X^2 + \imath g^2 \Gamma_X m_X}\right] \\
&= 2g^2 \frac{Q_q Q_\ell + g_q^Z g_\ell^Z}{s_{\ell\ell}} {\rm Re}\left[\frac{g_q^X g_\ell^X \left(s_{\ell\ell} - m_X^2 - \imath g^2 \Gamma_X m_X\right)}{\left(s_{\ell\ell} - m_X^2\right)^2 + g^4 \Gamma_X^2 m_X^2}\right] \\
&= g^2 \frac{2 g_q^X g_\ell^X \left(Q_q Q_\ell + g_q^Z g_\ell^Z\right)}{s_{\ell\ell}} \times \frac{s_{\ell\ell} - m_X^2}{\left(s_{\ell\ell} - m_X^2\right)^2 + g^4 \Gamma_X^2 m_X^2} \\
&= \frac{2 g_q^X g_\ell^X \left(Q_q Q_\ell + g_q^Z g_\ell^Z\right)}{s_{\ell\ell}} \frac{s_{\ell\ell} - m_X^2}{\Gamma_X^2 m_X^2} \times \frac{1}{g^2} \frac{g^4}{c_1^2 + g^4} \\
&= \frac{2 g_q^X g_\ell^X \left(Q_q Q_\ell + g_q^Z g_\ell^Z\right)}{s_{\ell\ell}} \frac{s_{\ell\ell} - m_X^2}{\Gamma_X^2 m_X^2} \times \frac{1}{g^2} \times \frac{g^4}{c_1^2 + g^4}
\end{aligned} \tag{B.8}$$

We already saw from equation B.6 that for $x \equiv \frac{g^4}{c_1^2} \to 0$ the last multiplier in equation B.9 is $\frac{1}{c_1^2} g^4$ to first order in x but this time it is multiplied by $\frac{1}{g^2}$ so the result is $I_{\rm off-shell} \propto g^2$.

B.3 Conclusions

We see that the pure signal (resonance) term is proportional to g^4 and the interference term is proportional to g^2. The complete cross section expanded up to first order in x is,

$$\begin{aligned} \frac{d\sigma_{\text{off-shell}}}{ds_{\ell\ell}} &= |\text{DY}|^2 + 2\text{Re}\left[\text{DY}^* X\right] + |X|^2 \\ &\sim |\text{DY}|^2 + \quad g^2 \frac{A}{c_1^2} \quad + g^4 \frac{B}{c_1^2} \end{aligned} \tag{B.9}$$

where A, B and c_1^2 are functions of the couplings masses, widths and $s_{\ell\ell}$, but not of the scale g.

Appendix C

Signal templates

C.1 Normalized templates

The templates for the signals are shown in figure C.1. The 2D templates for $Z_{\mathrm{KK}}/\gamma_{\mathrm{KK}}$ signal plus backgrounds are shown in figures C.2 and C.3 for two example pole masses (dielectron and dimuon channels respectively).

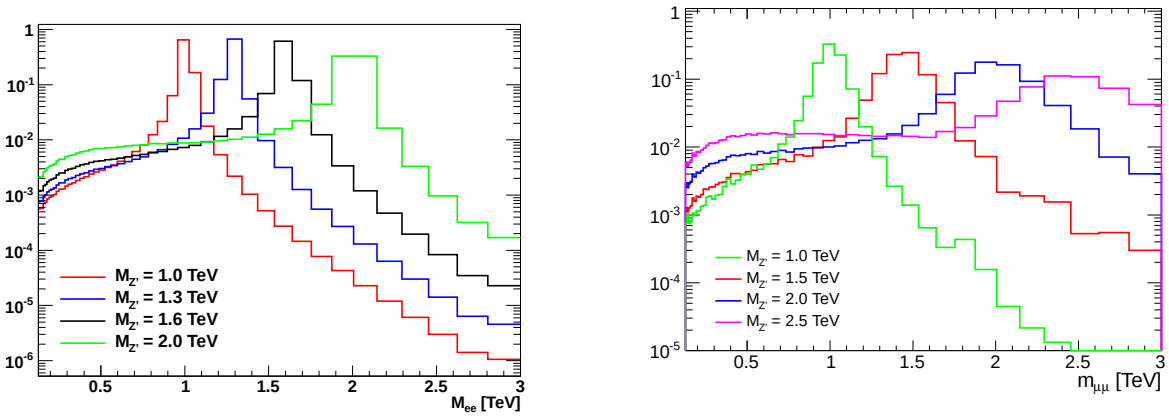

Figure C.1: Dielectron m_{ee} (left) and loose dimuon $m_{\mu\mu}$ (right) templates for a few Z'_{SSM} pole masses

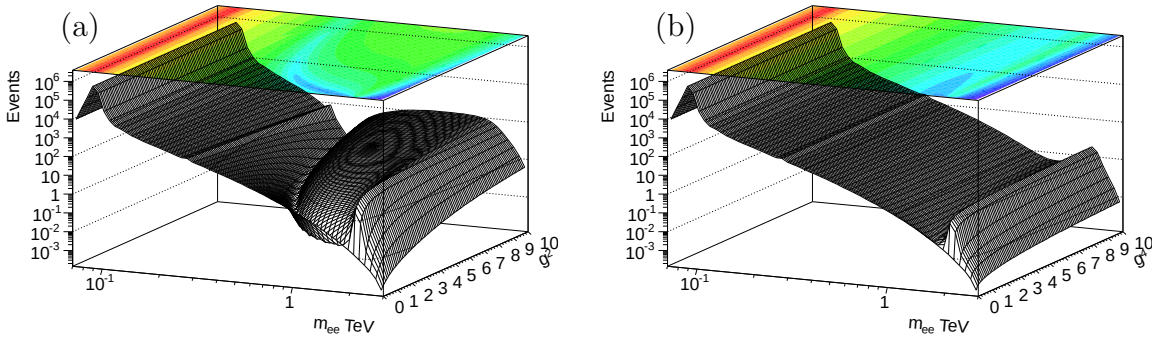

Figure C.2: The nominal $2d$ templates (m_{ee} vs. g^N) at 2 TeV. The KK template for g^2 in (a) and the Z'_{SSM} template for g^4 in (b)

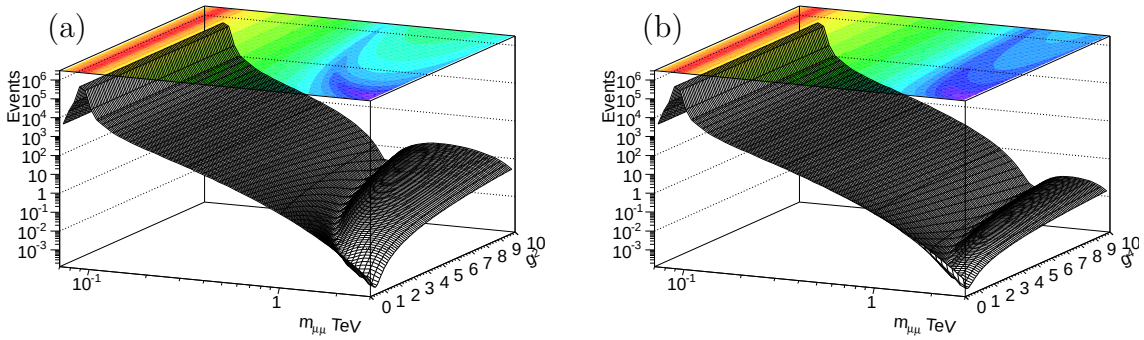

Figure C.3: The nominal $2d$ templates ($m_{\mu\mu}$ vs. g^N) at 4 TeV. The KK template for g^2 in (a) and the KK template for g^4 in (b). Unlike in the 2 TeV figure (figure C.2), the Z'_{SSM} at 4 TeV is not shown here since it looks essentially the same as the DY ($g = 0$) for any value $g^4 > 0$ in the range of dimuon masses up to 3 TeV.

C.2 Templates scaled with cross section

In the fitting procedure performed to compute the limits, the normalized templates shown above are used with a floating normalization. To give a feeling of the relative cross section of the searched signals, a few dielectron templates with masses between 1 and 2 TeV with absolute normalization according to their cross section for Z'_{SSM} signals are shown in Figure C.4.

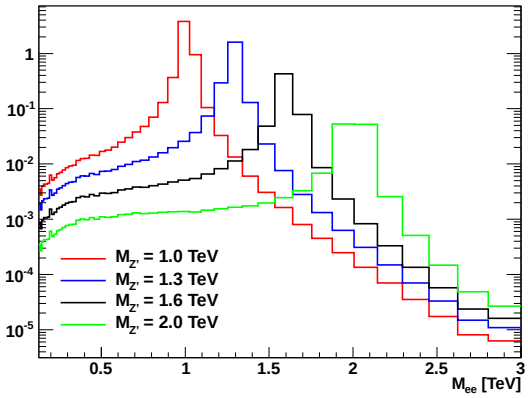

Figure C.4: Dielectron m_{ee} templates normalized to cross section for a few Z'_{SSM} pole masses.

C.3 Template reweighting validation

Figures C.5 show the validation of the dimuon templates for the Z'_{SSM} signals.

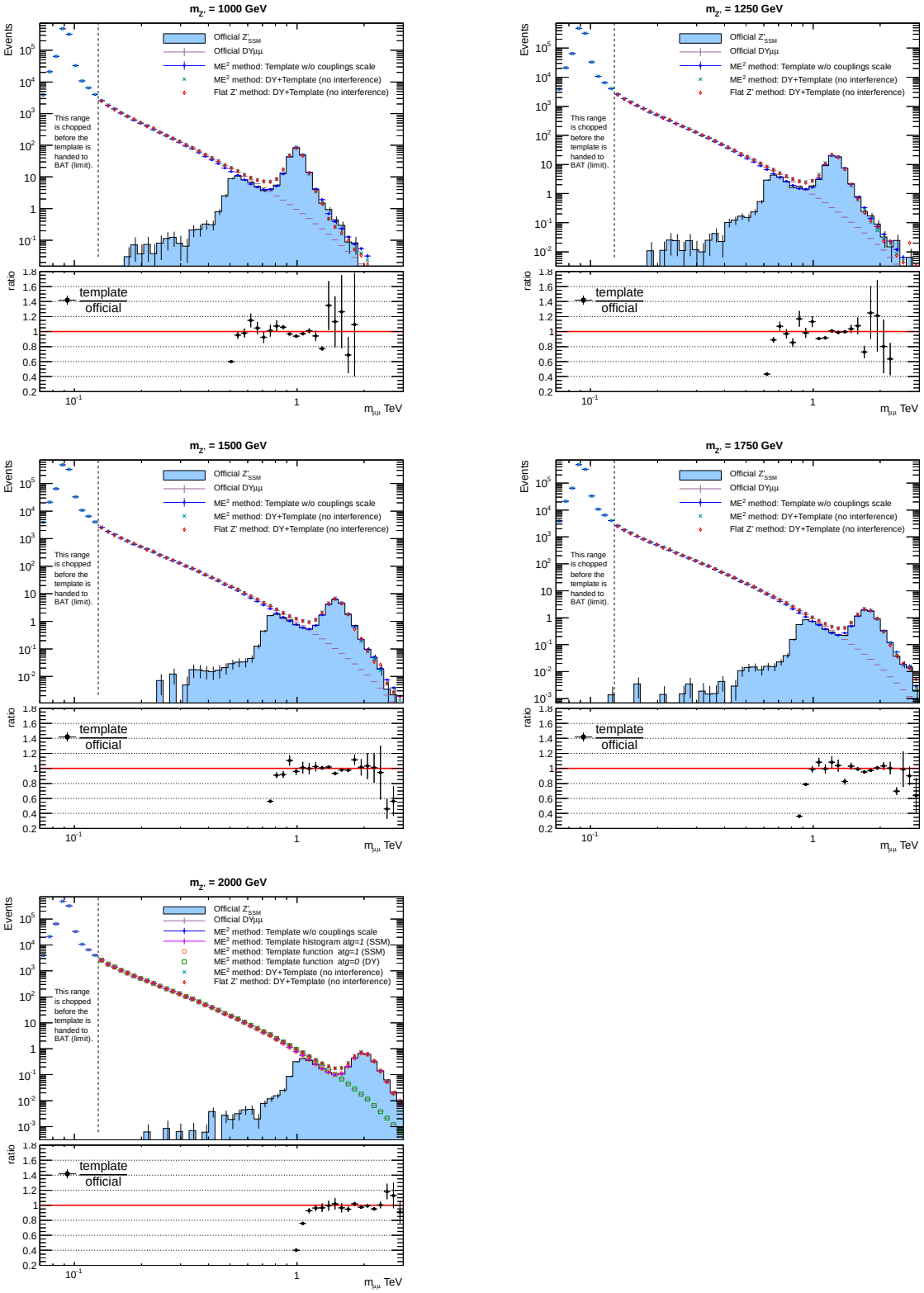

Figure C.5: Dimuon invariant mass ($m_{\mu\mu}$) distribution after event selection, of Z' signals (SSM) at five pole mass values: 1.0, 1.25, 1.5, 1.75 and 2 TeV. The bottom plot shows the ratio of the ME^2 template "without couplings scale", i.e. for SSM Z' (blue points) over the official Z'_{SSM} sample (blue histogram)

Appendix D

Specificities of the $Z_{\mathrm{KK}}/\gamma_{\mathrm{KK}}$ model (coupling limits)

Since the DY is an integral part of the signal, it implies that the systematic uncertainties, that should be also handed over to BAT, have to be two dimensional (the $g^N - m_{\ell\ell}$ space, $N = 2, 4$) like the signal templates themselves. However, there are systematic uncertainties that should be applied only on the DY part of the template while others should be applied only on the new Physics part of the templates. This can be done by defining the relative systematic uncertainty template,

$$T_{\text{syst.}} = \frac{T^{\mathrm{DY}+X}_{\text{syst.up}}}{T^{\mathrm{DY}+X}_{\text{nominal}}} - 1 \tag{D.1}$$

where X is the new Physics part, $T^{\mathrm{DY}+X}_{\text{syst.up}}$ is the $(+1\sigma)$ overestimated $2d$ template due to a certain systematic uncertainty and $T^{\mathrm{DY}+X}_{\text{nominal}}$ is the nominal $2d$ template. This is of course done bin-by-bin in the two dimensions. The way to obtain the overestimated $2d$ template ($T^{\mathrm{DY}+X}_{\text{syst.up}}$) correctly is to follow these steps;

- for a DY-only uncertainty, subtract the $(1d)$ DY part from the $(2d)$ nominal template and re-add the DY $+1\sigma$ overestimate
- for a new-Physics-only uncertainty, subtract the $(1d)$ DY part from the $(2d)$ template, modify the remaining $2d$ part to get its $+1\sigma$ overestimate (this corresponds to modifying the $|\mathrm{DY} + X|^2 - |\mathrm{DY}|^2$ "signal-only" shape). Then, re-add the nominal DY part.
- For the resolution systematic uncertainty, $T^{\mathrm{DY}+X}_{\text{syst.up}}$ is simply the over-smeared, full $(2d)$ template

The modification of the $2d$ part (from the second point above) is done for every g^N-slice of the template, where the standard mass-dependent relative uncertainties are used in the same way as for the σB limits.

Examples of the relative systematic uncertainty templates can be seen in figures D.1 to D.2.

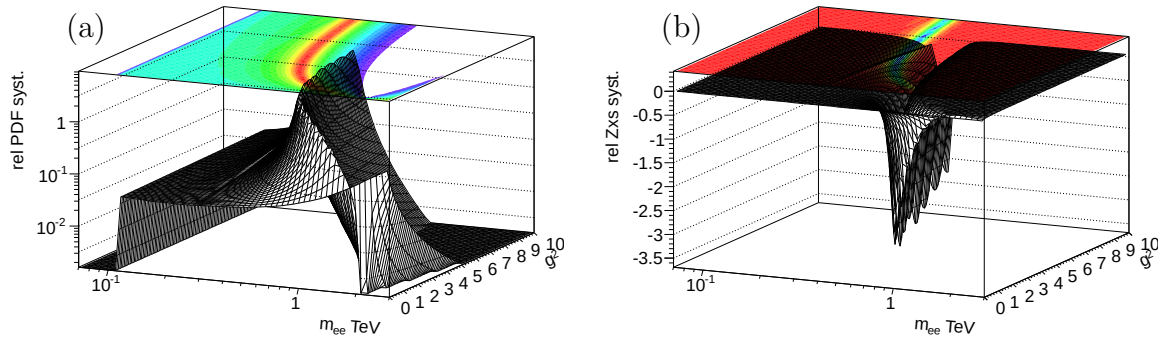

Figure D.1: Examples of two relative systematic uncertainty $2d$ templates (m_{ee} vs. g^N) at 2 TeV for the KK model and for g^2. The PDF rel. uncertainty template where only the DY part was overestimated in (a) and the Z cross section rel. uncertainty template where only the KK part was overestimated in (b).

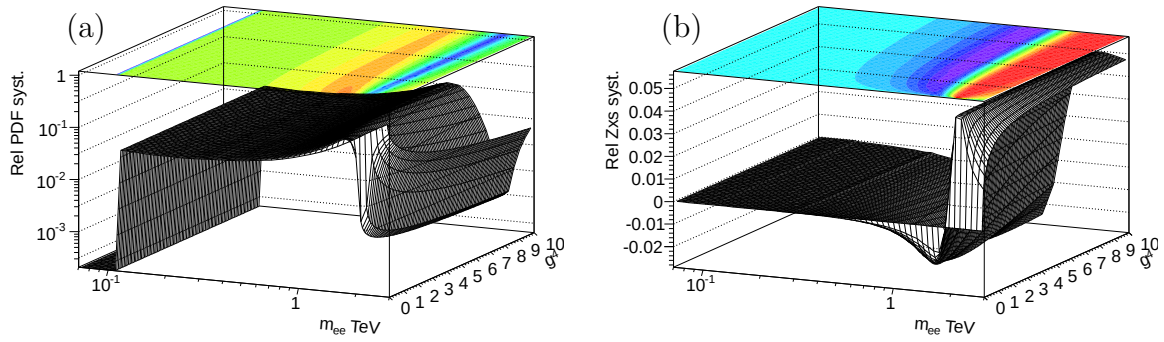

Figure D.2: Examples of two relative systematic uncertainty $2d$ templates (m_{ee} vs. g^N) at 2 TeV for the Z'_{SSM} model and for g^4. The PDF rel. uncertainty template where only the DY part was overestimated in (a) and the Z cross section rel. uncertainty template where only the KK part was overestimated in (b).

The likelihood for the g-limits

The likelihood function for a given "X" mass is

$$L_{m_X}\left(g, \{N^k_{\text{b,noDY}}\}, \{\theta_j\}|\text{data}\right) = \prod_k^{\text{Bins}} \frac{\left(N^k_{\text{s+b}}\right)^{N^k_{\text{obs}}} \times e^{-N^k_{\text{s+b}}}}{N^k_{\text{obs}}!} \times \prod_j^{\text{Syst.}} G\left(\theta_j, 0, 1\right) \times \text{Prior}\left(g\right) \tag{D.2}$$

The systematics are incorporated via nuisance parameters, θ_j, where $G\left(\theta_j, 0, 1\right)$ is a Gaussian in θ_j with mean 0 and $\sigma = 1$. The expected number of events (+ the systematic shifts) in the k'th $m_{\ell\ell}$ bin is

$$N^k_{\text{s+b}} = N^k_{\text{s}}(g)\left(1 + \sum_j^{\text{Syst.}} \theta_j \cdot S^k_{\text{s}}(g)\right) + N^k_{\text{b,noDY}}\left(1 + \sum_j^{\text{Syst.}} \theta_j \cdot S^k_{\text{b}}\right) \tag{D.3}$$

where $N^k_{\text{s}}(g)$ is the nominal signal template value in the k'th $m_{\ell\ell}$ bin as a function of g that includes the DY interfering part, i.e. $|\text{DY}(m_{\ell\ell}) + X(m_{\ell\ell}, g)|^2$, and where $N^k_{\text{b,noDY}}$ is the nominal sum of other backgrounds (no DY) value in the k'th $m_{\ell\ell}$ bin. Finally, the term $S^k_{\text{s}}(g)$ is the relative systematic uncertainty template value of the interfering signal, in the k'th $m_{\ell\ell}$ bin as a function of g (these were shown in the previous sections), and the term S^k_{b} is the standard $1d$ relative systematic uncertainty of the "other backgrounds" (no DY).

For practical reasons, the dependency of N^k_{s} in g for every $m_{\ell\ell}$ bin is transformed into a `TF1` object (in g) which is then given to BAT so it can vary it continuously.

Appendix E

Event Displays

E.1 Highest mass dielectron events

Figures E.1-E.3 show the ATLANTIS display for the three events with highest observed invariant mass. The third one is also displayed with PERSINT (figure E.4). Their main characteristics are listed in Table 3.5.

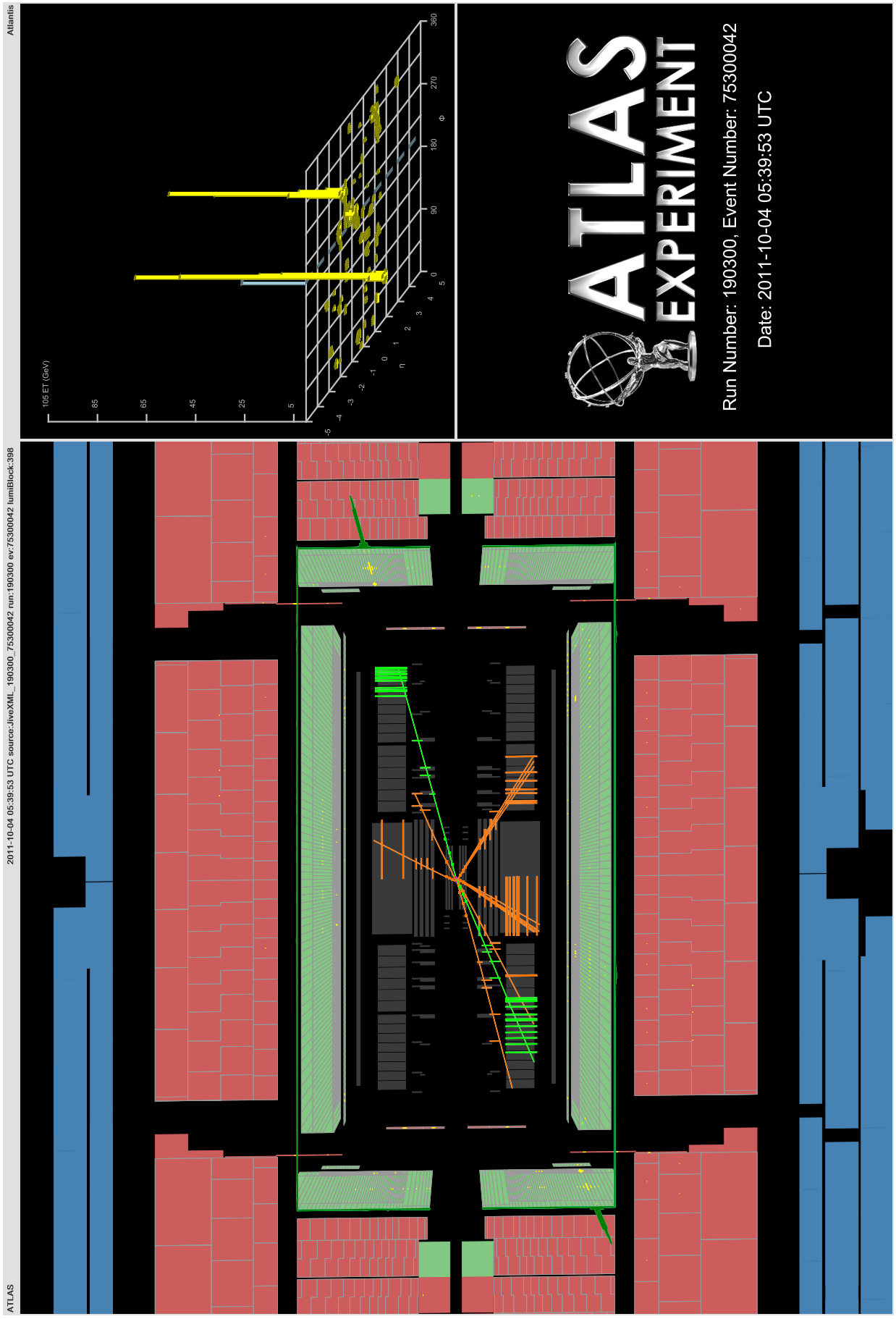

Figure E.1: ATLANTIS display of the highest mass electron event ($m_{ee} = 1.658$ TeV). The electron tracks are shown in green

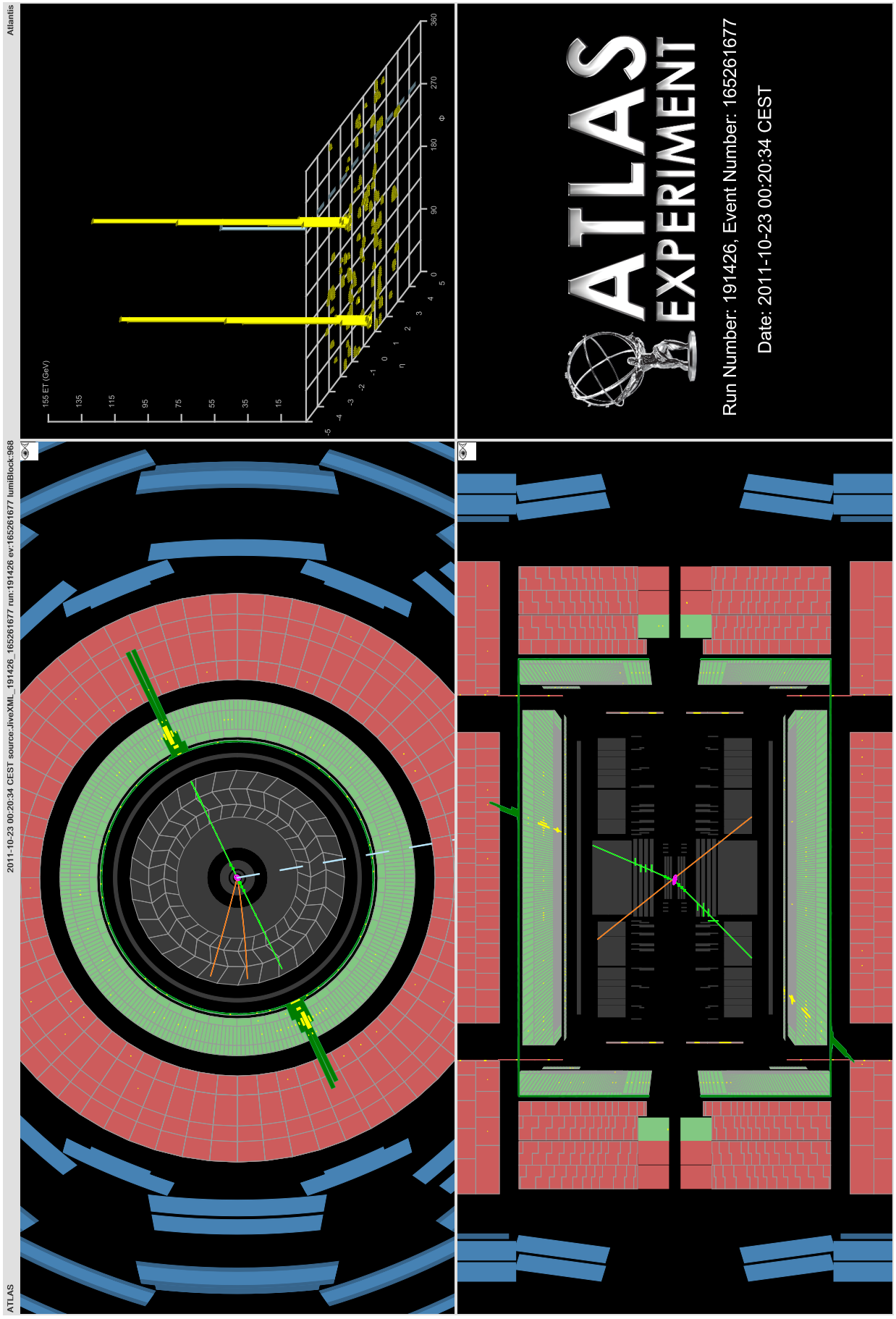

Figure E.2: ATLANTIS display of the second highest mass electron event (m_{ee} = 1.477 TeV). The electron tracks are shown in green

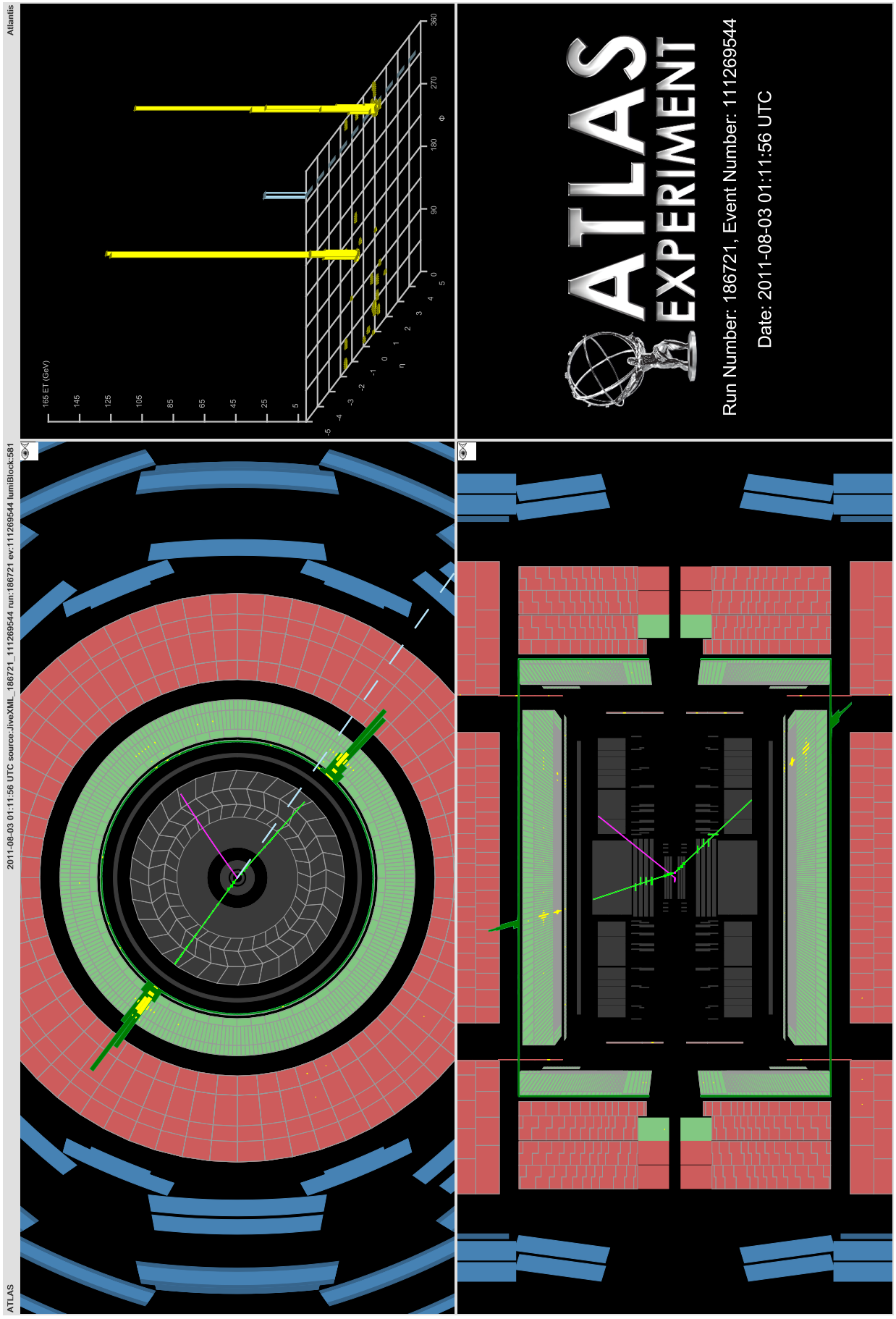

Figure E.3: ATLANTIS display of the third highest mass electron event ($m_{ee} = 1.214$ TeV). The electron tracks are shown in green

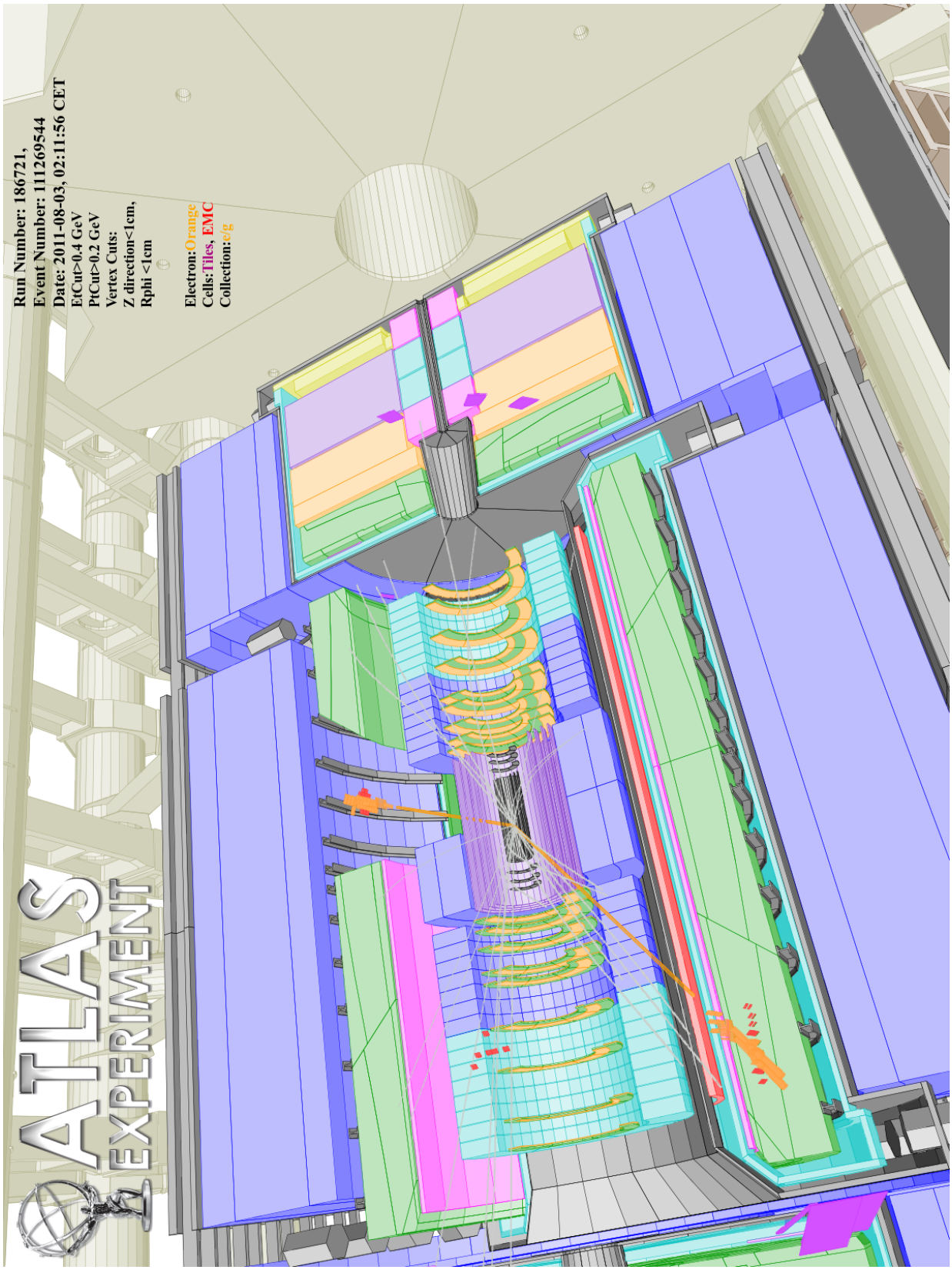

Figure E.4: PERSINT display of the third highest mass electron event ($m_{ee} = 1.214$ TeV). The electron tracks are shown in orange

Appendix F

Powheg vs Pythia DY Shape

We compare the $m_{\ell\ell}$ distribution at truth level using the two available DY Monte Carlo samples based on the POWHEG and PYTHIA event generators as explained in Section 3.1.2. The two distributions are shown in Figure F.2 (top) without any corrections and the ratio features a systematic positive slope as a function of $m_{\ell\ell}$. Further investigations have reveiled that the different choice of PDF (corrected for in Figure F.2 (middle)) and the treatment of α_{em} contribute to this difference. While PYTHIA was generated with MSTW2008 LO PDF and a running α_{em}, POWHEG was generated with CT10 NLO PDF and a fixed $\alpha_{em}(M_Z)$. Adjusting for these two differences, we find good agreement between the two event generators as shown in Figure F.2 (bottom). Given that the POWHEG sample provides higher statistics and was used to serve as the energy calibration reference[1] we will use the POWHEG sample in this analysis to describe the irreducible DY background.

[1]In principle the energy calibration should be sample independent, however due to a feature in the Powheg MC generation a MC sample dependence was effectively introduced that shifts the mass peak in the simulation by $\sim$ 40 MeV at the Z pole.

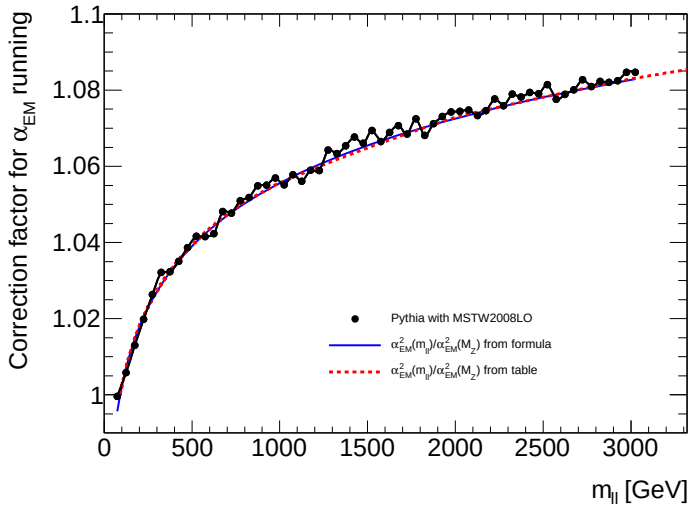

Figure F.1: Dilepton mass dependent correction factor due to running of α_{em}.

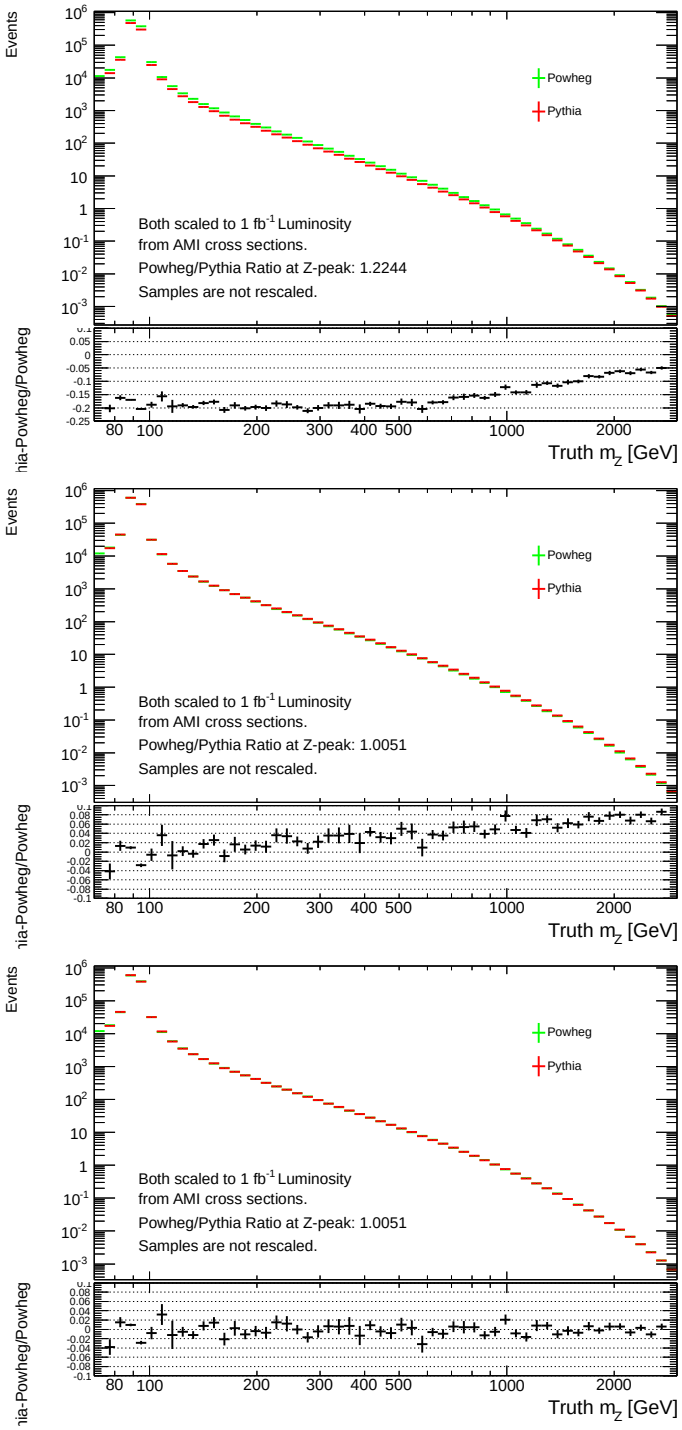

Figure F.2: Powheg vs Pythia DY $m_{\ell\ell}$ shape at truth level without any corrections (top), including the QCD K-factor and PDF reweighting (middle) and adding the running $\alpha_e m$ correction (bottom)

Bibliography

[1] D. Levin, R. Ball, J. Beene, Y. Benhammou, J. Chapman, T. Dai, E. Etzion, P. Friedman, M. B. Moshe, Y. Silver, R. V. Jr., C. Weaverdyck, S. White, B. Zhou, Development of a plasma panel muon detector, Nuclear Instruments and Methods in Physics Research Section A: Accelerators, Spectrometers, Detectors and Associated Equipment 652 (1) (2011) 315 – 318, symposium on Radiation Measurements and Applications (SORMA) {XII} 2010. doi:http://dx.doi.org/10.1016/j.nima.2010.07.076.
URL http://www.sciencedirect.com/science/article/pii/S0168900210016906

[2] P. Friedman, R. Ball, J. W. Chapman, D. Levin, C. Weaverdyck, B. Zhou, Y. Benhammou, E.Etzion, M. B. Moshe, Y. Silver, J. Beene, R. Varner, Large-Area Plasma-Panel Radiation Detectors for Nuclear Medicine Imaging to Homeland Security and the Super Large Hadron Collider, International Display Symposium Seattle WA.

[3] P. S. Friedman, A New Class of Low Cost, High Performance Radiation Detectors, IEEE NSS-MIC Conference Record (2005) 2815–2822.

[4] P. S. Friedman, R. Stoller, US Patents 7,332,726 (2008); 7,518,119 (2009); 7,564,039 (2009); 7,696,485 (2010) and 7,982,191 (2011).

[5] The ATLAS Experiment at the Large Hadron Collider, JINST 3 (2008) S08003.

[6] T. G. Rizzo, Testing the nature of Kaluza-Klein excitations at future lepton colliders, Phys. Rev. D61 (2000) 055005. doi:10.1103/PhysRevD.61.055005.

[7] T. Sjöstrand, S. Mrenna, P. Z. Skands, A Brief Introduction to PYTHIA 8.1, Comput. Phys. Commun. 178 (2008) 852–867. doi:10.1016/j.cpc.2008.01.036.

[8] G. Bella, E. Etzion, N. Hod, Y. Oz, Y. Silver, M. Sutton, A search for heavy Kaluza-Klein electroweak gauge bosons at the LHC, JHEP 09 (2010) 025. doi:10.1007/JHEP09(2010)025.

[9] R. Ball, J. W. Chapman, E. Etzion, P. S. Friedman, D. S. Levin, M. B. Moshe, C. Weaverdyck, B. Zhou, Plasma Panel Detectors for MIP Detection for the SLHC and a Test Chamber Design, IEEE Nuclear Science Symposium Conference Record (2009) 1321–1327.

[10] J. P. Boeuf, Plasma display panels: physics, recent developments and key issues, J. Phys. D Appl. Phys. 36 (2003) 53–79.

[11] K. Nakamura, et al., Review of particle physics, J. Phys. G37 (2010) 075021. doi:10.1088/0954-3899/37/7A/075021.

[12] Magboltz collaboration.
URL http://consult.cern.ch/writeup/magboltz/

[13] Z. f. H. Raether, Physik 112 (1939) 464.

[14] J. M. Meek, A Theory of Spark Discharge, Physical Review V.57.

[15] L. W. Nagel, D. O. Pederson, SPICE (Simulation Program with Integrated Circuit Emphasis), Memorandum No. ERL-M382, University of California, Berkeley.

[16] Comsol multiphysics homepage.
URL http://www.comsol.com/products/multiphysics

[17] S. Agostinelli, et al., GEANT4: A simulation toolkit, Nucl. Instrum. Meth. A506 (2003) 250.

[18] Ion beam applications website.
URL http://www.iba-worldwide.com/

[19] Cdh proton center, a procure center, in suburban chicago website.
URL http://www.procure.com/OurLocations/Illinois.aspx

[20] A. Munoz, et al., Energy deposition model based on electron scattering cross section data from water molecules, Journal of physics Conference Series 133. doi:10.1088/1742-6596/1331/1/012002.

[21] PSI DRS4 Chip homepage.
URL http://drs.web.psi.ch

[22] R. Ball, J. Chapman, J. Hollar, J. Kuah, ATLAS MiniDAQ Reference Guide.
URL http://atlas.physics.lsa.umich.edu/docushare

[23] W-ie-ne-r, plein & baus gmbh.
URL http://www.wiener-d.com/sc/modules/nim--modules/nimbox-npl20.html

[24] CAEN V560 User Manual.
URL http://www.caen.it/csite/CaenProd.jsp?parent=11&idmod=62

[25] CAEN V1290 User Manual.
URL http://www.caen.it/csite/CaenProd.jsp?parent=11&idmod=791

[26] R. Ball, J. R. Beene, Y. Benhammou, M. B. Moshe, J. W. Chapman, T. Dai, E. Etzion, P. S. Friedman, D. S. Levin, Y. Silver, G. Sherman, R. L. V. Jr., C. Weaverdyck, S. White, J. Yu, B. Zhou, Progress in the Development of Plasma Panel Radiation Detectors, IEEENuclear Science Symposium Conference, (Knoxville, TN) (2010) Paper N50–7.

[27] S. Glashow, Partial-symmetries of weak interactions, Nuclear Physics 22 (1961) 579–588. doi:10.1016/0029-5582(61)90469-2.

[28] S. Weinberg, A model of leptons, Physical Review Letters 19 (1967) 1264–1266. doi:10.1103/PhysRevLett.19.1264.

[29] A. Salam, Weak and Electromagnetic Interactions, Conf.Proc. C680519 (1968) 367–377.

[30] N. Arkani-Hamed, M. Schmaltz, Hierarchies without symmetries from extra dimensions, Phys. Rev. D61 (2000) 033005. arXiv:hep-ph/9903417, doi:10.1103/PhysRevD.61.033005.

[31] A. Leike, The Phenomenology of extra neutral gauge bosons, Phys. Rept. 317 (1999) 143–250. arXiv:hep-ph/9805494, doi:10.1016/S0370-1573(98)00133-1.

[32] P. Langacker, The Physics of Heavy Z' Gauge Bosons, Rev. Mod. Phys. 81 (2009) 1199–1228.

[33] D. London, J. L. Rosner, Extra Gauge Bosons in E(6), Phys. Rev. D34 (1986) 1530.

[34] M. Dittmar, A.-S. Nicollerat, A. Djouadi, Z' studies at the LHC: An update, Phys. Lett. B583 (2004) 111–120.

[35] E. Accomando, et al., Z' physics with early LHC data, Phys. Rev. D83 (2011) 075012. doi:10.1103/PhysRevD.83.075012.

[36] D. Bardin, et al., CERN-TH.5468/89.

[37] G. Azuelos, G. Polesello, Eur. Phys. J. C 39 (2004) s2, s1–s11.

[38] T. G. Rizzo, Indirect Searches for Z'-like Resonances at the LHC, JHEP 08 (2009) 082. doi:10.1088/1126-6708/2009/08/082.

[39] K. Cheung, G. Landsberg, Phys. Rev. D 65 (2008) 076003.

[40] V. M. Abazov, et al., Search for a heavy neutral gauge boson in the dielectron channel with 5.4 fb^{-1} of $p\bar{p}$ collisions at $\sqrt{s} = 1.96$ TeV, Phys. Lett. B695 (2011) 88–94.

[41] T. Aaltonen, et al., Search for High Mass Resonances Decaying to Muon Pairs in $\sqrt{s} = 1.96$ TeV $p\bar{p}$ Collisions, Phys. Rev. Lett. 106 (2011) 121801.

[42] G. Abbiendi, et al., Tests of the standard model and constraints on new physics from measurements of fermion pair production at 189 GeV to 209 GeV at LEP, Eur. Phys. J. C33 (2004) 173–212.

[43] J. Abdallah, et al., Measurement and interpretation of fermion-pair production at LEP energies above the Z resonance, Eur. Phys. J. C45 (2006) 589–632.

[44] P. Achard, et al., Measurement of hadron and lepton-pair production in e^+e^- collisions at $\sqrt{s} = 192$ GeV to 208 GeV at LEP, Eur. Phys. J. C47 (2006) 1–19.

[45] S. Schael, et al., Fermion pair production in e^+e^- collisions at 189-209 GeV and constraints on physics beyond the standard model, Eur. Phys. J. C49 (2007) 411–437.

[46] J. Erler, P. Langacker, S. Munir, E. R. Pena, Improved constraints on Z' bosons from electroweak precision data, JHEP 0908 (2009) 017.

[47] T. A. collaboration, Search for high-mass resonances decaying to dilepton final states in pp collisions at a center-of-mass energy of 7 TeV with the ATLAS detector, JHEP 1211 (2012) 138. doi:10.1007/JHEP11(2012)138.

[48] R. Brun, F. Rademakers, ROOT - An Object Oriented Data Analysis Framework, Nucl. Inst. & Meth. in Phys. Res. A. 389 (1997) 81, http://www.fnal.gov/pub/now/tevlum.html.

[49] S. Hassani, et al., A muon identification and combined reconstruction procedure for the atlas detector at the lhc using the (muonboy, staco, mutag) reconstruction packages, Nucl. Instrum. Meth. A 572 (2007) 77.

[50] D. Fassouliotis, et al., Muon identification using the muid packageATL-MUON-2003-003 (link).

[51] The ATLAS Simulation Infrastructure, Eur. Phys. J. C70 (2010) 823–874.

[52] T. Sjöstrand, S. Mrenna, P. Skands, PYTHIA 6.4 physics and manual, JHEP 05 (2006) 026.

[53] G. Corcella, et al., HERWIG6: an event generator for hadron emission reactions with interfering gluons (including supersymmetric processes), JHEP 01 (2001) 010.

[54] G. Corcella, I. Knowles, G. Marchesini, S. Moretti, K. Odagiri, P. Richardson, M. Seymour, B. Webber, HERWIG 6.5 Release Note, arXiv:hep-ph/0210213.

[55] J. M. Butterworth, J. R. Forshaw, M. H. Seymour, Multiparton interactions in photoproduction at HERA, Z. Phys. C72 (1996) 637–646.

[56] E. Boos, et al., CompHEP 4.4: Automatic computations from Lagrangians to events, Nucl. Instrum. Meth. A534 (2004) 250–259.

[57] J. Alwall, et al., MadGraph/MadEvent v4: The New Web Generation, JHEP 09 (2007) 028. doi:10.1088/1126-6708/2007/09/028.

[58] S. Frixione, B. R. Webber, Matching NLO QCD computations and parton shower simulations, JHEP 06 (2002) 029.

[59] M. L. Mangano, et al., ALPGEN, a generator for hard multiparton processes in hadronic collisions, JHEP 07 (2003) 001.

[60] A. Sherstnev, R. S. Thorne, Parton Distributions for LO Generators, Eur. Phys. J. C55 (2008) 553.

[61] A. Sherstnev, R. Thorne, Different PDF approximations useful for LO Monte Carlo generators (2008) 149arXiv:0807.2132.

[62] ATLAS Collaboration, ATLAS tunes of PYTHIA 6 and Pythia 8 for MC11, aTL-PHYS-PUB-2011-009 (http://cdsweb.cern.ch/record/1399599/).

[63] ATLAS Collaboration, Search for contact interactions in dilepton events from pp collisions at $\sqrt{s} = 7$ TeV with the ATLAS detector, Phys. Lett. B712 (2012) 40–58.

[64] P. M. Nadolsky, et al., Implications of CTEQ global analysis for collider observables, Phys. Rev. D78 (2008) 013004.

[65] H.-L. Lai, M. Guzzi, J. Huston, Z. Li, P. M. Nadolsky, et al., New parton distributions for collider physics, Phys. Rev. D82 (2010) 074024. arXiv:1007.2241, doi:10.1103/PhysRevD.82.074024.

[66] C. M. Carloni Calame, et al., Precision electroweak calculation of the production of a high transverse-momentum lepton pair at hadron colliders, JHEP 10 (2007) 109. arXiv:0710.1722, doi:10.1088/1126-6708/2007/10/109.

[67] C. M. Carloni Calame, et al., Precision electroweak calculation of the charged current Drell-Yan process, JHEP 0612 (2006) 016.

[68] R. Blair, et al., ATLAS Standard Model Cross Section recommendations for 7 TeV LHC 2 running, https://svnweb.cern.ch/trac/atlasgrp/export/50132/Physics-/StandardModel/xsectf/note/xsectf.pdf (2010).

[69] J. M. Butterworth, et al., Single and Diboson Production Cross Sections in *pp* collisions at $\sqrt{s} = 7$ TeV, ATL-COM-PHYS-2010-695.

[70] Electron performance measurements with the ATLAS detector using the 2010 LHC proton-proton collision data, Eur. Phys. J. C72 (2012) 1909.

[71] EGamma group, Efficiency Measurements, https://twiki.cern.ch/twiki/bin/view/AtlasProtected/Effi

[72] EGamma group, Energy Scale and Resolution recommendations, https://twiki.cern.ch/twiki/bin/view/AtlasProtected/EnergyScaleResolutionRecommendations.

[73] Exotics dilepton group, Search for high mass dilepton resonances in pp collisions at $\sqrt{s} = 7$ TeV (2011 update for the EPS conference), aTL-COM-PHYS-2011-770 (http://cdsweb.cern.ch/record/1361706/).

[74] Exotics dilepton group, Search for high mass dilepton resonances in 5/fb of pp collisions at $\sqrt{s} = 7$ TeV, aTL-COM-PHYS-2012-177 (http://cdsweb.cern.ch/record/1424738/).

[75] A. Caldwell, D. Kollar, K. Kröninger, BAT - The Bayesian Analysis Toolkit, Comput. Phys. Commun. 180 (2009) 2197.

[76] ATLAS Electromagnetic Barrel Calorimeter Collaboration, Energy linearity and resolution of the ATLAS electromagnetic barrel calorimeter in an electron test-beam, Nucl. Instrum. Meth. A568 (2006) 601–623.

[77] G. Choudalakis, On hypothesis testing, trials factor, hypertests and the BumpHunterarXiv:arXiv:1101.0390v2.

[78] G. Choudalakis, D. Casadei, Plotting the Differences Between Data and ExpectationarXiv:1111.2062.

[79] Exotics dilepton group, Limit Setting and Signal Extraction Procedures in the Search for Narrow Resonances Decaying into Leptons at ATLAS, aTL-COM-PHYS-2011-085 (http://cdsweb.cern.ch/record/1325592/).

[80] G. Azuelos, G. Polesello, *Prospects of the detection of Kaluza-Klein excitations of gauge bosons in the ATLAS detector at the LHC*, sN-ATLAS-2003-023 (2003).

[81] R. Hamberg, W. L. van Neerven, T. Matsuura, A Complete calculation of the order α_s^2 correction to the Drell-Yan K factor, Nucl. Phys. B359 (1991) 343–405.

[82] ATLAS Collaboration, Electron performance measurements with the ATLAS detector using the 2010 LHC proton-proton collision data, Eur.Phys.J. C72 (2012) 1909. arXiv:1110.3174.

[83] K. Melnikov, F. Petriello, Electroweak gauge boson production at hadron colliders through $O(\alpha_s^2)$, Phys. Rev. D 74 (2006) 114017. arXiv:0609070.

List of Figures

List of Tables